Epithelial signals that influence the form and function of somatosensory neurons in Drosophila

Nan Jiang

A dissertation

submitted in partial fulfillment of the

requirements for the degree of

Doctor of Philosophy

University of Washington

2017

Reading Committee:

Jay Z. Parrish, Chair

David W. Raible

Martha Bosma

Program Authorized to Offer Degree:

Biology

University of Washington

Abstract

Epithelial signals that influence the form and function of somatosensory neurons in *Drosophila*

Nan Jiang

Chair of the Supervisory Committee:
Associate Professor, Jay Z. Parrish
Department of Biology

Cell-cell interaction plays an important role in regulating cell morphology and function. In the peripheral nervous system, somatosensory neurons innervate our skin and interact with the epidermis to help us sense the world. However, the cellular interactions between epidermis and neurons and possible mechanisms by which the skin controls neuron growth and function are largely unexplored. This gap in our knowledge limits our ability to treat somatosensory neuron disease, which has a major impact on the quality of human lives. In our lab, we use Drosophila Class IV da neurons as a model system to study the interaction between somatosensory neurons and epidermis. Firstly, we identified signals derived from epithelial cells that regulate the coordinated growth between the Class IV sensory neurons and body wall epithelial cells during Drosophila larva development. We

found epithelial microRNA bantam regulates a special type of cell cycle in body wall epithelial cells, which then mediates dendrite growth through regulating a close interaction between dendrites and body wall epithelial cells. This close dendrite-epithelial interaction, where dendrites are ensheathed by epithelial cells, is a conserved structure across species. We identified and characterized the molecular components on epithelial membrane specialized domains that are associated with dendritic ensheathment by using the GAL4-UAS expression screen and an expansion microscopy imaging technique that we adapted specifically for this purpose. We found this actin rich structure on the epithelial cell membrane is regulated by epithelial endocytosis. Interestingly, this epithelial membrane specialized domain can facilitate and stabilize dendritic ensheathment which is induced by dendrite derived signals. Finally, we found that dendritic ensheathment also plays very important functional roles by mediating the Class IV da neuron nociception.

TABLE OF CONTENTS

LIST OF FIGURES

ACKNOWLEDGEMENTS

I would like to thank my advisor Dr. Jay Parrish for the continuous support of my PhD research. Besides my advisor, I would like to thank the rest of my thesis committee : Dr. David Raible, Dr. Martha Bosma, and Dr. Susan Parkhurst, for their insightful comments and encouragement.

My sincere thanks also go to our collaborators: Dr. Joshua Vaughan, Dr. Ben Eaton, Dr. Charlie Kim, Dr. Peter Soba for their inputs and help on my projects.

I thank my fellow lab mates for being supportive all the time.

Last but not the least, I would like to thank my family for supporting me throughout my PhD life.

INTRODUCTION

The somatosensory system consists of peripheral receptors and neural pathways through which the nervous system detects and processes information about touch (mechanoception), pain (nociception), temperature (thermoception) and the position and movement of parts of the body (proprioception). Malfunction of the somatosensory system leads to diseases such as peripheral neuropathy. In the USA, an estimated 20 million people are suffering from some form of peripheral neuropathy, with symptoms ranging from numbness and tingling to severe pain and organ dysfunction. Peripheral neuropathy can be due to various causes, such as diabetes, chemotherapy and inheritance. These can induce axonopathy, demyelination and altered expression of particular ion channels on neurons (Hughes, 2002;Marshall Devor, 2013). Due to limitations in the sensitivity of clinical tests, it is usually difficult to diagnose peripheral neuropathy in all but advanced cases. Unfortunately, most peripheral neuropathy cases are uncurable, with current treatment options limited by generally significant undesirable side effects, such as drowsiness, dizziness, cognitive impairment, and nausea to name only a few (Seward B Rutkove, 2015). Therefore, a better understanding of somatosensory neurons is extremely critical to develop new treatments for peripheral neuropathy and improve quality of life.

Different somatosensory neurons play different roles dependent on their distinct morphology

The ability for neurons to receive and process external stimuli is mediated by specific characeristics of the neuronal processes. One hundred years ago, Ramon y Cajal provided illustrations of the complex and varied patterns of somatosensory neurons that innervate

the epidermis and muscle (Ramon y Cajal, 1909). In humans, somatosensory neurons can be differentiated into distinct subtypes which target different receptors to transmits specific kinds of stimuli. In skin, myelinated Aβ and Aδ axons attach to hair follicles to sense light touch; unmyelinated C fiber and Aδ axons innervate the epidermis layer of the skin to respond to injurious forces (Delmas et al., 2011). In *C.elegans*, multi-branched sensory neurons PVD and FLP are both mechanosensory neurons, but occupy distinct and non-overlapping receptive fields on the body wall (Albeg et al., 2011; Chatzigeorgiou et al., 2010). Similarly, In *Drosophila* larva, there are four classes of somatosensory neurons categorized by their distinct morphologies that grow underneath the skin (Bodmer and Jan, 1987; Grueber et al., 2003). Among these are Class IV dendritic arborization (da) neurons which detect intense mechanical forces, noxious heat, harmful short-wave light and dry-surface environment (Guo et al., 2014; Hwang et al., 2007; Kim and Johnson, 2014; Xiang et al., 2010). There are also Class III da neurons which respond to gentle touch via the NOMPC mechanotransduction channel (Yan et al., 2013). The function of Class I and Class II da neurons is not known.

Neuron-substrate interaction is important to somatosensory neuron function

Communication methods between somatosensory neurons and other cells are myriad. In skin, sensory nerve terminals interact with sensory receptors. For instance, Merkel cells are a rare population of epithelial cells in the skin of most vertebrates (Moll et al., 1996). They are found in touch-sensitive areas such as finger tips and lips (Boot et al., 1992). Studies show that Merkel-cells function as touch-sensitive receptors in the skin that directly produce action potentials in neighboring Aβ axon fibers (Maksimovic et al.,

2014). Merkel-cells contact sensory afferent terminals to form synaptic-like interaction (Maksimovic et al., 2013; Shimohira-Yamasaki et al., 2006).

In addition, somatosensory neurons also interact with glial cells. In the mammalian PNS, somatosensory axons interact with Schwann cells to form the myelin sheath. Myelin sheath functions to speed up the impulse propagation along the nerve. It also helps with the degradation and regrowth of the injured nerves (Arthur-Farraj et al., 2012; Jessen and Mirsky, 2016). Demyelination is a common cause of peripheral neuropathy.

Substrate derived signals regulate somatosensory neuron patterning

The signals that guide somatosensory neurons to their targets and shape their arbors are unclear. In recent years, studies on the intercellular communications between somatosensory neurons and their substrates have been done in numerous model organisms.

In vertebrates, somatosensory neurons begin innervating the skin at early developmental stages to sense pain, heat and touch. For example, human dorsal root ganglion axons reach the epidermis by 7 weeks of development (Moore and Munger, 1989) and mouse trigeminal axons begin innervating the skin at approximately E10.5 (Davies and Lumsden, 1984). Again, Ramon y Cajal (1919) was the first to suggest that developing skin may attract sensory axons to it, based on the observation that collaterals branch off sensory nerve trunks as the nerves approach the skin. His hypothesis has been supported by several later studies. In mice, the outgrowth of the earliest cutaneous axons from the trigeminal ganglion appears to be directed by a diffusible factor produced by the target epithelium (Lumsden and Davies, 1983). In zebra fish, peripheral axons display a

misrouting phenotype when epidermis heparin sulfate proteoglycan (HSPG) is depleted (Wang et al., 2012).

Relatively more neuron-epidermis interaction studies have been published using invertebrate model organisms due to the simplicity of their structures. In *C.elegans*, PVD mechanosensory neurons cover the body wall with all the dendrites growing along the surface of the epidermis and some branches sandwiched between the epidermis and body wall muscles. Previous studies have shown that signals derived from epidermis (SAX-7/L1CAM and MNR-1/Menorin), can form a co-ligand complex on the epidermis to regulate the patterning of PVD dendrites (Dong et al., 2013; Salxberg et al., 2013). In addition, muscles can also provide direct cues to influence dendrite patterning. Molecules secreted from muscles such as UNC-52 and LECT-2, have been identified to orient PVD neuron 4 dendrites relative to the muscle arrangement (Liang et al., 2015).

Similarly, in *Drosophila*, somatosensory neuron patterning is regulated by cues derived from both epidermis and muscles. In adult flies, dendrites of the mechanosensory neurons are oriented along muscle fibers; shortly after eclosion, dendrite arbors are remodeled and subsequently reorient to interdigitate lateral tergosternal muscles (Yasunaga et al., 2010). In the larval stage, signals derived from epidermis and ECM regulate dendrite branching (Jiang et al., 2014; Parrish et al., 2009) and 3D spacing (Han et al., 2012; Kim et al., 2012).

Somatosensory neuron processes are sometimes ensheathed by epithelial cells

One intriguing observation made when studying interactions between somatosensory neurons and epidermis is that somatosensory neuron processes are sometimes located within skin epithelial cells, in the same way that peripheral axons are ensheathed by

Schwann cells. This neuron-epitehlial interaction is entitled the *ensheathment structure*. It has been found and described across species (Cauna, 1973; Goodman, 2006; Han et al., 2012; Jiang et al., 2014; Kim et al., 2012; O'Brien et al., 2012). However, no studies have explored the formation, structure and function of the ensheathment structure.

One major reason this interesting structure has been overlooked is its diminutive size. It measures only hundreds of nanometers and there are no well characterized markers to label it. In all published studies, it has been visualized by using transmission electron microscopy (TEM). TEM is expensive and cumbersome and is poorly suited for both regular clinical diagnosis and high throughput bench research. Developing easier to implement super resolution imaging techniques will accelerate the progress of neuronal ensheathment study. Identifying and characterizing specific ensheathment markers will also aid in the process.

Super resolution imaging techniques need to be optimized to study neuron-epithelial interaction

Even though many super resolution imaging techniques have been developed (Hell and Wichmann, 1994; Rust et al., 2006; Schermelleh et al., 2008), current techniques are not suited to all types of tissues and multi-color 3D imaging. In addition, the hardware and software tools are expensive. In 2015, Ed Boyden's group at MIT developed expansion microscopy (ExM) for super resolution imaging. Rather than improving power and quality of the microscope, they instead expanded biological specimens by approximately four times normal size in a polymer gel to produce much higher resolution images (Chen et al., 2015). Soon after Chen's study, optimizations on this exciting technology were published (Chozinski et al., 2016; Tillberg et al., 2016). With this technology, researchers can do super resolution imaging by using a conventional confocal microscope. To date, it

has been easily applied to cultured cells and soft tissues, for example brain slices. However, for it to have broader applications, adaptations need to be made in the ExM workflow. Such adaptations will allow ExM to be applied to a wider range of tissues.

In my thesis study, I first used Drosophila larva class IV da neurons as a model system to identify interactions between epithelial cells and dendrites that regulate dendrite growth and patterning. In the second chapter, I adapted expansion microscopy to the Drosophila system to allow us to look at high resolution structures of dendrite-epithelial interaction. Finally I focused on the dendritic ensheathment structure and characterized the cell biology basis and function of this type of interaction.

Chapter 1. Epithelial-derived signals that regulate dendrite growth

1.1 INTRODUCTION

As animals grow, dendrite arbors of many neurons must expand proportionally to sustain proper connectivity and maintain coverage of their receptive field. For example, mouse lumbar motor neuron dendrites grow to preserve dendrite topology as the spinal cord expands postnatally (Li et al., 2005). Likewise, scalar expansion of dendrite arbors to accommodate growth is widely documented in sensory systems. For example, vertebrate retinal ganglion cells (RGCs) tile the retina early in development, after which they expand their dendrites synchronously with the several-fold expansion of the retina that occurs postnatally (Bloomfield and Hitchcock, 1991; Hitchcock, 1987; Ramoa et al., 1988; Ren et al., 2010). Despite the prevalence of this phenomenon, little is known about how dendrite and substrate expansion are coordinated.

Several observations suggest that neuron non-autonomous growth-inhibitory signals likely contribute to the fidelity of dendrite arbor expansion by restricting dendrite arbors to target fields. Following genetic ablation of RGCs (Lin et al, 2004) or chemotropic ablation of starburst cholinergic amacrine cells (Farajian et al, 2004), the surviving cells developed regularly spaced adult dendrite arbors that exhibited a limited ability to expand into unoccupied territory. Therefore, interactions between neighboring dendrites are largely dispensable for maintenance of coverage in these neurons and unknown constraints limit their growth potential. Arguing in favor of an extrinsic component, these neurons retain the ability to expand their dendrite arbors to accommodate retinal growth, whereas exuberant growth is limited. Progressive restriction in dendrite structural plasticity has been observed in other contexts in the mammalian

nervous system as well, for example in hippocampal pyramidal neurons where the proportion of stable dendritic spines increases over time (Holtmaat et al., 2005; Zuo et al., 2005), suggesting that restriction of plasticity may be an important component of dendrite maintenance.

Drosophila peripheral nervous system (PNS) class IV dendrite arborization (C4da) neurons completely and non-redundantly cover the body wall early in development and maintain this tiling by growing in precise synchrony with their substrate, the body wall epithelium (Emoto et al., 2006; Grueber et al., 2002; Parrish et al., 2007, 2009). Prior to establishment of tiling, ablating C4da neurons leads to exuberant dendrite growth into unoccupied territory by adjacent neurons (Grueber et al., 2003; Parrish et al., 2009; Sugimura et al., 2003). This invasive growth potential is lost during the maintenance phase, and receptive field boundaries established by the $1^{st}/2^{nd}$ instar transition are subsequently maintained, even when dendrites establish aberrant coverage. Dendrite arbors grow after the $1^{st}/2^{nd}$ instar transition, but growth occurs only to maintain proportional receptive field coverage, showing that, as with RGCs, signals constrain late-stage growth of these dendrites. Notably, this signaling does not involve the homotypic repulsion required to establish tiling (Emoto et al., 2004). Instead, these neurons depend on epithelial-derived signals that restrict exuberant arbor expansion; the miRNA *bantam* (*ban*) acts in epithelial cells to regulate substrate-derived growth-inhibitory signals constrain dendrite growth (Parrish et al., 2009).

Here, we report our characterization of *ban*-regulated epithelial signaling that regulates dendrite growth. Using microarray-based expression profiling, we identified *ban*-regulated gene expression programs involved in cell growth, the cell cycle and cell

adhesion. We further found that *ban* influences dendrite development by regulating a developmental switch in epithelial growth, namely the onset of endoreplication, as manipulating epithelial endoreplication using *ban*-independent approaches recapitulates *ban*-mediated effects on dendrite growth. Endoreplication influences epithelia-dendrite and epithelia-ECM interactions, providing the cellular basis for the reduced dendrite growth potential that accompanies larval development. At a molecular level, the onset of endoreplication leads to alterations in cell adhesion molecules, and up-regulation of the integrin Mys is required for proper coupling of dendrite and substrate expansion and to constrain dendritic structural plasticity.

1.2 RESULTS

1.2.1 Identification of bantam-regulated pathways

The microRNA *ban* functions as a regulatory switch for substrate-derived signaling that restricts PNS dendrite growth and structural plasticity to ensure proportional expansion of dendrite and substrate (Figure 1.1 A; Parrish et al 2009). To identify substrate-derived regulators of dendrite growth required for proportional growth of dendrite and substrate, we set out to identify pathways regulated by the miRNA *ban* in epithelial cells. To this end, we conducted microarray-based expression profiling of FACS isolated GFP-positive epithelial cells from wild type (WT) and *ban* mutant larvae (Figure 1.1 B). We identified ~100 transcripts that were significantly deregulated in *ban* mutant epithelial cells (Figure 1.1 C), including a disproportionately large number of transcripts associated with cell growth, the cell cycle, and cell adhesion, suggesting that *ban* regulates these processes in epithelial cells.

Drosophila increase their mass ~200-fold during larval development, and this growth is accomplished by cell expansion rather than cell addition (Britton and Edgar, 1998; Church and Robertson, 1966). Indeed, we found that the number of body wall epithelial cells is constant from late embryogenesis to late larval stages, and that epithelial cells infrequently turnover, as epithelial cell clones persist from embryonic to larval stages >98% of the time (n=200; Figure 1.1 D, E). Since body wall epithelial cell number is unresponsive to *ban* activity (Figure 1.1 D), *ban* regulation of epithelial growth must involve growth of existing cells rather than proliferation. Although *ban* is known to regulate proliferation, and hence growth, in mitotically active tissues (Brennecke et al., 2003; Hipfner et al., 2002), how *ban* regulates growth of differentiated cells is unknown.

To facilitate larval growth, many larval cell types undergo endoreplication, a modified cell cycle that entails DNA replication without cell division (Britton and Edgar, 1998; Smith and Orr-Weaver, 1991). Consistent with a change in endoreplication, *ban* mutant epithelial cells exhibited dysregulation of numerous cell cycle-associated genes, including reduced expression of two regulators of endoreplication, *double parked (dup)* and *retina aberrant in pattern (rap)* (Park and Asano, 2008; Pimentel and Venkatesh, 2005; Sigrist and Lehner, 1997; Zielke et al., 2008), which encode orthologs of the DNA replication factor CDT1 and the APC/C activator CDH1/FZR1, respectively (Figure 1.1 C). We therefore hypothesized that *ban* regulates growth of mitotic (e.g. imaginal discs) and post-mitotic body wall epithelial cells by regulating different forms of the cell cycle.

To monitor larval endoreplication during the period of *ban* activity required for dendrite growth, we fed newly hatched 1st instar larvae BrdU for one day and monitored BrdU incorporation in 2nd and 3rd instar larvae. As a positive control we first measured

BrdU incorporation in the larval ventral ganglion, which contains mitotically active neuroblasts and endoreplicating glia (Truman and Bate, 1988; Unhavaithaya and Orr-Weaver, 2012), and observed extensive BrdU labeling (Figure 1.2 A, B). Likewise, we observed extensive labeling of epithelia and muscle, but no labeling of sensory neurons (Figure 1.2 C). PNS neurons fail to incorporate BrdU even when BrdU is constantly administered, and nucleic acid content of PNS neurons is constant from late embryonic stages through larval development, therefore we conclude that body wall epithelia and muscle, but not sensory neurons endoreplicate.

To monitor the timing and extent of endoreplication in the larval epidermis we measured DNA content in epithelial cells over development beginning with late stage embryos. Because PNS neurons do not endoreplicate, we normalized epithelial DAPI intensity to DAPI intensity of diploid PNS neurons located in the same segment. During embryogenesis, epithelial cells and PNS neurons had comparable levels of DAPI staining, and hence DNA content (Figure 1.2 D, E). Similar to other larval tissues (Britton and Edgar, 1998), body wall epithelia exhibited very low levels of endoreplication after hatching; DNA content in 1st instar epithelial cells was approximately 2.8-fold higher than PNS neurons. Epithelial ploidy increased throughout the remainder of larval development, and the rate of endoreplication increased dramatically at 48h AEL leading to a ~25-fold increase in genome content by 96h AEL. The increase in epithelial cell size closely followed the increase in endoreplication, with the pace of epithelial growth dramatically increasing after 48h AEL (Figure 1.2 F). Indeed, we observed a strong linear relationship between epithelial DNA content and epithelial cell size, suggesting that the two are tightly coupled (Figure 1.2 G). By

contrast, C4da dendrite expansion was anticorrelated with epithelial growth; C4da dendrites expanded most rapidly when they are establishing tiling of the body wall prior to 48h AEL, after which C4da dendrites expand at precisely the same rate as their substrate to maintain coverage of a fixed portion of the body wall (Figure 1.2 H and Parrish et al, 2009).

ban is required in epithelial cells to dampen dendrite growth beginning at ~48h AEL (Parrish et al., 2009), after dendrites have established tiling of the body wall and coincident with the rapid increase in epithelial endoreplication. We therefore assayed for *ban* function in endoreplication by monitoring BrdU incorporation in *ban* mutant larvae and found that BrdU incorporation was reduced by an average of 56% in *ban* mutant body wall epithelial cells compared to wild type controls (Figure 1.2 I). Likewise, epithelial ploidy was significantly reduced in *ban* mutants, as in *dup* and *rap* mutants (Figure 1.2 J). By contrast, epithelial ploidy was increased by overexpression of *ban* to a similar degree as overexpression of *diminutive* (*dm*; encodes *Drosophila* Myc), which promotes endoreplication in a variety of *Drosophila* cell types (Pierce et al., 2004). Thus, *ban* is necessary and sufficient to promote endoreplication in larval body wall epithelial cells, and the major wave of endoreplication is initiated in 2nd instar larvae, corresponding to the developmental time when *ban* functions in epithelial cells to coordinate dendrite and epithelial growth (Parrish et al., 2009).

We next investigated effects of *ban* activity and endoreplication on epithelial growth. *ban* mutant larvae exhibited significant decreases in epithelial cell size, as did larvae with mutations in *dup* or *rap*, whereas overexpression of *ban* or *dm* caused a

significant increase in cell size (Figure 1.2 K). Thus, *ban* regulates larval endoreplication, which promotes growth of larval epithelial cells.

1.2.2 Epithelial endoreplication influences dendrite growth

C4da dendrite growth outpaces substrate growth to establish complete, non-redundant coverage of the body wall (tiling), but growth is altered coincident with onset of epithelial endoreplication, such that dendrite arbors expand synchronously with the epidermis to maintain tiling of the growing body wall (Parrish et al., 2009). *ban* mutants tile the body wall properly, but dendrite and substrate growth are not synchronized at the $1^{st}/2^{nd}$ instar transition, hence dendrite growth continues to outpace substrate growth, causing dendrites to cross usual boundaries, occupy larger territories, and more densely populate the body wall (Parrish et al., 2009). As shown in Figure 1.3, C4da dendrites in *ban* mutant larvae exhibit a ~30% increase in the territory they cover (coverage index) and a ~140% increase in dorsal midline occupancy as a result of unchecked late stage growth.

We hypothesized that local signals, independent of systemic cues that promote larval growth and dendrite expansion, serve to coordinate dendrite and substrate growth and ensure proportiaonal expansion. Further, since *ban* regulates epithelial endoreplication, which is initiated on the same timescale as the developmental transition in larval dendrite growth, we hypothesized that epithelial endoreplication may be a critical component of this local substrate-derived control of dendrite growth. To test this hypothesis, we assayed effects of epithelial endoreplication on dendrite growth. First, we monitored dendrite growth in larvae homozygous for reduction of function mutations in *dup* or *rap,* which significantly attenuate epithelial endoreplication (Figure 1.2 J). In both

mutants, larval C4da neurons exhibited exuberant late-stage dendrite growth similar to *ban* mutants (Figure 1.3 C, G). Likewise, sustained epithelial expression of *Cyclin E*, which inhibits progress through endoreplication cycles (Weiss et al., 1998), caused dendrite defects similar to *ban* mutants (Figure 1.3 D, G), demonstrating that epithelial endoreplication is necessary for modulation of C4da dendrite growth. Finally, overexpression of *ban* or *dm*, which increases epithelial endoreplication, dampened late stage dendrite growth, leading to a decrease in body wall dendrite coverage and midline occupancy (Figure 1.3 E-G), consistent with a role for epithelial endoreplication in constraining dendrite growth. As with epithelial *ban* overexpression (Parrish et al., 2009), epithelial *dm* overexpression led to dendritic "wrapping" of epithelial cells (arrowheads), possibly reflecting tighter coupling between dendrites and epithelial cells (Figure 1.3 F, G). Whereas wild type C4da dendrites were confined to a thin cross-sectional area along the basal surface of epithelial cells (Figure 1.3 F' and Han et al., 2012; Kim et al., 2012), epithelial *dm* or *ban* overexpression caused dendrites to occupy a larger 3-dimensional area, particularly in regions exhibiting the "wrapping" behavior (Figure 1.3 F').

Our results thus far indicate that *ban* promotes endoreplication in epithelial cells and that epithelial endoreplication is involved in coordination of C4da dendrite and substrate growth. To test whether the requirement for *ban* in dendrite growth involves epithelial endoreplication, we examined the epistatic relationship between *ban* and endoreplication machinery. First, we assayed for genetic interactions between *ban* and *dup*. On its own, heterozygosity for mutations in either gene has no significant effect on dendrite coverage, but larvae doubly heterozygous for mutations in *ban* and *dup* exhibited modest but significant increases in dendrite coverage (Figure 1.3 H), suggesting

that *ban* and the endoreplication effector *dup* function in a genetic pathway to regulate dendrite growth. Second, we overexpressed *ban* in *dup* mutant larvae and found that reduction of *dup* function blocked the effects of epithelial *ban* overexpression on dendrite growth (Figure 1.3 I), demonstrating the requirement for endoreplication in *ban*-mediated dendrite growth control. Third, we overexpressed *dm* in epithelial cells of *ban* mutant larvae, taking advantage of the temperature-sensitive nature of the Gal4-UAS system to drive *dm* expression at different levels. Consistent with *dm* functioning downstream of *ban* to promote endoreplication and constrain dendrite growth, *dm* expression suppressed the dendrite overgrowth of *ban* mutants in a dose-dependent fashion (Figure 1.3 J, K). Altogether, these results demonstrate that *ban* regulates epithelial endoreplication to modulate dendrite growth.

1.2.3 Developmental control of dendrite-epithelia interactions

Increased epithelial endoreplication alters the relative position of dendrites and epithelial cells (Figure 1.3 F; Parrish et al 2009), therefore we hypothesized that epithelial endoreplication affects dendrite-substrate interactions by promoting epithelia-dendrite adhesion, modulating permissivity of the ECM to dendrite growth, or some combination of the two. Using a genetically-encoded proximity sensor, high resolution confocal imaging of dendrite/ECM markers, and transmission electron microscopy (TEM) of the dendrite/epithelia interface we examined whether dendrite/epithelia interactions change over a developmental time course in response to *ban* signaling and endoreplication.

GFP reconstitution has been used to map synaptic contacts, a technique known as GFP reconstitution across synaptic partners (Feinberg et al., 2008). Here, we used GFP reconstitution as a proximity detector (GFP-PD) to monitor dendrite-epithelia apposition

with the underlying hypothesis that an increase in dendrite-epithelia adhesion would be manifest as an increase in dendrite-epithelia proximity. Based on physical dimensions of the components (Becker et al., 1989; Morell et al., 2008), GFP reconstitution in this system indicates dendrite-substrate proximity of <30nm, a distance spanned by known adhesion molecules (Figure 1.4 A). GFP reassembly occurs slowly (>tens of minutes; (Pédelacq et al., 2006), thus dendrite-epithelia apposition must be stable to generate GFP-PD signal

To monitor dendrite-epithelia juxtaposition we expressed one half of the proximity sensor in C4da neurons and the other half in epithelial cells. In newly eclosed 1st instar larvae, prior to the larval surge in epithelial endoreplication, GFP-PD signal was almost undetectable (Figure 1.4 B). Epithelial ploidy rapidly increases beginning in 2nd instar larvae, and we likewise observed dendritic accumulation of GFP-PD beginning in 2nd instar larvae (Figure 1.4 C). Epithelial overexpression of *ban* or *dm* led to a significant increase in GFP-PD in 2nd instar larvae (Figure 1.4 D, F and G), suggesting that endoreplication promotes dendrite-epithelia juxtaposition. Conversely, *dup* mutant larvae exhibited a decrease in GFP-PD signal that was most pronounced in terminal dendrites (Figure 1.4 E-G). We therefore conclude that epithelial endoreplication is necessary and sufficient to trigger developmental changes in dendrite-epithelia juxtaposition.

GFP-PD signal was apparent throughout the majority of the dendritic arbor in 3rd instar larvae (Figure 1.4 H), suggesting that close apposition, and likely adhesion, of dendrites and epithelial cells progressively increases throughout larval development. However, GFP-PD signal was unevenly distributed and markedly reduced/absent from

many terminal dendrites, suggesting that dendrite-epithelia apposition varies in different regions of the dendritic arbor, with the most dynamic portions of the arbor (terminal dendrites) coupled to epithelial cells to a lesser degree (Figure 1.4 H). Epithelial overexpression of *ban* or *dm*, on the other hand, led to increased levels of GFP-PD signal throughout the dendrite arbor, including terminal dendrites (Figure 1.4 I), consistent with a role for epithelial endoreplication in promoting dendrite-epithelia adhesion.

Larval C4da dendrites grow along the basal surface of epithelial cells, attached to the ECM by virtue of dendritic integrins, with a small proportion of dendrites embedded in epithelial cells (Han et al., 2012; Kim et al., 2012). Based on our observation that dendritic and epithelial membranes become more closely juxtaposed as larval development progresses, we hypothesized that dendrite-ECM interactions might be developmentally regulated as well. Using high-resolution confocal imaging combined with deconvolution (Han et al., 2012), we monitored co-localization of dendrites and ECM components tagged with GFP by exon traps, including Collagen IV (*vkg-gfp* (Figure 1.5 ; Morin et al., 2001). In 1st instar larvae, we found that, on average, >98% of dendrites co-localize with ECM markers (Figure 1.5 A, G), but 12% of dendrites in 3rd instar larvae were detached from the ECM and apically shifted (Figure 1.5 B, G); these apically shifted dendrites are likely embedded in epithelial cells (Han et al., 2012). A significantly reduced proportion of dendrites were detached from the ECM in *ban* or *dup* mutant 3rd instar larvae, whereas epithelial *ban* or *dm* overexpression caused a significant increase in apical ECM detachment of dendrites (>25% of dendrites; Figure 1.5 C-G). Taken together, these results demonstrate that dendrite-epithelia proximity and dendrite-epithelia interactions (embedding) are developmentally regulated by epithelial

endoreplication. Thus, after dendritic coverage of the body wall is established, dendrites become increasingly coupled to epithelial cells.

To corroborate our finding that dendrite-epithelia interactions are developmentally regulated by endoreplication, we examined dendrite-epithelia interactions using TEM. In thin sections of abdominal segments cut along the apical-basal axis of the body wall, we monitored distribution of dendrites (identified as processes containing arrays of multiple parallel microtubules near the basal epithelial surface) and the frequency of plasma membrane invaginations, as internalized dendrites are frequently found in membrane invaginations (Han et al., 2012; Kim et al., 2012). In newly eclosed 1st instar larvae, most dendrites were positioned at the surface of epithelial cells in direct contact with the ECM; only 3/50 dendrites were enclosed in epithelial cells (Figure 1.5 H). We observed a substantial increase in the proportion of epithelia-embedded dendrites in 3rd instar larvae (27/91 dendrites; Figure 1.5 H). Thus, dendrite-epithelia interactions change substantially from early larval development when dendrites are establishing body wall coverage to late larval development when dendrites are expanding proportionally with their substrate. Mutations that inhibited endoreplication (including *ban*) blocked the developmental increase in epithelial plasma membrane invagination and dendrite enclosure, whereas treatments that increased epithelial endoreplication (*ban* or *dm* overexpression) had the opposite effects (Figure 1.5 H). These findings confirm our results using a GFP-based proximity sensor and our *in vivo* imaging of dendrites and the ECM; altogether, these studies indicate that interactions between dendrites and epithelial cells are developmentally regulated and that endoreplication in epithelial cells is a critical component of this control.

Next, we set out to identify molecular mediators of this developmentally regulated change in dendrite-epithelia interactions. Most adhesion-related transcripts that were dysregulated in *ban* mutants were differentially expressed in 1st and 3rd instar epithelial cells, consistent with *ban* playing a role in developmental control of epithelial adhesion (Figure 1.6 A). We therefore examined whether expression of these adhesion-related genes were responsive to endoreplication. Notable among these transcripts were *mys*, which encodes the lone somatically-expressed *Drosophila* β-integrin, and *hep*, which encodes a *Drosophila* JNK kinase; integrins are key mediators of cell-ECM interactions and play established roles in adhesion of the epidermis to the basement membrane (DiPersio et al., 1997), and JNK activity regulates adhesive properties of *Drosophila* epithelial cells, in part by regulating cadherin-based adhesion (Jacinto et al., 2000; Jasper et al., 2001; Martin-Blanco et al., 2000). Epithelial protein levels of Mys, in particular on the basal surface of epithelial cells outside of the basolateral junctional domain (Figure 1.6 B; arrows, adherens junctions) significantly increased during larval development, concomitant with the rapid increase in larval endoreplication, suggesting that increased Mys expression may be coupled to endoreplication. Indeed, the increased Mys expression was dampened by mutations that reduced endoreplication (*ban*, *dup*, or *rap*), and epithelial overexpression of *ban* or *dm*, which increase endoreplication, further enhanced Mys levels (Figure 1.6 B). Thus, developmental changes in epithelial expression of adhesion-related genes are triggered by endoreplication. We therefore hypothesized that endoreplication affects dendrite growth via these changes in epithelial expression of adhesion-related genes and we tested this by monitoring the role that epithelial integrins play in regulating dendrite growth.

1.2.4 Epithelia-ECM interactions influence dendrite growth and plasticity

To examine whether epithelial integrins influence dendrite growth, we expressed *UAS-mys(RNAi)* in epithelial cells, which effectively attenuated epithelial Mys protein levels ,and monitored effects on dendrite patterning in 3rd instar larvae. As shown in Figure 1.6 C and 6F, epithelial *mys(RNAi)* caused exuberant late stage dendrite growth beyond established boundaries similar to *ban* mutants or other endoreplication-defective mutants, albeit to a lesser extent. As a result, dendrites occupied larger than normal territories. Thus, the progressive increase in Mys expression, which mediates ECM attachment, contributes to coordination of dendrite and epithelial growth by constraining late-stage dendrite growth. One model to account for this finding is that increased epithelia-ECM attachment makes the ECM less permissive to dendrite growth. Alternatively, increased epithalia-ECM attachment may potentiate other epithelia-dendrite contacts that constrain dendrite growth.

To ascertain whether developmental control of Mys expression is a functionally relevant output of *ban* in regulating dendrite growth, we examined the epistatic relationship between epithelial *ban* and *mys* in control of C4da dendrite development. First, we simultaneously overexpressed *ban* and knocked down *mys* in epithelial cells and found that *mys(RNAi)* attenuated the dendrite growth defect of *ban* overexpression, resulting in dendrite overextension beyond normal boundaries (Figure 1.6 D, F). Second, we assayed effects of epithelial overexpression of integrins (*UAS-mys* + *UAS-inflated*) on dendrite growth and found that integrin overexpression caused a dendrite undergrowth phenotype similar to *ban* or *dm* overexpression (Figure 1.6 E, F). Third, we overexpressed integrins in *ban* mutant larvae and found that epithelial integrin

overexpression only partially suppressed the dendrite overgrowth of *ban* mutants (Figure 1.6 F). We conclude that increased epithelial Mys expression is necessary but not sufficient for *ban*-mediated control of dendrite growth. Taken together with our observation that modulating integrin expression causes less severe dendrite defects than modulation of *ban* or endoreplication, these results suggest that additional epithelial-derived factors contribute to *ban*-mediated, and hence endoreplication-dependent epithelial control of dendrite growth.

Synchronization of dendrite and substrate growth is accompanied by progressive restriction in C4da dendrite structural plasticity (Parrish et al., 2009). Prior to establishment of tiling, ablating C4da neurons leads to exuberant dendrite growth into unoccupied territory by spared neurons (Grueber et al., 2003; Parrish et al., 2009; Sugimura et al., 2003). This invasive growth potential is lost concomitant with the onset of epithelial endoreplication. We therefore hypothesized that developmental restriction in structural plasticity of C4da dendrites is the result of alterations in dendrite-substrate and dendrite-epithelia interactions triggered by epithelial endoreplication, including increased proximity between dendrites and epithelial cells. Consistent with this notion, when we monitored structural plasticity following laser ablation of a C4da neuron, we found that invading dendrites were less closely associated with epithelial cells than neighboring non-invading dendrites, as assessed by relative levels of GFP-PD intensity (Figure 1.7 A-D).

ECM modification plays important roles in regulating dendrite structural plasticity in several contexts (Mataga et al., 2002; Oray et al., 2004; Yasunaga et al., 2010), thus we reasoned that the *ban*-regulated developmental changes in epithelia-ECM attachment

might alter substrate permissivity for dendrite growth and hence regulate C4da dendrite plasticity. To test this possibility, we ablated Cd4a neurons just after the $1^{st}/2^{nd}$ instar transition and monitored the extent of coverage of the unoccupied territory by dendrites of neighboring neurons. In this paradigm, wild type dendrites exhibit little invasive activity, covering an average of 10% of the territory previously occupied by the ablated neuron (Figure 1.7 D, H). By contrast, when we ablated C4da neurons in *dup* mutant larvae, which are defective in endoreplication and the associated developmental changes in dendrite-epithelia interactions, we observed robust invasive activity comparable to *ban* mutants (Figure 1.7 E, H). Likewise, when we blocked the increase in Mys levels via epithelia-specific *mys(RNAi)*, we observed a significant potentiation of dendrite invasion (Figure 1.7 F-H). Notably, mutations in *ban* or *dup* potentiate dendrite invasion to a greater degree than *mys(RNAi)* (Figure 1.7 G, Parrish et al., 2009), suggesting that factors other than *mys* function downstream of endoreplication to control dendrite expansion. We conclude that the developmentally programmed growth transition to endoreplication in epithelial cells regulates substrate permissivity for dendrite growth, in part by regulating epithelia-ECM interactions.

1.3 DISCUSSION

1.3.1 Local and systemic control of dendrite growth

During embryonic and early larval development, C4da dendrites expand faster than their substrate to achieve complete body wall coverage. C4da neurons respond to nociceptive stimuli, and the rapid dendrite growth in embryonic and early larval development ensures that the larval body wall is completely covered by these sensory dendrites shortly after hatching, when the larvae must interact with their surroundings. Subsequently, C4da dendrites expand synchronously with body wall epithelial cells as larvae continue to grow to maintain proportionality (Figure 1.8 A). Thus, multiple growth signals are likely at

work in this system. First, in response to systemic growth cues, dendrites and epithelial cells continuously expand during embryonic and larval development. Blocking these growth cues, for example by ablating dILP neurons or globally compromising insulin signaling similarly affects both neuron and substrate, resulting in growth-arrested larvae with properly scaled dendrite arbors (Parrish et al., 2009). Beginning at the $1^{st}/2^{nd}$ instar transition, sensory neurons and epithelial cells respond differently to these growth cues: epithelial growth relies on endoreplication while sensory neuron growth does not (Figure 1.8 B). During this latter period of larval growth when dendrites and substrate expand proportionally, epithelial-derived signals constrain dendrite expansion to ensure synchronous growth of dendrite and substrate. We previously found that larval activation of *ban* in epithelial cells is an essential component of this signaling cascade (Parrish et al., 2009), and here we demonstrate that *ban* functions in epithelial cells to regulate endoreplication. By altering adhesive properties of epithelial cells and hence epithelia-ECM and epithelia-dendrite interactions, endoreplication serves to curtail C4da dendrite growth and structural plasticity (Figure 1.8 C). Many types of neurons must expand their arbors in concert with their substrate to maintain proportional coverage of their receptive field; developmental control of substrate adhesion may be similarly regulated in other contexts to ensure proper coupling of dendrite and substrate growth, and to regulate structural plasticity of dendrites.

1.3.2Endoreplication in nervous system development

Growth control is particularly complex in the nervous system where different cell types are continuously incorporated and many neurons/support cells must grow while maintaining connections. In some contexts, programmed polyploidy facilitates neuronal growth. For example, in the terrestrial slug *Limax valentianus* endoreplication occurs throughout the nervous system in proportion to animal growth, presumably to facilitate neuron expansion (Yamagishi et al., 2011). Although neuronal polyploidy is more widely documented in invertebrates than vertebrates, tetraploid neurons exist in the retina and in

the cortex (López-Sánchez and Frade, 2013; Morillo et al., 2010), and numerous studies suggest that Purkinje neurons may be polyploid.

In addition to supporting neuronal growth, developmentally regulated polyploidy (endoreplication) is a well-suited solution for tissue growth in circumstances where division might disrupt patterning or connectivity. For example, endoreplication allows glial cells that wrap the *Drosophila* ventral ganglion to maintain the integrity of the blood-brain barrier even as they grow to accommodate brain expansion (Unhavaithaya and Orr-Weaver, 2012). Likewise, we have shown that endoreplication of epithelial cells allows for substrate growth without cell divisions that might disrupt body wall innervation. In addition, this epithelial endoreplication drives a differentiation program that regulates epithelia-dendrite interactions to influence sensory dendrite growth and patterning. Notable among these interactions is an increase in embedding of dendrites in epithelial cells. Epithelial embedding of these dendrites may serve a number of purposes. First, as suggested in prior studies, embedding may have functional consequences (Han et al., 2012; Kim et al., 2012). Second, embedded dendrites may provide points of contact that constrain dendrite expansion. Third, the embedding may also facilitate the generation of tensile forces as the body wall expands and such forces could contribute to dendrite growth, analogous to axon elongation in response to mechanical tension (Bray, 1984). How genome amplification potentiates certain signaling pathways is not known, but *Drosophila* endoreplication entails underreplication of specific genomic regions in a cell type-specific manner (Sher et al 2012), thus endoreplication may facilitate expression of cell type-specific differentiation programs in eplithelial cells and in other contexts. It

remains to be seen whether endoreplication regulates substrate or target-derived signals that influence neuron growth and patterning in other systems as well.

1.2.3 Substrate control of dendrite plasticity

Here, we demonstrate that dendritic structural plasticity is tied to growth control. We found that alterations in adhesive properties of the substrate constrain dendritic structural plasticity in C4da neurons concomitant with proportional expansion of dendrites and substrate. First, decreased plasticity is accompanied by increased dendrite-epithelia proximity during development; manipulations that increase plasticity decrease dendrite-epithelial proximity, and vice-versa. Second, epithelial embedding of dendrites, which may serve to physically tether dendrites to epithelial cells, increases as the capacity for structural plasticity decreases, and manipulations that increase dendritic plasticity decrease the prevalence of epithelia-embedded dendrites. Third, epithelial expression of adhesion molecules changes as dendritic structural plasticity is restricted and epithelial integrin expression contributes to restriction of plasticity. Large-scale plasticity would seem to be incompatible with synchronous growth of neurons and their substrate, so it will be intriguing to see whether dendritic plasticity is broadly constrained during periods of growth that maintain proportionality.

1.4 MATERIALS AND METHODS

1.4.1 Live Imaging

Embryos were collected on yeasted grape juice agar plates and aged at 25˚C in a moist chamber. At the appropriate time, a single embryo/larva was mounted in 90% glycerol under coverslips sealed with grease and imaged using a Leica SP5 microscope with a 40x 1.25NA lens. For quantitation of dendrite phenotypes, image stacks of dendrites in

segments A2-A4 were captured from 8-10 larvae. For high-resolution confocal imaging of the dendrite-ECM interface, larvae were anesthetized with ether prior to mounting and image stacks with a 0.2um Z step size were acquired.

1.4.2 GFP reconstitution

GFP proximity detection (GFP-PD) is based on the previously described GRASP constructs (Feinberg et al.) using extracellular GFP fragments tethered to the transmembrane carrier protein CD4. Briefly, CD4-spGFP1-10 was PCR amplified and cloned into pUAST containing an in frame C-terminal mCerulean tag. Transgenic lines were obtained from BestGene (Chino Hills, CA) and tested for expression. The *UAS-spGFP1-10-CD4-mCer* line was recombined with the previously described *ppk-spGFP11-CD4-tdTomato* line (Han et al., 2012). Epithelia-dendrite GFP reconstitution was monitored by using the epithelium specific *A58-Gal4* driver to express *UAS-spGFP1-10-CD4-mCer* in combination with the C4da neuron-specific *ppk- spGFP11-CD4-tdTomato* transgene. GFP-PD signal was imaged under the same conditions for all samples of a given time point, taking care to avoid pixel saturation. Mean pixel intensity was measured using ImageJ (NIH).

1.4.3 Laser Ablation

A single larva was mounted, as for live imaging, and the nucleus of a C4da neuron was targeted under a 100x 1.4NA objective using a 337nm pulsed nitrogen laser (Andor Micropoint; 12 Hz, 15 sec) mounted on a Leica DM550 microscope. Following ablation, animals were recovered to cornmeal agar and imaged 48hr later.

1.4.4 Immunohistochemistry

Larval fillets were dissected/processed as described (Grueber et al., 2002) and stained with the following antibodies: HRP conjugated with Cy2 or Cy3 (1:200; Jackson labs), mCD8 (1:100; Life Tech.), phospho-D-Akt Ser505 (1:500; Cell Signaling), Myospheroid CF.6G11 (1:20; Developmental Studies Hybridoma Bank), BrdU (1:250; Abcam), phospho-JNK (1:500; Cell Signaling), DAPI (50ng/mL; Life Tech.) and secondary antibodies from Jackson labs. For BrdU labeling, larvae were fed cornmeal-molasses fly food containing BrdU (10μg/ml; Sigma), dissected in PBS, fixed in 4% formaldehyde/PBS, permeabilized in PBS-Tx, acid treated with 2.5N HCl for 30min, neutralized with 100mM Sodium tetraborate, and processed for immunostaining.

1.4.5 Transmission Electron Microscopy

Larvae were perforated with insect pins to improve fixative penetration and fixed in 2.5 % glutaraldehyde/0.1M sodium cacodylate buffer with centrifugation at 15,000 RPM for 1hr. Fixed tissue was washed 4x5min in PBS and post-fixed at 4C in buffered 2% osmium tetroxide. The following day, samples were spun at 12,500 RPM for 1hr to enhance fixative penetration, washed with distilled water in 20ml scintillation vials (3x20min), and dehydrated in a graded series of ethanol, followed by two changes of propylene oxide. This was followed by infiltration in a 1:1 mixture of propylene oxide:epon araldite epoxy resin overnight, two changes (2hr each) in epon araldite, and overnight polymerization in a 60 degree celsius oven. 70 nm sections were cut, stained with Reynolds lead citrate, and viewed on a JEOL 1230 transmission electron microscope equipped with an AMT XR 80 eight megapixel camera.

1.4.6 Fluorescence-activated cell sorting (FACS)

Larvae were filleted in PBS and the tissue containing cells of interest was dissected away from all other tissues. Dissection time was limited to 30min per sample, and following dissection cell suspensions were prepared in 5 volumes of PBS/2x trypsin via 3 cycles of the following: triturate 10x through a 1000 microliter pipet tip, mix 5min at 1000 rpm in a 37°C microtube mixer. Cell suspensions were filtered through a 70um cell strainer and sorted on a FACSAria II (BD). GFP^+ non-autofluorescent events were sorted into RNAqueous-Micro Lysis buffer (Life Tech.) and frozen on dry ice.

1.4.7 RNA isolation, amplification, and microarray hybridization

RNA was isolated from FACS-sorted samples using an RNAqueous-Micro kit (Life Tech.) and DNase-treated. All RNA samples were subjected to two rounds of linear amplification using the Aminoallyl MessageAmp II kit (Life Tech.). Dye-coupled aRNA was fragmented and hybridized to custom-designed microarrays (Agilent).

1.4.8 Microarray design

We designed two 60-mer oligonucleotide probes for each of the 20,726 coding sequences in the annotated fly genome (release 5.2) using ArrayOligoSelector (Bozdech et al., 2003), resulting in 35,272 successful probe designs, 16,717 additional probes against alternatively spliced transcripts, and 546 probes targeting non-coding RNA (244 snoRNA, 108 tRNA, 24 snRNA, 74 rRNA, 3 miRNA, 93 other). The final probe set was filtered to remove redundant probes, overlapping probes, and those with cross hybridization potential (based on a -21.6 kcal/mol threshold, which was chosen to fit the number of probes allowed in the Agilent 4 x 44k design specification). This resulted in 33,792 probes to CDS, 8744 probes to alternatively spliced transcripts, and 546 RNA probes. In total, 43,803 probes were included in the design.

1.4.9 Microarray scanning, feature extraction, normalization, and filtering

Microarrays were scanned on an Axon 4000B scanner and feature information extracted in GenePix 6 (Molecular Devices). GPR files were uploaded into Acuity (Molecular Devices) and ratio normalized. Data was retrieved using quality filters for reference channel intensity, background intensity, pixel saturation, pixel variance, feature diameter, % pixel intensity over background, and feature circularity. "Ratio of Medians" data was further filtered for 70% present data, Cy5 net median intensity > 350 across a minimum of 3 arrays, Cy3 net median intensity > 150 across a minimum of 20 arrays. Expression ratios were $\log_2$ transformed, arrays median centered, quantile normalized, and genes median centered before analysis.

1.4.10 Measurements

Dendrite branching metrics: To measure dendrite coverage, we used three indices. The coverage index represents the portion of the larval body wall covered by dendrites of a single neuron in dorsal hemisegments bounded by muscle attachment sites (apodemes; anterior/posterior boundaries), the dorsal midline (dorsal boundary) and a line connecting a neuron of interest to the corresponding neuron in the adjacent segments (ventral boundary). A dendrite that completely covers the dorsal hemisegment would have a coverage index of 1 whereas a dendrite that covered the entire dorsal hemisegment and territory of neighboring hemisegments would have a coverage index of > 1. The Invasion Index represents the portion of a dorsal hemisegment that is covered by dendrites of neurons from neighboring hemisegments. Midline occupancy represents the dendrite density at the midline and is expressed as dendrite length/unit area (μm dendrite

length/1000μm^2). 2D projections of Z-stacks were used for computer-assisted dendrite tracing (Neurolucida), and features of the arbor were measured using the traces.

DNA content: DAPI quantitation was as described (Unhavaithaya and Orr-Weaver, 2012). Briefly, DNA amount was quantified using ImageJ (NIH) to measure pixel densities. Nuclear DAPI intensity was measured in each optical section (500nm Z-slices) of Z-stacks and ploidy was calculated by normalizing to mean DAPI intensity value of 10 diploid PNS neurons from the same fillet imaged using identical settings. DAPI intensity values for PNS neurons within a sample/across different samples varied by less than 10%.

Cell Size: To measure epithelial cell size, we traced the outline of Nrx-IV-GFP or anti-Mys immunoreactivity for at least 50 epithelial cells of each genotype using ImageJ (NIH). We obtained similar results when we used Imaris to construct 3D renderings epithelial cells and calculated the volume of these rendered cells.

1.4.11 Statistical Analysis

Differences between group means were analyzed via ANOVA with a post hoc Dunnett's test. Significance of microarray expression differences was calculated using Statistical analysis of microarrays (SAM) (Tusher et al., 2001) using a false discovery rate of 5% and fold-change threshold of 1.5-fold.

Chapter 2. Super resolution imaging of Drosophila tissues using expansion microscopy

2.1 INTRODUCTION

Analysis of intercellular interactions and intracellular structures often requires optical resolution that is below the diffraction limit of light (~250nm). While many methods have been developed for super-resolution imaging of biological samples, Expansion Microscopy (ExM) has the advantage that it is compatible with standard optical microscopes and can be used with a wide range of fluorophores. ExM relies on physical expansion of samples to effectively increase imaging resolution, allowing for a ~4-fold increase in lateral resolution (Chen et al., 2015; Chozinski et al., 2016; Ku et al., 2016; Tillberg et al., 2016). ExM has been applied primarily to cells in culture, though several studies demonstrate its utility in analysis of tissues and organs (Chen et al., 2015; Chozinski et al., 2016; Ku et al., 2016). However, broad implementation of ExM to analysis of complex tissues and even whole organisms is complicated by the potential that different tissues will exhibit different rates of expansion and differential susceptibility to proteolytic digestion. In particular, many invertebrates, fungi, and plants are covered with a rigid exoskeleton that is important for maintaining organismal integrity. In some of these organisms including Drosophila, this exoskeleton is comprised of a rigid lipid and polysaccharide-rich cuticle that is refractory to conventional proteolytic digestion and hence prevents a major impediment to implementation of expansion microscopy.

Here, we set out to extend the utility of ExM by adapting it for use in Drosophila. We find that Drosophila tissues lacking a rigid cuticle are compatible with established protocols for ExM and reliably expand with minimal distortion. Although the cuticle

disrupts expansion of body wall preparations, enzymatic digestion of the cuticle renders both larval and adult body wall tissue compatible with ExM. We find that ExM yields a lateral resolution of ~80 nm in Drosophila tissue, allowing for analysis of structural elements that cannot be observed with conventional optical microscopy, and demonstrate the utility of this approach in three experimental contexts. First, we show that ExM allows for high-resolution analysis of presynaptic active zone (AZ) structure at the larval NMJ and that analysis of these structures with conventional confocal microscopy leads to systematic sampling errors. Second, using ExM to study AZ structure in adults, we identify age-dependent changes in AZ structure. Finally, we used ExM to analyze cell-cell interactions in the larval peripheral nervous system and, as a result of the increased axial resolution afforded by ExM, we show that epidermal enclosure of somatosensory dendrites is significantly more prevalent than previously reported, underscoring the likely importance of this intercellular interaction. Altogether, these studies establish ExM as an accessible super-resolution imaging platform that can be applied to analysis of diverse Drosophila tissues.

2.2 RESULTS AND DISCUSSION

2.2.1 Expansion of Drosophila tissues with minimal distortion

Prior studies demonstrated that some tissues are amenable to ExM (Chen et al., 2015; Chozinski et al., 2016; Ku et al., 2016), but given the prevalence of whole mount imaging in analysis of Drosophila embryonic development, we wanted to determine whether ExM could be used for analysis of in tact Drosophila embryos. The Drosophila cuticle is first deposited at late embryonic stages, after which it progressively thickens (Ostrowski et al., 2002). This cuticle provides a barrier to antibody access at late embryonic and larval

stages and is largely composed of chitin, which we reasoned would likely be refractory to the protease treatments used in prior implementations of ExM. We therefore investigated whether embryos that lacked a rigid cuticle were compatible with ExM. To this end, we fixed Drosophila embryos using a heptane/formaldehyde fixative and processed the embryos for ExM, which includes gelation, digestion, and expansion (Figure 2.1 A). Using this approach, Drosophila embryos were readily expanded up to ~4x without obvious tearing or distortion of samples (Figure 2.1 B). To directly assess the fidelity of expansion, we conducted correlative imaging analysis of stained whole mount Drosophila embryos before and after expansion, measured the expansion factor in post-expansion images, and analyzed distortion by digitally expanding pre-expansion images and comparing them to post-expansion images (Figure 2.1 B). For these experiments, we stained embryos with the monoclonal antibody 22C10 (Zipursky et al., 1984), which labels sensory neurons, and Alexa488-conjugated secondary antibodies. After staining, we treated the stained tissue with the amine-reactive small molecule MA-NHS (methacrylic acid N-hydroxy succinimidyl ester) to preserve fluorescence signal (Chozinski et al., 2016). We found that distortion was generally below 300nm (root mean square distance) over length scales of up to 10μm, comparable to results reported for other tissue samples (Chen et al., 2015; Chozinski et al., 2016; Ku et al., 2016; Tillberg et al., 2016).

Next, we examined the compatibility of isolated Drosophila tissue with ExM. Similar to embryos, formalehyde-fixed larval brains were readily expanded without gross distortion. Indeed, larval brains stained with anti-FasII antibody (Hummel et al., 2000) exhibited axial distortion that was generally below 500nm (root mean square distance)

over length scales of up to 10μm.

Unlike embryo and larval brain samples, larval body wall samples exhibited extensive tearing and distortion during expansion, likely a result of incomplete digestion of the larval cuticle. Chitin, a polysaccharide, is the major component of the Drosophila cuticle, so we reasoned that treatment with chitinases, which are produced during molting to digest the cuticle (Winicur and Mitchell, 1974) and have recently been used to promote antibody access to in tact larval preparations (Manning and Doe, 2017) might dissociate larval tissue from the cuticle and facilitate expansion. Indeed, addition of a single chitinase digestion step after gelation allowed for expansion of larval body wall samples without tearing or obvious distortion of tissue (Figure 2.1 C). Correlative image analysis indicated that body wall samples exhibited low levels of distortion, comparable to embryo and larval brain samples, demonstrating that chitinase treatment had little effect on tissue integrity. Finally, we found that chitinase treatment allowed for isometric expansion of adult body wall samples as well (see below), suggesting that this approach may be broadly useful for ExM on samples with a chitin-rich exoskeleton, including other arthropods and fungi. Altogether, these results demonstrate that ExM is applicable to different types of Drosophila tissues and that fine structural elements are preserved during expansion of complex cellular assemblies including whole embryo preparations.

2.2.2 Super-resolution imaging of subcellular structures with ExM

We next examined whether ExM would facilitate identification of fine structural details in Drosophila tissue that were not observable with standard confocal microscopy. To this end, we first used ExM to visualize mitochondrial morphology as mitochondrial morphology is dynamic during development, altered in a broad range of disease states

(Pernas and Scorrano, 2016), and commonly studied with routine fluorescence microscopy. We expressed a form of GFP that is targeted to the mitochondrial matrix (UAS-mitoGFP) specifically in Drosophila class IV dendrite arborization (C4da) neurons, which innervate the body wall, and processed larval body wall samples for ExM with anti-GFP antibodies to visualize mitochondrial morphology. Confocal imaging of unexpanded tissue revealed a blurry filamentous network of structures. (Figure 2.2 A) Detailed structures, such as mitochondrial branches (Figure 2.2 A"), couldn't be distinguished especially from the orthogonal view (Figure 2.2 A'). In expanded tissue, the mitochondria appeared as a more highly interconnected network that was less uniform in diameter, with loops, branches, and frequent swellings visible (Figure 2.2 B, B', B''). Thus, ExM allows for visualization of fine structural elements in organelles and should prove to be a valuable tool in studying organelle morphogenesis.

We then used ExM to visualize the microtubule cytoskeleton. Although gluteraldehyde-containing fixatives performed well in ExM of cultured cells (Chozinski et al., 2016), gluteraldehyde-fixed larval body wall samples exhibited extensive distortion after expansion. In contrast, paraformaldehyde-fixed samples were uniformly expanded, and allowing for visualization of the intricate microtubule network in epithelial cells that was not discernable in unexpanded samples (Figure 2.2 D-E').

2.2.3 Super-resolution of presynaptic active zones with ExM

The Drosophila neuromuscular junction (NMJ) is a widely used model system for the analysis of glutamatergic synapses. Though conventional fluorescence microscopy has been used to study synapses at the NMJ, the diameter of glutamatergic synapses and feature size prevent accurate assessment of synapse number and structure at the NMJ

with conventional light microscopy. We reasoned that the increase in lateral resolution provided by ExM, compared to conventional microscopy, should allow facilitate analysis of synapse number and ultrastructure at the NMJ. Furthermore, analysis of NMJ synapses provides an opportunity to benchmark ExM against other super-resolution imaging platforms such as SIM, dSTORM and STED that have been successfully applied to analysis of presynaptic active zones at the NMJ (Ehmann et al., 2014; Fouquet et al., 2009; Jepson et al., 2014; Kittel et al., 2006; Lepicard et al., 2014; Matkovic et al., 2013).

The active zone (AZ) is a specialized structure at presynaptic terminals that serves as the site of neurotransmitter release. Structurally, the active zone can be identified by the dense collection of proteins called the cytomatrix at the active zone (CAZ), which includes Bruchpilot (Brp), a major structural component of the CAZ (Kittel et al., 2006; Wagh et al., 2006). Antibodies that recognize the C-terminus of Brp (mAb Nc82) label hollow ring-like structures ~200-400 nm in diameter (Ehmann et al., 2014; Kittel et al., 2006; Wagh et al., 2006), the walls of which exhibit a full width half maximum of approximately 80 nm with discrete foci of Brp immunoreactivity aligning in a circular array (Fouquet et al., 2009). To examine the utility of ExM in analysis of AZ structure, we conducted correlative pre- and post-expansion analysis of Brp immunostaining at the NMJ of third instar larvae. Using conventional confocal microscopy, Brp immunoreactivity appeared as solid structures ranging in size from ~300 to 500 nm in diameter and 100 to 300 nm2 in area (Figure 2.3 A). These structures exhibited either uniform signal intensity or a central maximum in intensity. Following expansion, we noted several key differences in apparent structure of AZs. First, the shapes of the AZs were less regular; whereas the puncta in pre-expansion samples were largely spherical,

many puncta in post-expansion samples were elliptical, elongated, and/or contained multiple distinct lobes. Second, the AZs were uniformly smaller in post-expansion samples than the apparent size in pre-expansion samples (Figure 2.3 C). Third, many sites of Brp immunoreactivity that appeared as individual structures under standard confocal imaging were resolved into multiple independent sites of Brp immunoreactivity (Figure 2.3, A', A", B' and B"), suggesting that quantitative analysis using confocal imaging likely results in underscoring of AZ numbers. Indeed, ratiometric analysis of AZ number in confocal images of pre- and post-expansion tissue indicated that ExM consistently facilitated identification of larger numbers of AZs (Figure 2.3 D). Fourth, many of the Brp puncta in post-expansion samples were hollow ring-like structures (Figure 2.3, B and E). Finally, the maximum signal intensity of Brp immunoreactivity was concentrated in the periphery of many puncta in the post-expansion samples. Thus, our data demonstrates that ExM of the larval NMJ allowed for visualization of AZ substructure, including the hollow ring-like structures formed by the active zone protein Bruchpilot (Brp) previously revealed by super resolution imaging using the same anti-Brp antibody (Ehmann et al., 2014; Fouquet et al., 2009), and more accurate scoring of AZ number than conventional fluorescence microscopy.

To directly compare our results with ExM to another super-resolution imaging technique, we also imaged Brp immunostaining using structured illumination microscopy (SIM). (Figure 2.3 E) As we can see, ExM performs better than SIM. (Figure 2.3 H, I)

2.2.4 Age-dependent changes in AZ structure

We next investigated whether ExM could be used to resolve AZ structures at the CM9 NMJs located on the proboscis of the adult fly. Of note, the CM9 NMJs experience an

increase in neurotransmitter release during aging, but the cellular mechanisms underlying this potentiation of release are unclear (Mahoney et al., 2014). The size of the SV release event scales with the size of the presynaptic active zone (AZ) at numerous synapses including both small glutamatergic synapses of the CNS and large synapses like the NMJ (Gupta et al., 2016; Holderith et al., 2012; Propst and Ko, 1987; Südhof, 2012; Weyhersmüller et al., 2011). This includes changes in Brp levels at larval AZs during homeostatic plasticity (Weyhersmüller et al., 2011). Thus we wanted to investigate using ExM whether changes in the Brp staining pattern at the AZ could explain the age-dependent potentiation of neurotransmission at the CM9 NMJ.

CM9 NMJs were dissected from 10 day-old (10d), 30 day-old (30d), and 60 day-old (60d) adult virgin female flies and processed for immunostaining with anti-Brp antibody and subjected to ExM. We found that ExM successfully revealed Brp "rings" at the CM9 NMJ of the adult Drosophila and that these rings were similar to what we observed at the larval NMJ (Figure 2.4 B, D). We next investigated the structure of the Brp staining at each AZ and found a significant increase with age in the presence of AZs consisting of multiple Brp rings (Figure 2.4 F). The increase in AZs containing multiple rings was accompanied by a decrease in the percentage of AZs consisting of a single Brp ring (Figure 2.4 F). These results document an age-dependent change in AZ structure that is consistent with the potential fusion of neighboring AZs during the aging process that could not be resolved using standard epifluorescent microscopy. It is possible that these fused AZs have enhanced release given the likely increased abundance of voltage-gated calcium channels and larger pools of synaptic vesicles (SVs) (Cooper et al., 1996). These data are also supported by ultrastructural analysis of SV pool size and glutamate receptor

fields at the NMJs formed on the lateral abdominal muscles (VLMs) of the adult (Wagner et al., 2015). The spacing of the presynaptic AZs is directly influenced by the post-synaptic specialization especially the spectrin and actin cytoskeletons (Blunk et al., 2014; Pielage et al., 2006). Our data therefore suggests that changes in the post-synaptic cytoskeleton during aging could underlie the altered spacing of the AZs within the presynaptic nerve terminal.

2.2.5 Improved axial resolution with ExM

We next explored the potential utility of ExM for studying features of cell-cell interactions that are not observable with conventional confocal microscopy. Portions of dendrite arbors of C4da neurons, like peripheral arbors of other nociceptive sensory neurons, become physically embedded in the epidermis (Chalfie and Sulston, 1981; Han et al., 2012a; Kim et al., 2012; O'Brien et al., 2012). The extent of C4da dendrite embedding in the epidermis has been difficult to ascertain using optical microscopy because the size and spacing of sensory dendrites and epithelial membranes cannot be accurately measured as a result of poor axial resolution. And although TEM has proven useful in characterizing the architecture of C4da dendrite enclosure by the epidermis (Han et al., 2012a; Jiang et al., 2014; Kim et al., 2012), the difficulty of positively labeling cells of interest and the necessity for sampling a large surface area encompassing the dendritic territory of a single neuron have limited the utility of TEM in mapping the distribution or quantifying the extent of dendrite embedding in the epidermis. We reasoned that the increased resolution afforded by ExM would therefore allow for the most accurate analysis of C4da dendrite embedding to date.

C4da dendrites initially innervate the collagen-rich extracellular matrix on the basal side of the epidermis (Han et al., 2012a; Kim et al., 2012). During larval development, portions of the arbor become apically displaced and physically enclosed by epithelial cells (Jiang et al., 2014). Prior studies using high-resolution confocal imaging combined with deconvolution to monitor co-localization of dendritic membranes (labeled with the fluorescent reporter ppk-CD4-tdTomato) and components of the ECM tagged with GFP exon traps (Morin et al., 2001), revealed that a small portion (~10%) of the C4da dendrite arbor is apically displaced from the ECM and enclosed by the epidermis (Han et al., 2012a; Jiang et al., 2014). By contrast, a larger proportion of dendrites identified in TEM sections (>30%) were enclosed by the epidermis (Jiang et al., 2014), suggesting that confocal analysis underreports on the extent of epidermal enclosure of dendrites. However two factors prevent direct comparison of the TEM and confocal analyses. First, dendrites were identified in TEM as processes containing arrays of multiple parallel microtubules near the basal epithelial surface; portions of the arbor lacking microtubules would not be identified by this approach, and microtubules are not detectable at C4da dendrite terminals by fluorescence microscopy. Furthermore, although C4da neurons exhibit more extensive epithelial embedding than other somatosensory neurons (Kim et al., 2012), a subset of the dendrites identified in TEM sections may originate from other classes of da neurons. Second, TEM allows for sampling of a limited cross-sectional area, preventing systematic analysis of the distribution of epidermal enclosure across the entire C4da arbor. We therefore used ExM to determine the extent and distribution of C4da dendrite enclosure by the larval epidermis.

We double labeled the ECM and C4da dendritic membranes in larvae expressing the C4da-specific membrane marker ppk-mCD8-GFP with antibodies to GFP and the ECM component Perlecan (Friedrich et al., 2000) and measured epidermal dendrite enclosure using confocal microscopy of unexpanded and expanded tissue. Noticeably, ECM consists of many rigid components such as collagen, which cannot be broken down with proteinase during digestion. We found by using regular larval body wall expansion treatment, some ECM tearing and distortion happened, which gave us a dry-lake-bed-like ECM (Figure 2.5 B). Therefore, we introduced collagenase treatment after the proteinase digestion step. Compared to using ExM with no collagenase treatment, the ECM structure fidelity of ExM with collagenase treatment was largely improved (Figure 2.5 C). However the signal intensity of ECM after collagenase treatment was dampened.

In unexpanded tissues, we found that the vast majority of dendrites appeared to be in contact with the ECM (Figure 2.4 A'). Following tissue expansion, we observed several differences in the apparent size and orientation of dendrites and ECM. First, dendrites appeared as spherical structures with defined margins (Figure 2.5 C'). The ECM likewise appeared as a well-defined structure of nearly uniform thickness. Second, we were able to identify detached dendrites at a distance of 200 nm following expansion. By contrast, we failed to detect dendrite detachment from the ECM at distances of less than 550 nm prior to expansion (Figure 1.4 D). As a result of this increased axial resolution, imaging of post-expansion tissue revealed significantly more dendrite enclosure than conventional confocal analysis, with ~30% of the C4da dendrite arbor enclosed in the epidermis in post-expansion tissue. We likewise found that ~40% of

dendrites identified in TEM cross sections were embedded in the epidermis. These results also demonstrate the compatibility of ExM with multicolor labeling

2.3 MATERIALS AND METHODS

2.3.1 Fly stocks

Flies were maintained on standard cornmeal-molasses-agar media and reared at 25° C under 12 h alternating light-dark cycles. The following fly lines were used in this study: w1118 (BL6326); w1118; ppk-Gal4 (BL32079); w1118; UAS-mito-HA-GFP, e1 (BL8443); w1118, ppk-mCD8-GFP (Parrish et al., 2009).

2.3.2 Larval ventral nerve cord staining

3rd instar larvae were pinned dorsal side up on a sylgard plate (Dow Corning) and filleted along the dorsal midline. Brains were carefully removed using forceps, fixed in EM-grade paraformaldehyde (PFA; Electron Microscopy Sciences) freshly diluted to 4% final concentration in PBS for 30min at room temperature and washed 5x 5 min in PBSTx (PBS with 0.2% Triton X-100) before being blocked in blocking/permeabilization buffer (PBS with 5% BSA and 0.2% Triton X-100) for 30min. Samples were incubated with primary antibodies in blocking/permeabilization buffer overnight at 4° C, washed three times for 15 min each in PBST, and incubated for 6 h with secondary antibodies in blocking/ permeabilization buffer. After three 20 min washes in PBST, samples were treated with 1mM MA-NHS at room-temperature for 1 h followed by washing three times for 20 min each with PBS.

2.3.3 Whole mount embryo staining

Embryos were collected on yeasted grape juice agar plates for 4 h and aged at 25° C in a moist chamber for 10-14 h. Embryos were dechorionated in 50% bleach for 4 min and rinsed in water. Embryos were then fixed in a 1:1 suspension of heptane and 4%

formaldehyde (in PBS) for 15 min with vigorous shaking. The formaldehyde was removed and 1 volume of methanol added and the heptane:methanol suspension was vigorously shaken to devitellinize the embryos. After fixation, embryos were recovered and processed as described above for the nerve cord samples.

2.3.4 Larval body wall fillets

3rd instar larvae were pinned on a sylgard plate, filleted along the ventral midline, and pinned open. After removing the intestines, fat bodies, imaginal discs and ventral nerve cord, fillets were fixed in PBS with 4% PFA for 15 min (for anti-brp staining) or 30 min (for anti-GFP staining). For microtubule staining, we extracted the tissue with PEM (0.1M PIPES ph7, 1mM EDTA, 1mM MgCl2) containing 0.5% Triton-X-100 for 30s immediately before fixation. Samples were then fixed for 15 min in a solution containing 3.2% paraformaldehyde and 0.1% glutaraldehyde or 3.2% paraformaldehyde alone in PEM, followed by a post extraction with PEM for 30s. After fixation, samples were processed as above for staining.

2.3.5 Gelation, digestion and expansion of nerve cord and embryo samples

Samples were incubated in monomer solution (2 M NaCl, 8.625% Sodium Acrylate, 2.5% Acrylimide, 0.15% Bisacrylimide in PBS) for 1 h at 4° C prior to gelation. A stock of 4-hydroxy-2,2,6,6-tetramenthylpiperidin-1-oxyl (4-hydroxy-TEMPO) at 1% (wt/wt) in water was added to the incubation solution and diluted to concentration of 0.01%. Concentrated stocks of tetramethylethylenediamine (TEMED) and ammonium persulfate (APS) at 10% (wt/wt) in water were added sequentially to the incubation solution and diluted to concentrations of 0.2% (wt/wt). The tissues were then incubated at 37° C for 2-2.5 h. After the samples were gelled, the gels were cut and placed in a small 12-well

chamber and were digested in 8 units/ml proteinase K solution in digestion buffer (40 mM Tris pH 8, 1 mM EDTA, 0.5% Triton, 0.8 M Guanidine HCl) for 1 h at 37° C. Subsequently, samples were removed from the digestion solution and were allowed to expand in excess water overnight.

2.3.6 Gelation, digestion and expansion of Drosophila body wall samples

Samples were incubated in monomer solution for 1 h at 4° C prior to gelation. Larva fillets were gelled with the same solution as above, but were incubated at 37° C for 3-4 h. After gelation, the gels were cut and placed in a small 12-well chamber and 5mg/ml of Chitinase in PBS (pH6.0) was used to digest the cuticles for ~4 d at 37° C. Samples were then rinsed 2x with PBS for 5 min each and digested/expanded as above.

2.3.7 Gelation, digestion and expansion of Drosophila body wall samples with collagenase

Samples were gelled and treated with Chitinase as mentioned above. Samples were then incubated with 400units/ml collagenase solution (prepared with buffer 1x HBSS (w/o calcium, magnesium, and phenol red) with 0.01M $CaCl_2$ and 0.01M $MgCl_2$ added) overnight in 37° C shaking incubation chamber. After that, the samples were rinsed with PBS twice for ~5min and digested in 8 units/ml proteinase K solution in digestion buffer for 1 hour at 37° C incubation chamber.

2.3.8 Mounting and Imaging

Before expansion, samples were mounted on lysine coated 0.17 mm cover glass in wells made of PDMS. PBS was added to the well submerging the tissue to prevent it from drying out. After expansion, the expanded gel was trimmed to fit onto the coverglass, excess water was removed, and the gel was mounted on a lysine coated cover glass for

imaging. Confocal microscopy was performed on a Leica SP5 inverted confocal scanning microscope using a 63X 1.2 NA water lens or a 20X 0.75 NA air lens.

2.3.9 TEM

TEM was as previously described (Jiang et al., 2014). Briefly, larvae were perforated with insect pins, fixed in 2.5 % glutaraldehyde/0.1M sodium cacodylate buffer, washed in PBS and post-fixed in 2% osmium tetroxide. Samples were embedded in epon-araldite and 70nm sections were stained with lead citrate and viewed on a JEOL-1230 microscope with an AMT XR80 camera.

2.3.10 Measurements

Distortion analysis. Distortion analysis is conducted in the same way as mentioned in this paper(Chozinski et al., 2016)

Active zones. AZ numbers (Figure 3D) were scored as the number of discrete Brp positive structures in 2D projections of confocal stacks from corresponding areas of pre- and post-expansion tissue. AZ area was measured by computer-assisted tracing of the perimeter of Brp positive structures in 2D projections of confocal stacks, and density measurements represent the number of Brp positive structures per unit area (in 2D projections of confocal stacks). AZ area and dendsity measurements were taken from at least 5 independent samples. AZ architecture (singlets, doublets, multiples) represents the proportion of Brp positive structures with the respective number distinct ring-like structures.

Dendrite-epithelia interactions. Epithelial enclosure of somatosensory dendrites was measured in confocal image stacks as previously described (Han et al., 2012b). Briefly, image stacks were captured at a Z-depth of 0.15 microns, and where indicated, image

stacks were deconvolved using the Leica LAS deconvolution plugin set to adaptive PSF for 10 iterations. 3D reconstruction was performed with Imaris and co-localization was measured between fluorescent signals labeling dendrites (GFP immunoreactivity) and ECM (Perlecan immunoreactivity) using the Imaris Coloc module. The dendrites were traced in Imaris, portions of the arbor that failed to co-localize with the ECM (apically detached dendrites) were pseudocolored in traces, and the proportion of the arbor that was detached from the ECM was measured in these traces. Dendrites were identified in TEM images as processes near the basal epithelial surface containing arrays of parallel microtubules. 417 total dendrites were scored (in sections of X larvae) as ECM attached (in direct contact with the basement membrane) or detached (internalized in the epidermis), and the proportion of ECM attached dendrites is shown in Figure 3.4 F.

Chapter 3. The cell biology basis of dendrite epithelial ensheathment

3.1 INTRODUCTION

Somatosensory neurons innervate our skin and interact with the epidermis to help us sense the world. However, the cellular interactions between epidermis and neurons, and possible mechanisms by which the skin controls neuron growth and function are largely unexplored. This gap in our knowledge limits our ability to treat somatosensory neuron disease, which has a major impact on the quality of human lives. Twenty million Americans suffer from peripheral neuropathy, in which a large percentage have no identified etiology and few - if any - treatments.

Neuron-substrate interactions are important for neuronal development and function. 100 years ago, Ramon y Cajal suggested that skin may attract sensory axons to grow to it, based on the observation that collaterals branch off sensory nerve trunks as the nerves approach the skin. His hypothesis has been supported by many studies across species. In mouse and zebrafish, diffusible factors are found to attract somatosensory axons to target epidermis (Lumsden and Davies, 1983; Wang et al., 2012). In *C.elegans* and *Drosophila*, some of the somatosensory dendrites directly interact with epidermis and muscles. Signals derived from both epidermis and muscle help shape these neuron arborizations (Dong et al., 2013; Salxberg et al., 2013; Liang et al., 2015; Yasunaga et al., 2010; Han et al., 2012; Jiang et al., 2014; Kim et al., 2012; Parrish et al., 2009a).

In addition to directing neurons to their target fields, the epidermis can also facilitate neuron structure by regulating the degradation of neuron processes during developmental pruning or after injury. During development, the degradation of neuron

processes plays an important role in neuron remodeling (Williams and Truman, 2005); in adults, regeneration of neuron processes after physical injury or pathological conditions leads to neuronal remodeling. (Luo and O'Leary, 2005). In the peripheral nervous system, many types of cells contribute to clearing neuronal debris during degradation, in addition to the professional phagocytes such as macrophages. In mammals, axon debris during degradation is cleared by glia in the CNS and Schwann cells in the PNS together with macrophages (Hall, 2005). In *Drosophila*, macrophage like hemocytes have been reported to engulf dendrite debris during pruning (Williams and Truman, 2005). However, it is the epithelial cells, instead of hemocytes, that work as primary phagocytes to facilitate dendrite degradation after injury and during pruning, shown by Han et al in 2014 (Han et al., 2014). Similar phenomena were observed in zebra fish afterwards, where epithelial cells clear injury-induced axon debris through engulfment machinery (Rasmussen et al., 2015). Together, epithelial cells exert multiple functions when regulating somatosensory neuron morphology.

On the other hand, signals derived from neurons also influence their substrates. Interactions between axons and Schwann cells in the vertebrate PNS are one of the most striking examples of reciprocal cell-cell interactions in cell biology. During development, axons promote the generation of Schwann cells via trophic, mitogenic and differentiative effects on precursor cells (Jessen and Mirsky, 2005; Sherman and Brophy, 2005). In the PNS, Schwann cells adopt one of two distinct relationships with axons, either myelinating individual axons or ensheathing multiple, small axons in what are called Remak bundles. It has long been known that the axon determines which of these two distinct phenotypes Schwann cells adopt, based on experiments in which nerve of

different composition were cross-anastomosed (Langley and Anderson, 1904). Some evidence shows that the amount of the growth factor that different axons express is the key determinant of the ensheathment fate of axons (Nave and Salzer, 2006). However, the axonal signals that regulate the myelin sheath is still not fully understood.

In addition, signals from somatosensory neurons also regulate epidermis. Neuropeptides released from sensory nerves play defined roles in cutaneous physiology and in certain skin diseases (Roosterman et al., 2006). For instance, neuropeptides derived from sensory nerves can enhance local keratinocyte proliferation that is involved in atopic eczema, a chronic skin disease characterized by epidermal hyperplasia (Roggenkamp et al., 2013). Together, the cross-talk between somatosensory neurons and their substrates is important to the development and homeostasis of both sides.

In *Drosophila*, there are four classes of dendritic arborization sensory neurons, distinguished by their different morphologies. Among these the class III and class IV neurons are mechanosensory neurons, which provide complete and independent tiling of the body wall. Class III neurons respond to gentle touch via the NOMPC ion channel (Yan et al., 2013b); Class IV neurons are nociceptors, which respond to noxious stimuli, such as harsh mechanoforce and heat (Guo et al., 2014; Hwang et al., 2007; Kim and Johnson, 2014; Xiang et al., 2010). These neuron dendrites innervate the larval body wall and are mostly confined to a 2 dimensional sheet sandwiched between a monolayer of body wall epithelial cells and extracellular matrix (ECM). Interestingly, these dendrites sometimes can detach from ECM and become ensheathed by epidermal cells (Han et al., 2012; Jiang et al., 2014; Kim et al., 2012a). Transmission electron microscopic (TEM) images show that these ensheathed dendrites are located in the folds of the invaginated

epithelial cell basal membrane, in the same way that Schwann cells ensheath peripheral nerves. Even though this ensheathment structure is also identified in many other species (Cauna, 1973; Goodman, 2006; Han et al., 2012; Jiang et al., 2014; Kim et al., 2012; O'Brien et al., 2012), its formation, cell biology structure and function has not been studied at all, due to its tiny size (only a few hundred nanometers) and a lack of tools or markers for visualization.

Here we use *Drosophila* class IV sensory neurons as a model system to identify the cell biology basis and function of the dendrite epidermis interactions, with a particular focus on the cellular events in the epidermis that facilitate dendrite ensheathment. Using the Gal4-UAS binary expression system, we have conducted an exhaustive survey of markers of different subcellular domains. Our findings indicate that, during later stages of larval development, regions of epithelial membranes that are in contact with somatosensory neurons have actin-rich specialized subdomains. Dendrites are required for the formation these membrane subdomains. However, they are not necessary to maintain these membrane subdomains. Finally, we found epithelial dendrite ensheathment may regulate dendrite degradation after injury and facilitates Class IV da neuron nociception.

3.2 RESULTS

3.2.1 Identification of ensheathment markers on epithelial cells

Dendritic ensheathment is coupled with epithelial cell membrane deformation which may change the local epithelial membrane molecular composition. To determine if there are specialized subdomains on epithelial cells that are associated with dendrite ensheathment, we sought markers of ensheathed dendrite branches. Previous work done by screening a

collection of GFP trap lines for expression associated with da neurons showed that the septate junction protein coracle is enriched where dendrites become ensheathed (Kim et al., 2012a). Here we used the GAL4-UAS expression system to examine the epithelial expression pattern of 65 GFP tagged candidate molecules. We picked candidate molecules that are involved in pathways regulating cell membrane tubulation, dynamics and endocytosis. Such molecules include membrane markers, phosphoinositides, junction proteins, actin binding proteins, endocytic proteins, membrane tubulation markers, lipid binding proteins and microtubule binding proteins. Interestingly, 9 of 65 candidates showed varying levels of intermittent enrichment along class IV dendritic arbors. These 9 candidate molecules include the PH-domain of phospholipase C, which binds to membrane phosphatidylinositol 4, 5-bisphosphate (PIP2) (Figure 3.1 A-D); the cell membrane marker myristoylated GFP (myr-GFP) which binds to membrane lipids (Figure 3.1 E-F); the endocytic molecule, ADP ribosylation factor at 51F (Arf51F) (Figure 3.1 G, H); adherent junction components E-cadherin shotgun (shg) (Figure 3.1 I, J); β catenin armadillo (arm) (Figure 3.1 K, L); and gap junction protein Innexin 3 (Inx3) (Figure 3.1 M, N). We also observed F-actin marker GMA (Figure 3.1 O, P) and actin binding GTPase Rho (Figure 3.1 Q, R). By contrast, the rest of the 65 candidate molecules did not show any expression pattern associated with dendrite branches, for example cell membrane marker CD8-GFP (Figure 3.1 S, T). Therefore, there are specialized membrane subdomains on epithelial cells associated with the Class IV dendritic arbor. The enrichment we saw was likely caused by local accumulation of the molecules in the vicinity of somatosensory dendrites. Interestingly, we also observed that these molecules tend to accumulate along primary and secondary dendrite branches but

not along the smaller tertiary and terminal branches (Supplemental Figure 3.1), which indicates that epithelial cells may somehow selectively ensheath thicker branches and different regions of the dendrites may send different signals to the epithelial cells.

Next, we wanted to test whether those enrichments were associated with dendritic ensheathment. Firstly, we used the septate junction protein Coracle as a benchmark for dendrite ensheathment and measured co-localization of each marker with Coracle at sites of ensheathment. Our preliminary data (data not shown due to incomplete data set) showed the markers we identified all co-localized with the enriched Coracle, suggesting they are bona fide ensheathment markers. Interestingly, some marker molecules, such as GMA, Rho and Inx3, were enriched at a subset of ensheatment sites, due to various possibilities. One possible explanation for these observations is that the ensheathment structures themselves could have different compositions depending on the status and developmental stages of the ensheathment. Second, some molecules' accumulation could be very dynamic and transient, for example the small GTPase Rho, which regulates actin rearrangement (Spiering and Hodgson, 2011). Finally, since many of these molecules such as the GMA labeled F-actin also have a strong expression ubiquitously in the epithelial cytosol, enrichment may sometimes be hard to identify with a strong expression background.

In contrast, PIP2 enriched at all the ensheathed dendrites. PIP2 is formed primarily by the type I phosphatidylinositol 4-phosphate 5-kinases (PIP5Ks) from PI4P. PIP2 is a minor phospholipid component of cell membranes (It constitutes about 1% of the plasma membrane), however, it is responsible for a wide range of membrane-related phenomena, including cytoskeletal attachment, organization, regulation, and

polymerization of F-actin via direct binding to actin regulating proteins (Janmey and Lindberg, 2004; Sechi and Wehland, 2000; Shibasaki et al., 1997). In our case, accumulated PIP2 is likely functioning to recruit actin binding proteins that induce GMA labeled F-actin enrichment. The enrichment of Rho, which is best known for regulating actin polymerization, also indicates rearrangement of F-actin at the epithelial membrane specialized subdomain where dendrites are ensheathed.

Arf51F, the *Drosophila* Arf6 orthologue, is also found enriched at all dendritic ensheathments. Arf6 is a GTP-binding protein. In mammalian cells, activated Arf6 is primarily involved in membrane trafficking and remodeling (Altschuler et al., 1999; Moss and Vaughan, 1998). It is also involved in mechanisms such as actin cytoskeletal remodeling (Guo et al., 2014; Johnson et al., 2011; Kondo et al., 2000) and activation of PIP5Ks (Brown et al., 2001; Honda et al., 1999). Interestingly, we observed extensive associations of vesicular transport with sites of ensheathment using Serial block-face scanning electron microscopy (data not shown), suggesting that endocytosis may be important to the ensheathment structure formation. In our case, Arf51F may enrich at the ensheathed domain to facilitate cell membrane reorganization via regulation of endocytosis. It may also contribute to the local enrichment of PIP2 by activating PIP5Ks.

Interestingly, several junction proteins were also found to enrich along the dendritic arbor. The enrichment of these junction proteins may form direct interactions between epithelial cells and the ensheathed dendrite. It may also localize only at epithelial cell membranes and form autotypic junctions between invaginated membranes within one epithelial cell. In mammalian PNS, gap junction proteins and adherent junction proteins play important roles in the Schwann cell myelin sheath. In mammalian

PNS, gap junction protein connexin32 (Cx32) localizes in the uncompacted myelin domains, paranodal loops and Schmidt-Lantermann incisures of Schwann cells, suggesting that Cx32 may form autotypic gap junctions between myelin membranes (Anzini et al., 1997; Balice-Gordon et al., 1998; Suter and Scherer, 2003). By forming a radial pathway through the layers of the myelin sheath, these channels could reduce up to 1000-fold the distance that ions and messenger molecules travel between the perinuclear and the periaxonal regions of Schwann cells. Apart from gap junctions, adherent junction protein E-Cadherin and tight junction protein Claudins also localize at the paranodal and incisures region of the myelin sheath, to stabilize the wraps (Poliak et al., 2002; Tricaud et al., 2005).

3.2.2 Localization of the ensheathment molecules on the ensheathment structure

In order to characterize the molecular and cellular structure of the ensheathment complex, we employed expansion microscopy (ExM), a super resolution microscopy technique, to visualize the position of the ensheathment markers on the ensheathment structure. As is shown in Figure 3.2 A, B, A' and B', PIP2 accumulated along the entire length of the membrane invagination that serves as the site of ensheathment. However, the gap junction protein Inx3 only localized at the basal side of the ensheathed dendrite (Figure 3.2 C, D, C', D'), suggesting the gap junction proteins may form autotypic gap junctions between epithelial cell membranes, basal to ensheathed dendrites, similar to the Cx32 on the myelin sheath. In this scenario, the gap junctions formed by Inx3 and other innexins could likely facilitate faster travel of ions and messenger molecules in the epithelial cell. The same ExM assay needs to be done on other ensheathment markers, especially other junction proteins.

3.2.3 Dendrites are required for the formation but not the maintenance of epithelial membrane specialized domains

Our previous study shows dendritic ensheathment starts to occur around 72 hours after egg laying (AEL) (Jiang et al., 2014). In order to determine how the ensheathment is initiated, we set out to determine whether dendritic ensheathment or the epithelial cell membrane specialized domains that mark sites of ensheatment appeared first? To answer this question, we looked at the expression pattern of PIP2 at different developmental time points. As shown in Figure 3.3,, enrichment of the ensheathment markers began expression at 72 hours AEL, correlating with the increased dendritic ensheathment. This means there is no pre-pattern of the specialized domains on epithelial membranes before the dendritic ensheathment happens, suggesting the interaction of dendrites with epithelial cells induce the formation of the epithelial membrane specialized structure.

Is dendritic ensheathment necessary to the formation of the epithelial specialized domains? To address this question, we genetically ablated Class IV da neurons by specifically expressing the cell death protein, *reaper* (*rpr*) (Chen et al., 1998), to Class IV neurons. Then we immunostained the 3rd instar larvae with antibodies to Coracle and HRP, which labels all classes of the sensory neurons (Jan and Jan, 1982). With Class IV da neurons being killed during the embryonic stage, the Coracle enrichment outside of junctional domains (corresponding to sites of dendrite ensheathment)is largely decreased (Figure 3.3 G-J, L). In larvae lacking Class IV neurons, the small amount of remaining Coracle enrichment co-localized with other classes of neurons (Figure 3.3 I, J), which are ensheathed less extensively than Class IV neurons (see below). Taken together with our time lapse imaging, these results suggest that signals from somatosensory dendrites are required to initiate formation of the epithelial domains that ensheath dendrites.

Since dendrites are required for formation of the ensheathment structures in epithelial cells, we next examined whether dendrites are necessary to maintain the epithelial specialized domains? To answer this question we specifically expressed GPF-PLC-PH in epithelial cells to label PIP2 as an ensheathment marker and labeled Class IV da neurons with CD4-tdTOM. We then severed proximal dendrites of class IV da neurons near the soma using a pulsed nitrogen laser on larvae at 72 hours AEL, which induced degeneration of all dendrites distal to the injury site. Twenty four hours after injury (AI), the severed branch was completely degenerated (Supplemental Figure 3.2 A-D), and no dendrite regrowth had started. However, the epithelial cell membrane PIP2 enrichment was still present (Supplemental Figure 3.2 B', D'). This suggests that, unlike Schwann cell-ensheathed axons, dendrites are not required to maintain the epithelial membrane specialized domain after formation. This may be due to the potential stabilization role played by the junction proteins that localized on the ensheathment membrane. In addition, the remaining epithelial membrane specialized structure may help to reshape the new dendrite arbor during dendritic regrowth.

Based on our observation that gap junction protein (and possibly other junction proteins) localize between the invaginated epithelial cell membrane to facilitate information exchange within the epithelial cells and stabilize the ensheathment structure, we hypothesize that the junction proteins may be the last markers to occur on the ensheathment epithelial membrane during ensheathment maturation. F-actin and Rho enrichment may happen after PIP2 enrichment, based on the fact that PIP2 can recruit actin binding molecules. The multifunction GTPase Arf51F enrichment suggests that endocytosis may play a role during membrane reorganization. Unfortunately, we don't

have evidence to clarify what happens during the maturation of the ensheathment structure. Therefore, to have a better understanding of the formation of the ensheathment and the epithelial specialized subdomain, detailed time lapse imaging is needed to reveal the sequence of occurrence of these marker molecules on the ensheathment structure during development.

3.2.4 The specialized domains of epithelial membranes facilitate dendritic ensheathment

Next, we asked whether the epithelial membrane ensheathment molecules also influence dendritic ensheathment formation. To answer this question, we modified epithelial PIP2 levels by interrupting the epithelial PIP2 metabolism. The major route of synthesis of PIP2 is by phosphorylation of phosphatidylinositol (PI) by PI 4-kinases (PI4K), making phosphatidylinositol 4-phosphate (PI4P), which is then phosphorylated at the 5-position by PI4P 5-kinase (PIP5K). We knocked down PI4K in body wall epithelial cells and stained the larvae with coracle to label dendritic ensheathment. Our preliminary data (not shown) showed a decrease in the ensheathment level after interrupting epithelial PIP2 synthesis. In addition, we also reduced dendritic ensheathment by feeding 2nd instar larvae with 20μM PBP10 for 24 hours. PBP10 is a cell-permeable PIP2 binding peptide that can sequestrate PIP2 and interrupt many PIP2 mediated cellular events (Wong et al., 2005). As expected, we saw a decrease in the amount of coracle enrichment in animals exposed to PBP10 in our preliminary results. Therefore, the enriched PIP2 is not only an epithelial membrane marker for dendritic ensheathment, it also facilitates ensheathment formation.

Next, we asked what regulates PIP2 enrichment in epithelial cells. Endocytic signaling has been known to mediate membrane turnover and reorganization during many

cellular events such as cell division and migration (Berdnik et al., 2002; Schiefermeier et al., 2011). From our screening, we found the accumulation of endocytic protein Arf51F at the epithelial dendritic ensheathment structure. To study whether endocytic signaling regulates epithelial PIP2 enrichment and dendritic ensheathment, we blocked the endocytic pathway in epithelial cells by expressing the dominant negative mutant (DN) of *shibire (shi)*, the *Drosophila* dynamin, in body wall epithelial cells. Blocking endocytosis in epithelial cells largely changed the expression pattern of PIP2 on epithelial cell membrane (Figure 3.4 A-F). No enrichment of PIP2 was found at either cell-cell junctions or along the dendritic arbor (compare Figures 4 C, F). Meanwhile, Class IV da neuron dendrite morphology was also significantly changed. In *shi DN* animals Class IV da neuron dendrites had a severe overgrowth defect compared with the control (Figure 3.4 B, E). This overgrowth dendrite phenotype may be due to the lack of dendritic ensheathment that tethers dendrites to the epidermis. (Jiang et al., 2014) Together, these observations suggests the epithelial endocytic pathway may affect dendritic ensheathment via regulating the formation of epithelial specialized ensheathment structure. To further confirm this, we plan to test the expression pattern of other epithelial ensheathment markers after blocking epithelial endocytosis.

3.2.5 Dendritic ensheathment may influence dendrite degradation after injury

Dendrite degeneration happens during neuron remodeling, such as dendritic pruning; similar remodeling may occur after neuronal injury. Dendrite debris resulting from this degeneration needs to be immediately removed to maintain tissue homeostasis and to prevent an inflammatory response. Degenerating neuronal processes are usually cleared via engulfment by phagocytes. In the central nervous system(CNS), phagocytosis of

degenerating axons and dendrites is mainly carried out by glia (Aldskogius and Kozlova, 1998; Awasaki and Ito, 2004; MacDonald et al., 2006; Marín-Teva et al., 2004; Watts et al., 2004). In the peripheral nervous system (PNS), injured axons are cleared by both Schwann cells and macrophages (Coleman et al., 1998). Phagocytosis is a form of endocytosis, which requires many membrane reorganizations. Many of the ensheathment molecules we identified are also part of the phagocytosis pathway (Egami et al., 2015; Scott et al., 2005).

To determine whether dendritic ensheathment is involved in dendrite degeneration, we expressed GPF-PLC-PH in epithelial cells to label PIP2 as a ensheathment marker and CD4-tdTOM in class IV da neurons to label dendrites during fragmentation. We then severed proximal dendrites of class IV da neurons near the soma using nitrogen laser on larvae at 96 hour AEL (Arrowhead in Figure 3.5 A, D), which induced degeneration of all dendrites distal to the injury site. At 3 hours after injury (AI) (Figure 3.5 A, B), the severed branch showed no sign of fragmentation and the epithelial PIP2 showed intermittent enrichment along the dendritic branch, suggesting some parts of the severed branch were ensheathed (Figure 3.5 C, C', C"). However, at 6 hours AI, the severed branch was undergoing degeneration, showing beaded dendrites and fragmentation (Figure 3.5 D, E). Most interestingly, the epithelial PIP2 at 6 hours AI accumulated along almost all of the whole severed branch (Figure 3.5 F, F', F"). As marked by by the arrows in Figure 3.5, the un-ensheathed fractions of dendrites at 3 hours AI were now ensheathed during dendrite degeneration at 6 hours AI (Figure 3.5 C", F"). In contrast, the PIP2 enrichment pattern was the same at 3 hours AI and 6 hours AI along the dendrite branch that was not severed (Figure 3.5 C', F', G). This suggests

dendritic ensheathment may play an important role in regulating dendrite regeneration after injury.

3.2.6 Dendritic ensheathment is important to the mechanosensitivity and thermosensitivity of Class IV da neurons

In the mammalian CNS, Schwann cells ensheath peripheral axons and form electrically insulating layers to restrict the axon membrane depolarization to the nodes of Ranvier, resulting in rapid nerve conduction. A large majority of peripheral neuropathies are caused by demyelination (Hughes, 2002; Suter and Scherer, 2003). We asked whether the dendritic ensheathment in *Drosophila* also plays an important functional role.

In *Drosophila* PNS, there are four classes of somatosensory neurons distinguished by their morphology. Among them, Class III and Class II neurons respond to gentle touch (Yan et al., 2013b; Tsubouchi et al., 2012); Class IV neurons are nociceptors (Guo et al., 2014; Hwang et al., 2007; Kim and Johnson, 2014; Xiang et al., 2010). Class I neurons function as proprioceptors required for coordinated larval locomotion (Hughes and Thomas, 2007).

All classes of *Drosophila* larval somatosensory neurons grow underneath epithelial cells, however, it is unknown whether other classes of sensory neurons interact with epithelial cells in the same way that the Class IV da neurons do. A better characterization of the dendritic ensheathment of other classes of sensory neurons will shed light on the formation of the dendritic ensheathment structure and function. Firstly, we asked whether different classes of *Drosophila* sensory neurons have varying extents of dendritic ensheathment. To test the percentage of ensheathment in other classes of somatosensory neurons, we did coracle staining in larvae with GFP labeled Class III da neurons or Class I da neurons. As is shown in Figure 3.6, less than 5% of the dendrites

were ensheathed in Class III or Class I da neurons (The ensheathment level of Class II da neurons remains to be tested). By contrast, in Class IV da neurons approximately 20% of the dendrites are ensheathed. This suggests that dendritic ensheathment preferentially happens in Class IV da neurons and may associate with Class IV da neuron nociception.

In order to test whether dendritic ensheathment is associated with Class IV da neuron nociception, we conducted escape behavior assays on Drosophila larvae with different dendritic ensheathment levels. Firstly, we tested the association between dendritic ensheathment level with mechanonociception. Stimulation with 80mN von frey filaments were applied to wild type larvae and mutants with reduced dendritic ensheathment. Both the *ban* mutant and neuronal integrin overexpression larvae have previously been shown to have dampened dendritic ensheathment. (Han et al., 2012; Jiang et al., 2014) Epithelial PI4P knockdown and PBP10 treated animals were found to have decreased dendritic ensheathment in our current study. Compared to the 60% response rate of the wild type larvae, mutants with less dendritic ensheathment had significant response deficits (Figure 3.7 A). Similar results were observed with thermal nociception assays (Figure 3.7 B). Together, we conclude that dendritic ensheathment is required for Class IV da neurons to maintain their sensitivity to noxious stimuli. Dendritic ensheathment may be a major contributor to facilitate nociception versus gentle touch sensation, based on the fact that dendritic ensheathment mostly occurs in Class IV da neurons.

3.3DISCUSSION

3.3.1 The formation of dendritic ensheathment

Somatosensory neuron ensheathment by skin epithelial cells has been found in many different species (Cauna, 1973; Goodman, 2006; Han et al., 2012; Jiang et al., 2014; Kim et al., 2012a; O'Brien et al., 2012). They all share the same structure where parts of the somatosensory neuron processes grow within epithelial cells and wrapped by the folded epithelial cell membrane. Unfortunately, nothing more is known beyond this so far.

Structurally, this epithelial ensheathment shares some similarities to the axon ensheathment by Schwann cells in the mammalian PNS. Although many studies have been done on the myelin sheath formation and regulation, the interactions between axons and Schwann cells, especially the Schwann cell axon recognition, are still unclear. In zebrafish, CNS myelin membrane wraps CNS axons by PI(3,4,5)P3 dependent polarized growth at the inner tongue of the wrapping oligodendrocytes (Snaidero et al., 2014). In our model, we identified specialized membrane subdomains on epithelial cells associated with dendritic ensheathment. This ensheathment complex is actin rich and also enriched with PIP2, endocytic molecules and junction proteins, including the gap junction protein *inx3*. In the mammalian PNS, gap junction proteins and adherent junction proteins play important roles in regulating the Schwann cell myelin sheath. In humans, mutations affecting the gap junction gene Cx32 are associated with the X-linked form of the hereditary peripheral neuropathy Charcot-Maire-Tooth disease (CMTX) (Bergoffen et al., 1993). Mice that have connexin32 knocked out develop demyelinating peripheral neuropathy (Scherer et al., 1998). In our model, *inx3* enrichment is localized at the folded epithelial cell membrane of the ensheathment structure to form autotypic gap junctions, similar to the gap junctions on the myelin sheath. However, the role of *inx3* and other junction proteins on the dendritic ensheathment formation or neuronal function is unclear.

We believe this specialized membrane structure helps to facilitate, stabilize and maintain the ensheathment of the dendrite. However, dendritic ensheathment is not itself induced by epithelial membrane specialized domains. Our results show the formation of these membrane specialized domains is dependent on dendritic ensheathment, which indicates the formation of epithelial membrane ensheathment subdomain is triggered by some dendrite derived signals. Interestingly, we also found dendritic ensheathment preferentially happens in Class IV da neurons instead of the other classes of somatosensory neurons in *Drosophila* larva. This narrows the dendrite-derived ensheathment signals to Class IV da neuron specific molecules or features. Adhesion molecules and some ligand dependent pathways are most likely involved in regulating epithelial ensheathment domain formation. In the mammalian PNS, Neuregulin 1 (Nrg 1) type III on axons is required for axonal recognition via ErbB2/3 receptor on Schwann cells (Nave and Salzer, 2006; Newbern and Birchmeier, 2010). Adhesion molecules such as the myelin-associated glycoprotein (MAG) expressed by Schwann cells (Trapp et al., 1989) are also involved in Schwann cell-axon contact. In addition, the size of the axons also plays a determinant role during myelination. Larger axons are sorted by Schwann cells to myelinate, while small axons are embedded instead of wrapped in Schwann cells in bundles to form the Remak bundle (Laura et al., 2016). Interestingly, we observed a similar size preference phenomenon in our model as well. Ensheathment tends to happen along primary dendrites, instead of the thinner terminal branches. This may also explain the neuronal type preference of ensheathment that we saw, since Class III and Class I neurons may have thinner dendritic branches compared with the Class IV da neurons.

However, the mechanism underlying this ensheathment sorting phenomena remains to be studied.

3.3.2 The function of dendritic ensheathment

Previously, we found the extent of dendritic ensheathment is associated with the fidelity of dendritic arbors to their receptive fields (Jiang et al., 2014). Mutants that have dendritic ensheathment disrupted tend to have uncontrolled dendrite overgrowth (Jiang et al., 2014). Apart from regulating dendritic morphology and holding dendrites to their target substrates, whether dendritic ensheathment also influences neuron functions is even more interesting to know. Based on our research, we found that dendritic ensheathment primarily happens in Class IV da neurons and is important to mechano and thermal nociception. The functional regulation of dendritic ensheathment may due to a couple of possibilities. First, epithelial cells may act as sensory receptors. And direct interactions between the ensheathed dendrites and epithelial cells may work as synapses. In addition, dendritic ensheathment may regulate ion channel distributions on dendrites. Ion channels such as PPK, Piezo, TRPA1 have been demonstrated to contribute to the mechanonociception or thermal nociception in *Drosophila* larva (Guo et al., 2014; Kim et al., 2012b; Neely et al., 2011). However, the distribution of these ion channels on the dendritic arbor has not been studied. In the mammalian PNS, different ion channels are located at different sub regions along the myelinated axon (Lai and Jan, 2006). Loss of myelin sheath can alter ion channel distribution and lead to pheripheral neuropathy (Devaux and Scherer, 2005; Hamada and Kole, 2015). We hypothesis body wall epithelial cells in *Drosophila* may also influnce the dendritic ion channel localization.

Finally, dendritic ensheathment may increase the action potential conduction velocity along the dendrites in a myelin-sheath-like fashion. To address this question, recording electrodes can be used to measure the nerve conduction latency along the Class IV da neurons of larvae with different extents of dendritic ensheathment. It will also be very interesting to know whether the action potential conduciton velocity varies between different classes of somatosensory neurons in the *Drosophila* larva.

3.4MATERIALS AND METHODS

3.4.1 Fly stocks

Flies were maintained on standard cornmeal-molasses-agar media and reared at 25° C under 12 h alternating light-dark cycles. The following fly lines were used in this study: *w1118* (BL6326); *A58-Gal4* (Galko and Krasnow, 2004); *ppk-mCD8-GFP* (Parrish et al., 2009b); *ppk-CD4-tdTom* (Han et al., 2011); *UAS-CD4-tdGFP* (BL35835); *UAS-mCD8-GFP* (BL60704); *UAS-myr-GFP* (BL32197); *UAS-Akt-PH-GFP* (Reversi et al., 2014); *UAS-PLC-PH-GFP* (BL398693*); UAS-Inx3-GFP* (Giuliani et al., 2013); *UAS-arm-GFP* (BL58724); *UAS-shg-GFP* (BL58445); *NrxIV-GFP* (CA06597); *UAS-Dlg-GFP* (BL30928); *UAS-GMA* (BL31774); *UAS-Arp3-GFP* (BL39721); *UAS-capu-GFP* (BL24763); *UAS-dpod-GFP*; *UAS-Myo10A-GFP* (BL24780); *UAS-Pak-GFP* (BL53266); *UAS-Rho-GFP* (BL9393); *UAS-sstn-GFP* (BL65863); *UAS-Apc2-GFP* (BL8815); *UAS-hook-GFP* (BL65858); *UAS-dia-GFP* (BL56751); *UAS-EndoA-GFP* ; *UAS-EndoB-GFP*; *UAS-Cip4-GFP* (Yan et al., 2013a); *UAS-Arf102F-GFP* (BL65866); *UAS-Arf51F-GFP* (BL65867); *UAS-Arf79F-GFP* (BL65850); *UAS-Fy-GFP* (BL66513); *UAS-par-6-GFP* (BL65847); *UAS-Sema2a-GFP* (BL65747); *UAS-step-GFP* (BL65862); *UAS-bas-GFP*; *UAS-Rab35-YFP* (BL9819); *UAS-Rab4-YFP* (BL50787); *UAS-Rab21-YFP* (BL9801);

UAS-gammacop-GFP (BL29711); *NompC-gal4* (BL36369); *Gal4*^{221} (Grueber et al., 2003); UAS-fwd-RNAi (BL35257); UAS-shi.K44A (BL5811).

3.4.2 Live Imaging

Embryos were collected on yeasted grape juice agar plates and aged at 25˚C in a moist chamber. At the appropriate time, a single embryo/larva was mounted in 90% glycerol under coverslips sealed with grease and imaged using a Leica SP5 microscope with a 40x 1.25NA lens. For quantitation of dendrite phenotypes, image stacks of dendrites in segments A2-A4 were captured from 8-10 larvae. For high-resolution confocal imaging of the dendrite-ECM interface, larvae were anesthetized with ether prior to mounting and image stacks with a 0.2um Z step size were acquired.

3.4.3 Expansion Microscopy

Expansion microscopy was conducted following the same steps as mentioned in Chapter two for Drosophila body wall sample expansion.

3.4.4 Laser Ablation

A single larva was mounted, as for live imaging, and the proximal branch of Class IV da neuron dendrites was targeted near the soma under a 100x 1.4NA objective using a 337nm pulsed nitrogen laser (Andor Micropoint; 12 Hz, 15 sec) mounted on a Leica DM550 microscope. Following ablation, animals were recovered to cornmeal agar and imaged 3 hours, 6 hours and 24 hours later.

3.4.5 Immunohistochemistry

Larval fillets were dissected/processed as described (Grueber et al., 2002) and stained with the following antibodies: HRP conjugated with Cy2 (1:200; Jackson labs), C566.9

(1:50; Hybridoma Bank), GFP (1:100; Invitrogen), Dsred (1:50, Clontech), and secondary antibodies from Invitrogen.

3.4.6 Behavior assay

Flies were maintained on standard cornmeal-molasses-agar media and reared at 25° C under 12 h alternating light-dark cycles. 96hr AEL larvae of different genotypes were used for the von frey assay with 80 mN von frey filaments. The von frey assay were conducted as described (Zhong et al., 2010). For the heat probe assay, 40° C heat probe was applied to 96hr AEL larvae of different genotypes as described (Tracey et al., 2003). The rolling of the larvae was recorded.

3.4.7 Measurements

Dendrites were traced and measured using Neurolucida. Other measurements were conducted using ImageJ.

3.4.8 Statistical Analysis

Differences between group means were analyzed via ANOVA with a post hoc Tukey's test. Difference between group means of wild type control and other genotype groups were analyzed via ANOVA with the Dunnett's multiple comparisons test. Differences between means of two groups were analyzed via Student's t-test.

CONCLUSION AND FUTURE WORK

To sum up, the interaction between somatosensory neurons and the epidermis is not only critical to neuronal morphology but also important for neuronal function. In the first chapter of my research, we found the epithelial derived signals are involved in coordinating the growth of somatosensory neurons and epidermis during development. In the *Drosophila* larva, epithelial microRNA *bantam* inhibits the growth Class IV da neurons by regulating epithelial endocycle, which, as a result, regulates dendrite growth by changing epithelial adhesive properties. We also found the coordinated growth between neurons and epithelial cells are associated with the extent of the dendritic ensheathment, where dendrites are partially embedded in epithelial cells. In the last chapter of my research, we identified specialized subdomains on the epithelial cell membrane that are associated with the ensheathed dendrites. The epithelial ensheathment structure, which shares many components with the cell junctions, can facilitate and maintain the ensheathment of the dendrites. However, the formation of the dendritic ensheathment is regulated by signals from both neurons and epithelial cells. Finally, by using behavior assays, we found dendritic ensheathment can facilitate Class IV sensory neuron nociception.

My thesis work for the first time characterized the structure and formation of the ensheathment of neuronal processes in epithelial cells, which occurs in many different species. It is also the first time to reveal the functional role of this special type of neuron-epithelial interaction. In the future, more detailed characterizations are needed to fully understand the mechanism of the functional regulation of dendritic ensheathment. It will be very interesting to know whether the underlying mechanism of Drosophila functional regulation of the dendritic ensheathment is similar to what happens in the sensory nerves in human skin. In addition, the molecules that are involved in neuron epithelial direct

contact are still not clear. So far, all the epithelial ensheathment components we identified are not involved in the direct interaction between the ensheathed dendrites and the epithelial membrane. A better understanding of the direct interaction molecules may shed light on the key regulators of the ensheathment process, which may provide us new targets for peripheral neuropathy treatments.

BIBLIOGRAPHY

Aldskogius, H., and Kozlova, E.N. (1998). Central neuron-glial and glial-glial interactions following axon injury. Prog. Neurobiol. 55, 1–26.

Altschuler, Y., Liu, S., Katz, L., Tang, K., Hardy, S., Brodsky, F., Apodaca, G., and Mostov, K. (1999). ADP-ribosylation factor 6 and endocytosis at the apical surface of Madin-Darby canine kidney cells. J. Cell Biol. 147, 7–12.

Anzini, P., Neuberg, D.H.-H., Schachner, M., Nelles, E., Willecke, K., Zielasek, J., Toyka, K.V., Suter, U., and Martini, R. (1997). Structural Abnormalities and Deficient Maintenance of Peripheral Nerve Myelin in Mice Lacking the Gap Junction Protein Connexin 32. J. Neurosci. 17, 4545–4551.

Awasaki, T., and Ito, K. (2004). Engulfing action of glial cells is required for programmed axon pruning during Drosophila metamorphosis. Curr. Biol. CB 14, 668–677.

Balice-Gordon, R.J., Bone, L.J., and Scherer, S.S. (1998). Functional Gap Junctions in the Schwann Cell Myelin Sheath. J. Cell Biol. 142, 1095–1104.

Becker, J.W., Erickson, H.P., Hoffman, S., Cunningham, B.A., and Edelman, G.M. (1989). Topology of cell adhesion molecules. Proc. Natl. Acad. Sci. U. S. A. 86, 1088–1092.

Berdnik, D., Török, T., González-Gaitán, M., and Knoblich, J.A. (2002). The Endocytic Protein α-Adaptin Is Required for Numb-Mediated Asymmetric Cell Division in Drosophila. Dev. Cell 3, 221–231.

Bergoffen, J., Scherer, S.S., Wang, S., Scott, M.O., Bone, L.J., Paul, D.L., Chen, K., Lensch, M.W., Chance, P.F., and Fischbeck, K.H. (1993). Connexin mutations in X-linked Charcot-Marie-Tooth disease. Science 262, 2039–2042.

Bloomfield, S.A., and Hitchcock, P.F. (1991). Dendritic arbors of large-field ganglion cells show scaled growth during expansion of the goldfish retina: a study of morphometric and electrotonic properties. J. Neurosci. Off. J. Soc. Neurosci. 11, 910–917.

Blunk, A.D., Akbergenova, Y., Cho, R.W., Lee, J., Walldorf, U., Xu, K., Zhong, G., Zhuang, X., and Littleton, J.T. (2014). Postsynaptic actin regulates active zone spacing and glutamate receptor apposition at the Drosophila neuromuscular junction. Mol. Cell. Neurosci. 61, 241–254.

Bozdech, Z., Zhu, J., Joachimiak, M.P., Cohen, F.E., Pulliam, B., and DeRisi, J.L. (2003). Expression profiling of the schizont and trophozoite stages of Plasmodium falciparum with a long-oligonucleotide microarray. Genome Biol. 4, R9.

Bray, D. (1984). Axonal growth in response to experimentally applied mechanical tension. Dev. Biol. 102, 379–389.

Brennecke, J., Hipfner, D.R., Stark, A., Russell, R.B., and Cohen, S.M. (2003). bantam encodes a developmentally regulated microRNA that controls cell proliferation and regulates the proapoptotic gene hid in Drosophila. Cell 113, 25–36.

Britton, J.S., and Edgar, B.A. (1998). Environmental control of the cell cycle in Drosophila: nutrition activates mitotic and endoreplicative cells by distinct mechanisms. Dev. Camb. Engl. 125, 2149–2158.

Brown, F.D., Rozelle, A.L., Yin, H.L., Balla, T., and Donaldson, J.G. (2001). Phosphatidylinositol 4,5-bisphosphate and Arf6-regulated membrane traffic. J. Cell Biol. 154, 1007–1018.

Cauna, N. (1973). The free penicillate nerve endings of the human hairy skin. J. Anat. 115, 277–288.

Chalfie, M., and Sulston, J. (1981). Developmental genetics of the mechanosensory neurons of Caenorhabditis elegans. Dev. Biol. 82, 358–370.

Chen, F., Tillberg, P.W., and Boyden, E.S. (2015). Expansion microscopy. Science 347, 543–548.

Chozinski, T.J., Halpern, A.R., Okawa, H., Kim, H.-J., Tremel, G.J., Wong, R.O.L., and Vaughan, J.C. (2016). Expansion microscopy with conventional antibodies and fluorescent proteins. Nat. Methods 13, 485–488.

Church, R.B., and Robertson, F.W. (1966). Biochemical analysis of genetic differences in the growth of Drosophila. Genet. Res. 7, 383–407.

Coleman, M.P., Conforti, L., Buckmaster, E.A., Tarlton, A., Ewing, R.M., Brown, M.C., Lyon, M.F., and Perry, V.H. (1998). An 85-kb tandem triplication in the slow Wallerian degeneration (Wlds) mouse. Proc. Natl. Acad. Sci. U. S. A. 95, 9985–9990.

Cooper, R.L., Winslow, J.L., Govind, C.K., and Atwood, H.L. (1996). Synaptic structural complexity as a factor enhancing probability of calcium-mediated transmitter release. J. Neurophysiol. 75, 2451–2466.

Devaux, J.J., and Scherer, S.S. (2005). Altered Ion Channels in an Animal Model of Charcot-Marie-Tooth Disease Type IA. J. Neurosci. 25, 1470–1480.

DiPersio, C.M., Hodivala-Dilke, K.M., Jaenisch, R., Kreidberg, J.A., and Hynes, R.O. (1997). alpha3beta1 Integrin is required for normal development of the epidermal basement membrane. J. Cell Biol. 137, 729–742.

Egami, Y., Fujii, M., Kawai, K., Ishikawa, Y., Fukuda, M., and Araki, N. (2015). Activation-Inactivation Cycling of Rab35 and ARF6 Is Required for Phagocytosis of Zymosan in RAW264 Macrophages.

Ehmann, N., Linde, S. van de, Alon, A., Ljaschenko, D., Keung, X.Z., Holm, T., Rings, A., DiAntonio, A., Hallermann, S., Ashery, U., et al. (2014). Quantitative super-resolution imaging of Bruchpilot distinguishes active zone states. Nat. Commun. 5, 4650.

Emoto, K., He, Y., Ye, B., Grueber, W.B., Adler, P.N., Jan, L.Y., and Jan, Y.-N. (2004). Control of dendritic branching and tiling by the Tricornered-kinase/Furry signaling pathway in Drosophila sensory neurons. Cell 119, 245–256.

Emoto, K., Parrish, J.Z., Jan, L.Y., and Jan, Y.-N. (2006). The tumour suppressor Hippo acts with the NDR kinases in dendritic tiling and maintenance. Nature 443, 210–213.

Feinberg, E.H., Vanhoven, M.K., Bendesky, A., Wang, G., Fetter, R.D., Shen, K., and Bargmann, C.I. (2008). GFP Reconstitution Across Synaptic Partners (GRASP) defines cell contacts and synapses in living nervous systems. Neuron 57, 353–363.

Fouquet, W., Owald, D., Wichmann, C., Mertel, S., Depner, H., Dyba, M., Hallermann, S., Kittel, R.J., Eimer, S., and Sigrist, S.J. (2009). Maturation of active zone assembly by Drosophila Bruchpilot. J. Cell Biol. 186, 129–145.

Friedrich, M.V., Schneider, M., Timpl, R., and Baumgartner, S. (2000). Perlecan domain V of Drosophila melanogaster. Sequence, recombinant analysis and tissue expression. Eur. J. Biochem. 267, 3149–3159.

Giuliani, F., Giuliani, G., Bauer, R., and Rabouille, C. (2013). Innexin 3, a New Gene Required for Dorsal Closure in Drosophila Embryo. PLOS ONE 8, e69212.

Goodman, M. (2006). Mechanosensation. WormBook.

Grueber, W.B., Jan, L.Y., and Jan, Y.N. (2002). Tiling of the Drosophila epidermis by multidendritic sensory neurons. Dev. Camb. Engl. 129, 2867–2878.

Grueber, W.B., Jan, L.Y., and Jan, Y.N. (2003). Different Levels of the Homeodomain Protein Cut Regulate Distinct Dendrite Branching Patterns of Drosophila Multidendritic Neurons. Cell 112, 805–818.

Grueber, W.B., Ye, B., Moore, A.W., Jan, L.Y., and Jan, Y.N. (2003). Dendrites of distinct classes of Drosophila sensory neurons show different capacities for homotypic repulsion. Curr. Biol. CB 13, 618–626.

Guo, Y., Wang, Y., Wang, Q., and Wang, Z. (2014). The Role of PPK26 in Drosophila Larval Mechanical Nociception. Cell Rep. 9, 1183–1190.

Gupta, V.K., Pech, U., Bhukel, A., Fulterer, A., Ender, A., Mauermann, S.F., Andlauer, T.F.M., Antwi-Adjei, E., Beuschel, C., Thriene, K., et al. (2016). Spermidine Suppresses

Age-Associated Memory Impairment by Preventing Adverse Increase of Presynaptic Active Zone Size and Release. PLoS Biol. 14, e1002563.

Hall, S. (2005). The response to injury in the peripheral nervous system. J. Bone Joint Surg. Br. 87, 1309–1319.

Hamada, M.S., and Kole, M.H.P. (2015). Myelin Loss and Axonal Ion Channel Adaptations Associated with Gray Matter Neuronal Hyperexcitability. J. Neurosci. 35, 7272–7286.

Han, C., Song, Y., Xiao, H., Wang, D., Franc, N.C., Jan, L.Y., and Jan, Y.-N. (2014). Epidermal cells are the primary phagocytes in the fragmentation and clearance of degenerating dendrites in Drosophila. Neuron 81, 544–560.

Han, C., Wang, D., Soba, P., Zhu, S., Lin, X., Jan, L.Y., and Jan, Y.-N. (2012). Integrins regulate repulsion-mediated dendritic patterning of drosophila sensory neurons by restricting dendrites in a 2D space. Neuron 73, 64–78.

Hipfner, D.R., Weigmann, K., and Cohen, S.M. (2002). The bantam gene regulates Drosophila growth. Genetics 161, 1527–1537.

Hitchcock, P.F. (1987). Constant dendritic coverage by ganglion cells with growth of the goldfish's retina. Vision Res. 27, 17–22.

Holderith, N., Lorincz, A., Katona, G., Rózsa, B., Kulik, A., Watanabe, M., and Nusser, Z. (2012). Release probability of hippocampal glutamatergic terminals scales with the size of the active zone. Nat. Neurosci. 15, 988–997.

Honda, A., Nogami, M., Yokozeki, T., Yamazaki, M., Nakamura, H., Watanabe, H., Kawamoto, K., Nakayama, K., Morris, A.J., Frohman, M.A., et al. (1999). Phosphatidylinositol 4-Phosphate 5-Kinase α Is a Downstream Effector of the Small G Protein ARF6 in Membrane Ruffle Formation. Cell 99, 521–532.

Hughes, R.A.C. (2002). Peripheral neuropathy. BMJ 324, 466–469.

Hummel, T., Krukkert, K., Roos, J., Davis, G., and Klämbt, C. (2000). Drosophila Futsch/22C10 is a MAP1B-like protein required for dendritic and axonal development. Neuron 26, 357–370.

Hwang, R.Y., Zhong, L., Xu, Y., Johnson, T., Zhang, F., Deisseroth, K., and Tracey, W.D. (2007). Nociceptive neurons protect Drosophila larvae from parasitoid wasps. Curr. Biol. CB 17, 2105–2116.

Jacinto, A., Wood, W., Balayo, T., Turmaine, M., Martinez-Arias, A., and Martin, P. (2000). Dynamic actin-based epithelial adhesion and cell matching during Drosophila dorsal closure. Curr. Biol. CB 10, 1420–1426.

Jan, L.Y., and Jan, Y.N. (1982). Antibodies to horseradish peroxidase as specific neuronal markers in Drosophila and in grasshopper embryos. Proc. Natl. Acad. Sci. U. S. A. 79, 2700–2704.

Janmey, P.A., and Lindberg, U. (2004). Cytoskeletal regulation: rich in lipids. Nat. Rev. Mol. Cell Biol. 5, 658–666.

Jasper, H., Benes, V., Schwager, C., Sauer, S., Clauder-Münster, S., Ansorge, W., and Bohmann, D. (2001). The genomic response of the Drosophila embryo to JNK signaling. Dev. Cell 1, 579–586.

Jepson, J.E.C., Shahidullah, M., Liu, D., Marchand, S.J. le, Liu, S., Wu, M.N., Levitan, I.B., Dalva, M.B., and Koh, K. (2014). Regulation of synaptic development and function by the Drosophila PDZ protein Dyschronic. Development 141, 4548–4557.

Jessen, K.R., and Mirsky, R. (2005). The origin and development of glial cells in peripheral nerves. Nat. Rev. Neurosci. 6, 671–682.

Jiang, N., Soba, P., Parker, E., Kim, C.C., and Parrish, J.Z. (2014). The microRNA bantam regulates a developmental transition in epithelial cells that restricts sensory dendrite growth. Dev. Camb. Engl. 141, 2657–2668.

Johnson, R.I., Sedgwick, A., D'Souza-Schorey, C., and Cagan, R.L. (2011). Role for a Cindr–Arf6 axis in patterning emerging epithelia. Mol. Biol. Cell 22, 4513–4526.

Kim, M.-J., and Johnson, W.A. (2014). ROS-mediated activation of Drosophila larval nociceptor neurons by UVC irradiation. BMC Neurosci. 15, 14.

Kim, M.E., Shrestha, B.R., Blazeski, R., Mason, C.A., and Grueber, W.B. (2012). Integrins establish dendrite-substrate relationships that promote dendritic self-avoidance and patterning in drosophila sensory neurons. Neuron 73, 79–91.

Kim, S.E., Coste, B., Chadha, A., Cook, B., and Patapoutian, A. (2012b). The role of Drosophila Piezo in mechanical nociception. Nature 483, 209–212.

Kittel, R.J., Wichmann, C., Rasse, T.M., Fouquet, W., Schmidt, M., Schmid, A., Wagh, D.A., Pawlu, C., Kellner, R.R., Willig, K.I., et al. (2006). Bruchpilot promotes active zone assembly, Ca2+ channel clustering, and vesicle release. Science 312, 1051–1054.

Kondo, A., Hashimoto, S., Yano, H., Nagayama, K., Mazaki, Y., and Sabe, H. (2000). A new paxillin-binding protein, PAG3/Papalpha/KIAA0400, bearing an ADP-ribosylation factor GTPase-activating protein activity, is involved in paxillin recruitment to focal adhesions and cell migration. Mol. Biol. Cell 11, 1315–1327.

Ku, T., Swaney, J., Park, J.-Y., Albanese, A., Murray, E., Cho, J.H., Park, Y.-G., Mangena, V., Chen, J., and Chung, K. (2016). Multiplexed and scalable super-resolution imaging of three-dimensional protein localization in size-adjustable tissues. Nat. Biotechnol. 34, 973–981.

Lai, H.C., and Jan, L.Y. (2006). The distribution and targeting of neuronal voltage-gated ion channels. Nat. Rev. Neurosci. 7, 548–562.

Langley, J.N., and Anderson, H.K. (1904). On the union of the fifth cervical nerve with the superior cervical ganglion. J. Physiol. 30, 439–442.

Laura, F.M., Yannick, P., and Carlo, P.S. (2016). How Schwann Cells Sort Axons: New Concepts. Neurosci. Rev. J. Bringing Neurobiol. Neurol. Psychiatry 22, 252–265.

Lepicard, S., Franco, B., de Bock, F., and Parmentier, M.-L. (2014). A presynaptic role of microtubule-associated protein 1/Futsch in Drosophila: regulation of active zone number and neurotransmitter release. J. Neurosci. Off. J. Soc. Neurosci. 34, 6759–6771.

Li, Y., Brewer, D., Burke, R.E., and Ascoli, G.A. (2005). Developmental changes in spinal motoneuron dendrites in neonatal mice. J. Comp. Neurol. 483, 304–317.

López-Sánchez, N., and Frade, J.M. (2013). Genetic evidence for p75NTR-dependent tetraploidy in cortical projection neurons from adult mice. J. Neurosci. Off. J. Soc. Neurosci. 33, 7488–7500.

Lumsden, A.G., and Davies, A.M. (1983). Earliest sensory nerve fibres are guided to peripheral targets by attractants other than nerve growth factor. Nature 306, 786–788.

MacDonald, J.M., Beach, M.G., Porpiglia, E., Sheehan, A.E., Watts, R.J., and Freeman, M.R. (2006). The Drosophila cell corpse engulfment receptor Draper mediates glial clearance of severed axons. Neuron 50, 869–881.

Mahoney, R.E., Rawson, J.M., and Eaton, B.A. (2014). An age-dependent change in the set point of synaptic homeostasis. J. Neurosci. Off. J. Soc. Neurosci. 34, 2111–2119.

Manning, L., and Doe, C.Q. (2017). Immunofluorescent antibody staining of intact Drosophila larvae. Nat. Protoc. 12, 1–14.

Marín-Teva, J.L., Dusart, I., Colin, C., Gervais, A., van Rooijen, N., and Mallat, M. (2004). Microglia promote the death of developing Purkinje cells. Neuron 41, 535–547.

Martin-Blanco, E., Pastor-Pareja, J.C., and Garcia-Bellido, A. (2000). JNK and decapentaplegic signaling control adhesiveness and cytoskeleton dynamics during thorax closure in Drosophila. Proc. Natl. Acad. Sci. U. S. A. 97, 7888–7893.

Mataga, N., Nagai, N., and Hensch, T.K. (2002). Permissive proteolytic activity for visual cortical plasticity. Proc. Natl. Acad. Sci. U. S. A. 99, 7717–7721.

Matkovic, T., Siebert, M., Knoche, E., Depner, H., Mertel, S., Owald, D., Schmidt, M., Thomas, U., Sickmann, A., Kamin, D., et al. (2013). The Bruchpilot cytomatrix determines the size of the readily releasable pool of synaptic vesicles. J. Cell Biol. 202, 667–683.

Morell, M., Czihal, P., Hoffmann, R., Otvos, L., Avilés, F.X., and Ventura, S. (2008). Monitoring the interference of protein-protein interactions in vivo by bimolecular fluorescence complementation: the DnaK case. Proteomics 8, 3433–3442.

Morillo, S.M., Escoll, P., de la Hera, A., and Frade, J.M. (2010). Somatic tetraploidy in specific chick retinal ganglion cells induced by nerve growth factor. Proc. Natl. Acad. Sci. U. S. A. 107, 109–114.

Morin, X., Daneman, R., Zavortink, M., and Chia, W. (2001). A protein trap strategy to detect GFP-tagged proteins expressed from their endogenous loci in Drosophila. Proc. Natl. Acad. Sci. U. S. A. 98, 15050–15055.

Moss, J., and Vaughan, M. (1998). Molecules in the ARF orbit. J. Biol. Chem. 273, 21431–21434.

Nave, K.-A., and Salzer, J.L. (2006). Axonal regulation of myelination by neuregulin 1. Curr. Opin. Neurobiol. 16, 492–500.

Neely, G.G., Keene, A.C., Duchek, P., Chang, E.C., Wang, Q.-P., Aksoy, Y.A., Rosenzweig, M., Costigan, M., Woolf, C.J., Garrity, P.A., et al. (2011). TrpA1 Regulates Thermal Nociception in Drosophila. PLOS ONE 6, e24343.

Newbern, J., and Birchmeier, C. (2010). Nrg1/ErbB signaling networks in Schwann cell development and myelination. Semin. Cell Dev. Biol. 21, 922–928.

O'Brien, G.S., Rieger, S., Wang, F., Smolen, G.A., Gonzalez, R.E., Buchanan, J., and Sagasti, A. (2012). Coordinate development of skin cells and cutaneous sensory axons in zebrafish. J. Comp. Neurol. 520, 816–831.

Oray, S., Majewska, A., and Sur, M. (2004). Dendritic spine dynamics are regulated by monocular deprivation and extracellular matrix degradation. Neuron 44, 1021–1030.

Ostrowski, S., Dierick, H.A., and Bejsovec, A. (2002). Genetic control of cuticle formation during embryonic development of Drosophila melanogaster. Genetics 161, 171–182.

Park, S.Y., and Asano, M. (2008). The origin recognition complex is dispensable for endoreplication in Drosophila. Proc. Natl. Acad. Sci. U. S. A. 105, 12343–12348.

Parrish, J.Z., Emoto, K., Jan, L.Y., and Jan, Y.N. (2007). Polycomb genes interact with the tumor suppressor genes hippo and warts in the maintenance of Drosophila sensory neuron dendrites. Genes Dev. 21, 956–972.

Parrish, J.Z., Xu, P., Kim, C.C., Jan, L.Y., and Jan, Y.N. (2009). The microRNA bantam functions in epithelial cells to regulate scaling growth of dendrite arbors in drosophila sensory neurons. Neuron 63, 788–802.

Pédelacq, J.-D., Cabantous, S., Tran, T., Terwilliger, T.C., and Waldo, G.S. (2006). Engineering and characterization of a superfolder green fluorescent protein. Nat. Biotechnol. 24, 79–88.

Pernas, L., and Scorrano, L. (2016). Mito-Morphosis: Mitochondrial Fusion, Fission, and Cristae Remodeling as Key Mediators of Cellular Function. Annu. Rev. Physiol. 78, 505–531.

Pielage, J., Fetter, R.D., and Davis, G.W. (2006). A postsynaptic spectrin scaffold defines active zone size, spacing, and efficacy at the Drosophila neuromuscular junction. J. Cell Biol. 175, 491–503.

Pierce, S.B., Yost, C., Britton, J.S., Loo, L.W.M., Flynn, E.M., Edgar, B.A., and Eisenman, R.N. (2004). dMyc is required for larval growth and endoreplication in Drosophila. Dev. Camb. Engl. 131, 2317–2327.

Pimentel, A.C., and Venkatesh, T.R. (2005). rap gene encodes Fizzy-related protein (Fzr) and regulates cell proliferation and pattern formation in the developing Drosophila eye-antennal disc. Dev. Biol. 285, 436–446.

Poliak, S., Matlis, S., Ullmer, C., Scherer, S.S., and Peles, E. (2002). Distinct claudins and associated PDZ proteins form different autotypic tight junctions in myelinating Schwann cells. J. Cell Biol. 159, 361–372.

Propst, J.W., and Ko, C.P. (1987). Correlations between active zone ultrastructure and synaptic function studied with freeze-fracture of physiologically identified neuromuscular junctions. J. Neurosci. Off. J. Soc. Neurosci. 7, 3654–3664.

Ramoa, A.S., Campbell, G., and Shatz, C.J. (1988). Dendritic growth and remodeling of cat retinal ganglion cells during fetal and postnatal development. J. Neurosci. Off. J. Soc. Neurosci. 8, 4239–4261.

Rasmussen, J.P., Sack, G.S., Martin, S.M., and Sagasti, A. (2015). Vertebrate Epidermal Cells Are Broad-Specificity Phagocytes That Clear Sensory Axon Debris. J. Neurosci. 35, 559–570.

Ren, L., Liang, H., Diao, L., and He, S. (2010). Changing dendritic field size of mouse retinal ganglion cells in early postnatal development. Dev. Neurobiol. 70, 397–407.

Reversi, A., Loeser, E., Subramanian, D., Schultz, C., and De Renzis, S. (2014). Plasma membrane phosphoinositide balance regulates cell shape during Drosophila embryo morphogenesis. J. Cell Biol. 205, 395–408.

Roggenkamp, D., Köpnick, S., Stäb, F., Wenck, H., Schmelz, M., and Neufang, G. (2013). Epidermal Nerve Fibers Modulate Keratinocyte Growth via Neuropeptide Signaling in an Innervated Skin Model. J. Invest. Dermatol. 133, 1620–1628.

Roosterman, D., Goerge, T., Schneider, S.W., Bunnett, N.W., and Steinhoff, M. (2006). Neuronal control of skin function: the skin as a neuroimmunoendocrine organ. Physiol. Rev. 86, 1309–1379.

Scherer, S.S., Xu, Y.T., Nelles, E., Fischbeck, K., Willecke, K., and Bone, L.J. (1998). Connexin32-null mice develop demyelinating peripheral neuropathy. Glia 24, 8–20.

Schiefermeier, N., Teis, D., and Huber, L.A. (2011). Endosomal signaling and cell migration. Curr. Opin. Cell Biol. 23, 615–620.

Scott, C.C., Dobson, W., Botelho, R.J., Coady-Osberg, N., Chavrier, P., Knecht, D.A., Heath, C., Stahl, P., and Grinstein, S. (2005). Phosphatidylinositol-4,5-bisphosphate hydrolysis directs actin remodeling during phagocytosis. J. Cell Biol. 169, 139–149.

Sechi, A.S., and Wehland, J. (2000). The actin cytoskeleton and plasma membrane connection: PtdIns(4,5)P(2) influences cytoskeletal protein activity at the plasma membrane. J. Cell Sci. 113 Pt 21, 3685–3695.

Sherman, D.L., and Brophy, P.J. (2005). Mechanisms of axon ensheathment and myelin growth. Nat. Rev. Neurosci. 6, 683–690.

Shibasaki, Y., Ishihara, H., Kizuki, N., Asano, T., Oka, Y., and Yazaki, Y. (1997). Massive actin polymerization induced by phosphatidylinositol-4-phosphate 5-kinase in vivo. J. Biol. Chem. 272, 7578–7581.

Sigrist, S.J., and Lehner, C.F. (1997). Drosophila fizzy-related down-regulates mitotic cyclins and is required for cell proliferation arrest and entry into endocycles. Cell 90, 671–681.

Smith, A.V., and Orr-Weaver, T.L. (1991). The regulation of the cell cycle during Drosophila embryogenesis: the transition to polyteny. Dev. Camb. Engl. 112, 997–1008.

Snaidero, N., Möbius, W., Czopka, T., Hekking, L.H.P., Mathisen, C., Verkleij, D., Goebbels, S., Edgar, J., Merkler, D., Lyons, D.A., et al. (2014). Myelin membrane wrapping of CNS axons by PI(3,4,5)P3-dependent polarized growth at the inner tongue. Cell 156, 277–290.

Südhof, T.C. (2012). The presynaptic active zone. Neuron 75, 11–25.

Sugimura, K., Yamamoto, M., Niwa, R., Satoh, D., Goto, S., Taniguchi, M., Hayashi, S., and Uemura, T. (2003). Distinct developmental modes and lesion-induced reactions of dendrites of two classes of Drosophila sensory neurons. J. Neurosci. Off. J. Soc. Neurosci. 23, 3752–3760.

Suter, U., and Scherer, S.S. (2003). Disease mechanisms in inherited neuropathies. Nat. Rev. Neurosci. 4, 714–726.

Tillberg, P.W., Chen, F., Piatkevich, K.D., Zhao, Y., Yu, C.-C.J., English, B.P., Gao, L., Martorell, A., Suk, H.-J., Yoshida, F., et al. (2016). Protein-retention expansion microscopy of cells and tissues labeled using standard fluorescent proteins and antibodies. Nat. Biotechnol. 34, 987–992.

Tracey, W.D., Wilson, R.I., Laurent, G., and Benzer, S. (2003). painless, a Drosophila Gene Essential for Nociception. Cell 113, 261–273.

Trapp, B.D., Andrews, S.B., Wong, A., O'Connell, M., and Griffin, J.W. (1989). Co-localization of the myelin-associated glycoprotein and the microfilament components, F-actin and spectrin, in Schwann cells of myelinated nerve fibres. J. Neurocytol. 18, 47–60.

Tricaud, N., Perrin-Tricaud, C., Brusés, J.L., and Rutishauser, U. (2005). Adherens Junctions in Myelinating Schwann Cells Stabilize Schmidt-Lanterman Incisures via Recruitment of p120 Catenin to E-Cadherin. J. Neurosci. 25, 3259–3269.

Truman, J.W., and Bate, M. (1988). Spatial and temporal patterns of neurogenesis in the central nervous system of Drosophila melanogaster. Dev. Biol. 125, 145–157.

Tusher, V.G., Tibshirani, R., and Chu, G. (2001). Significance analysis of microarrays applied to the ionizing radiation response. Proc. Natl. Acad. Sci. U. S. A. 98, 5116–5121.

Unhavaithaya, Y., and Orr-Weaver, T.L. (2012). Polyploidization of glia in neural development links tissue growth to blood-brain barrier integrity. Genes Dev. 26, 31–36.

Wagh, D.A., Rasse, T.M., Asan, E., Hofbauer, A., Schwenkert, I., Dürrbeck, H., Buchner, S., Dabauvalle, M.-C., Schmidt, M., Qin, G., et al. (2006). Bruchpilot, a protein with homology to ELKS/CAST, is required for structural integrity and function of synaptic active zones in Drosophila. Neuron 49, 833–844.

Wagner, N., Laugks, U., Heckmann, M., Asan, E., and Neuser, K. (2015). Aging Drosophila melanogaster display altered pre- and postsynaptic ultrastructure at adult neuromuscular junctions. J. Comp. Neurol. 523, 2457–2475.

Wang, F., Wolfson, S.N., Gharib, A., and Sagasti, A. (2012). LAR receptor tyrosine phosphatases and HSPGs guide peripheral sensory axons to the skin. Curr. Biol. 22, 373–382.

Watts, R.J., Schuldiner, O., Perrino, J., Larsen, C., and Luo, L. (2004). Glia engulf degenerating axons during developmental axon pruning. Curr. Biol. CB 14, 678–684.

Weiss, A., Herzig, A., Jacobs, H., and Lehner, C.F. (1998). Continuous Cyclin E expression inhibits progression through endoreduplication cycles in Drosophila. Curr. Biol. CB 8, 239–242.

Weyhersmüller, A., Hallermann, S., Wagner, N., and Eilers, J. (2011). Rapid active zone remodeling during synaptic plasticity. J. Neurosci. Off. J. Soc. Neurosci. 31, 6041–6052.

Williams, D.W., and Truman, J.W. (2005). Cellular mechanisms of dendrite pruning in Drosophila: insights from in vivo time-lapse of remodeling dendritic arborizing sensory neurons. Dev. Camb. Engl. 132, 3631–3642.

Winicur, S., and Mitchell, H.K. (1974). Chitinase activity during Drosophila development. J. Insect Physiol. 20, 1795–1805.

Wong, R., Hadjiyanni, I., Wei, H.-C., Polevoy, G., McBride, R., Sem, K.-P., and Brill, J.A. (2005). PIP2 Hydrolysis and Calcium Release Are Required for Cytokinesis in Drosophila Spermatocytes. Curr. Biol. 15, 1401–1406.

Xiang, Y., Yuan, Q., Vogt, N., Looger, L.L., Jan, L.Y., and Jan, Y.N. (2010). Light-avoidance-mediating photoreceptors tile the Drosophila larval body wall. Nature 468, 921–926.

Yamagishi, M., Ito, E., and Matsuo, R. (2011). DNA endoreplication in the brain neurons during body growth of an adult slug. J. Neurosci. Off. J. Soc. Neurosci. 31, 5596–5604.

Yan, S., Lv, Z., Winterhoff, M., Wenzl, C., Zobel, T., Faix, J., Bogdan, S., and Grosshans, J. (2013a). The F-BAR protein Cip4/Toca-1 antagonizes the formin Diaphanous in membrane stabilization and compartmentalization. J Cell Sci 126, 1796–1805.

Yan, Z., Zhang, W., He, Y., Gorczyca, D., Xiang, Y., Cheng, L.E., Meltzer, S., Jan, L.Y., and Jan, Y.N. (2013b). Drosophila NOMPC is a mechanotransduction channel subunit for gentle-touch sensation. Nature 493, 221–225.

Yasunaga, K., Kanamori, T., Morikawa, R., Suzuki, E., and Emoto, K. (2010). Dendrite reshaping of adult Drosophila sensory neurons requires matrix metalloproteinase-mediated modification of the basement membranes. Dev. Cell 18, 621–632.

Zhong, L., Hwang, R.Y., and Tracey, W.D. (2010). Pickpocket Is a DEG/ENaC Protein Required for Mechanical Nociception in Drosophila Larvae. Curr. Biol. 20, 429–434.

Zielke, N., Querings, S., Rottig, C., Lehner, C., and Sprenger, F. (2008). The anaphase-promoting complex/cyclosome (APC/C) is required for rereplication control in endoreplication cycles. Genes Dev. 22, 1690–1703.

Zipursky, S.L., Venkatesh, T.R., Teplow, D.B., and Benzer, S. (1984). Neuronal development in the Drosophila retina: monoclonal antibodies as molecular probes. Cell 36, 15–26.

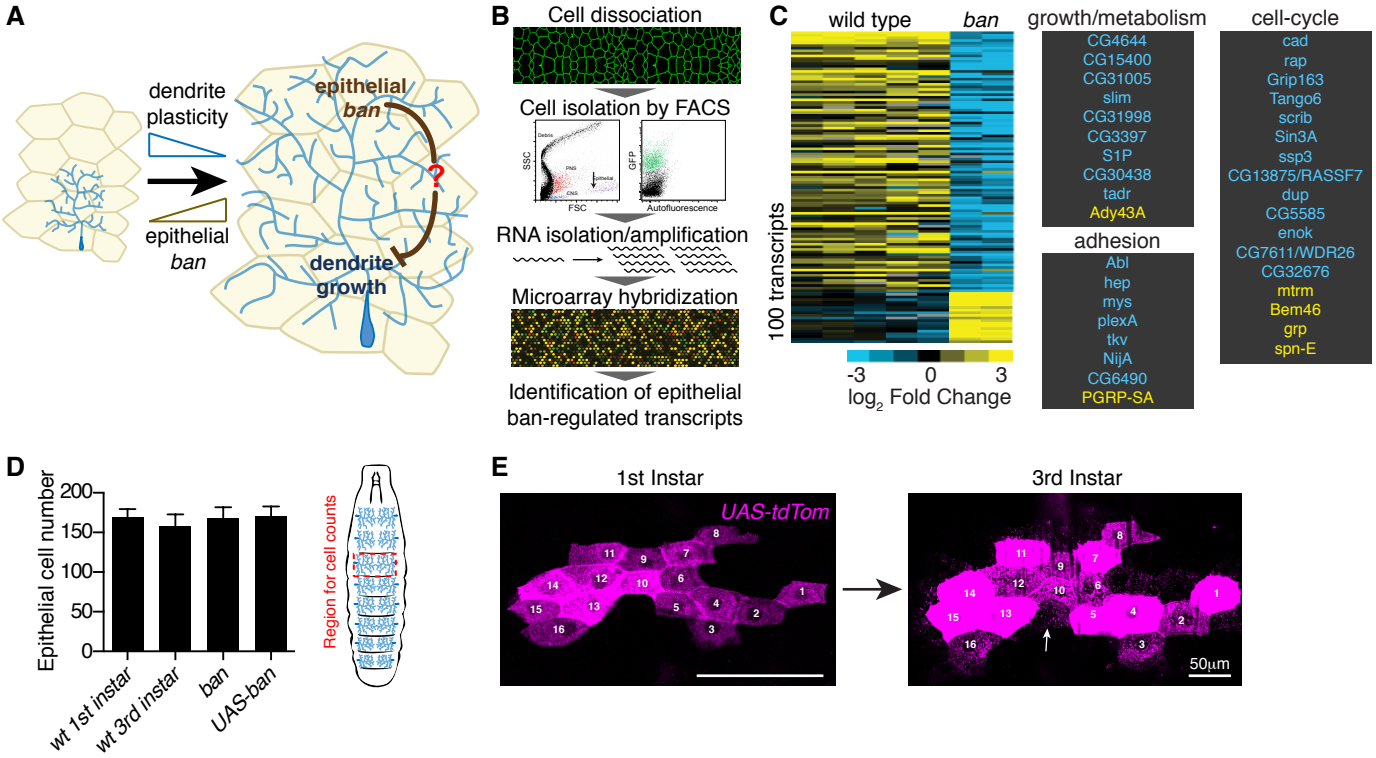

Figure 1.1. Identification of substrate-derived regulators of dendrite growth.
(A) Schematic depicting the role that ban plays in regulating dendrite structural plasticity. (B) Workflow for microarray expression profiling. (C) Heat map depicting ban-regulated epithelial transcripts. Significantly deregulated transcripts involved in cell growth/metabolism, adhesion, and the cell cycle are listed. (D) Body wall epithelial cell number counts in a region bounded by dorsal C4da neurons and segment borders (red hatched rectangle) using DAPI to label nuclei and anti-Mys staining to demarcate cell boundaries. Counts were restricted to segments A2-A4; n>10 segments for each genotype. (E) Time lapse imaging of epithelial cell clones (hs-flp; actin>CD2>Gal4/+; UAS-tdTomato/+) in newly eclosed 1st instar larvae (left) and 3rd instar larvae (right). In this example, all of the cells labeled in 1st instar larvae (numbered) are present in the same relative position in 3rd instar larvae. Occasionally, additional cells are weakly labeled in 3rd instar (arrow); these cells were present in the same position in 1st instar but label had not accumulated to detectable levels.

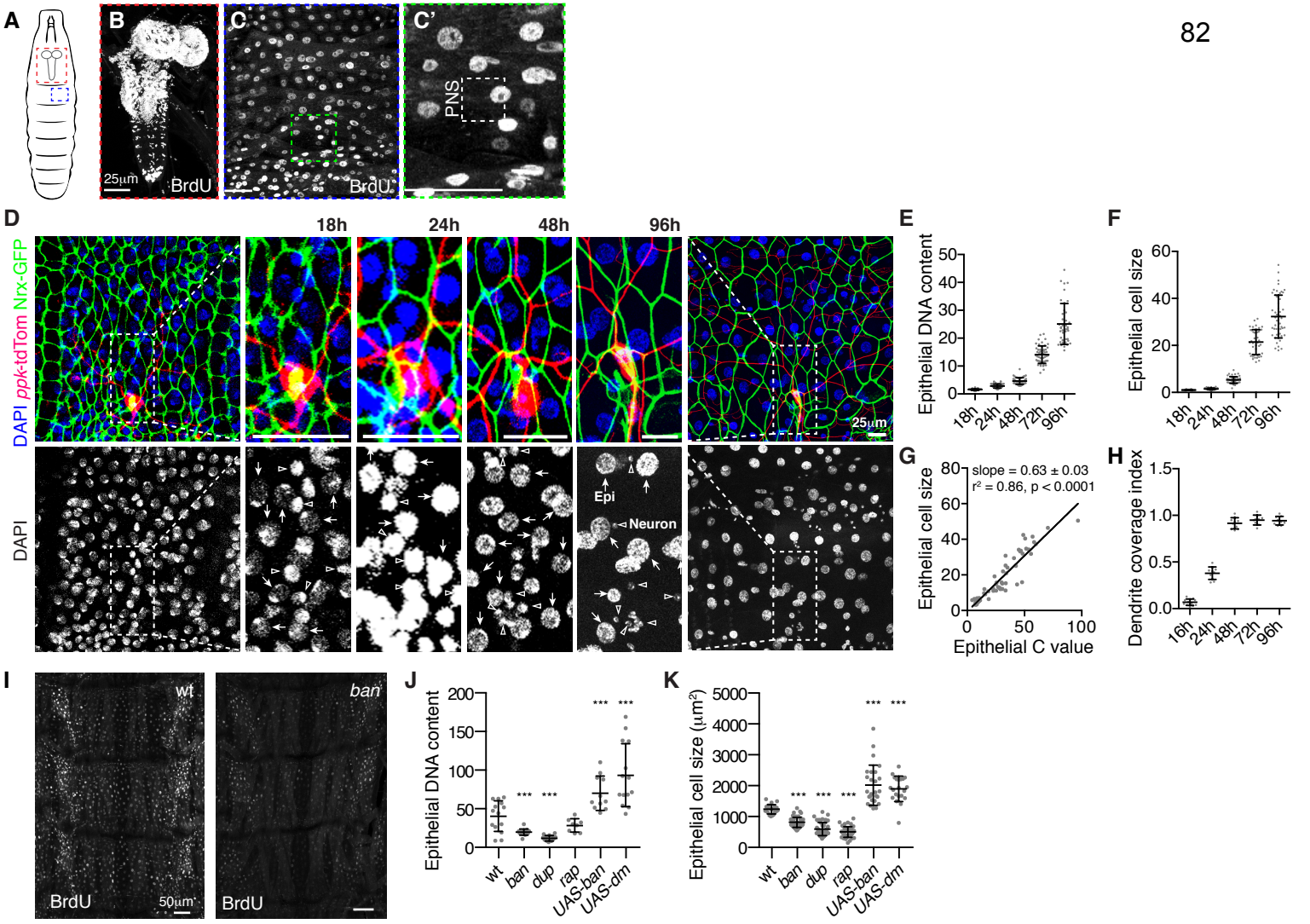

Figure 1.2. ban regulates a developmental growth transition in epithelial cells.
(A-C) BrdU incorporation in Drosophila larvae. BrdU incorporation in the larval brain (B) and the larval body wall (C). A single dorsal abdominal hemisegment is shown. (C') Region containing the dorsal cluster of larval PNS neurons; these neurons do not incorporate BrdU. (D-G) Monitoring the relationship between cell size and DNA content in body wall epithelial cells. (D) Embryos (18h) or larvae carrying markers to label C4da dendrites (ppk-tdTomato) and epithelial cells (Nrx-IV::GFP) were injected with DAPI and imaged live at the indicated time to allow simultaneous measurement of DNA content, epithelial cell size and dendrite coverage. Arrows mark epithelial nuclei and carats mark neuronal nuclei in DAPI panels. (E) Scatter plot of epithelial cell size normalized to the mean epithelial size at 18h AEL, which was measured by tracing the cell membrane labeled by NrxIV-GFP and measuring the area of the polygon. (F) Scatter plot showing epithelial DNA content during embryonic and larval development. n≥50 cells for each genotype in (E-F). (G) Regression analysis of the relationship between epithelial cell size and DNA content. 10 measurements each from 18h, 24h, 36h, 48h, 72h, and 96h were used for the analysis and the pattern of residuals supports a linear model. (H) Scatter plot depicting dendrite coverage index, the proportion of the body wall covered by C4da dendrites (n≥8 dendrites at each timepoint). (I) BrdU incorporation in representative wild type (wt) and ban mutant larvae. WT and ban larvae were processed in the same tube and imaged under identical conditions. (J-K) Scatter plots depict effects of endoreplication on (J) epithelial DNA content and (K) cell size in 120h AEL larvae of the indicated genotype. For J-K, larva were filleted, fixed, and stained with DAPI and Mys antibodies, and cell size was measured by tracing the plasma membrane labeled by anti-Mys staining; n≥20 cells for each genotype. Error bars depict the mean and 95% confidence interval and each data point is a measurement from a single cell. Scale bars: 25µm for B-D, 50µm for H.

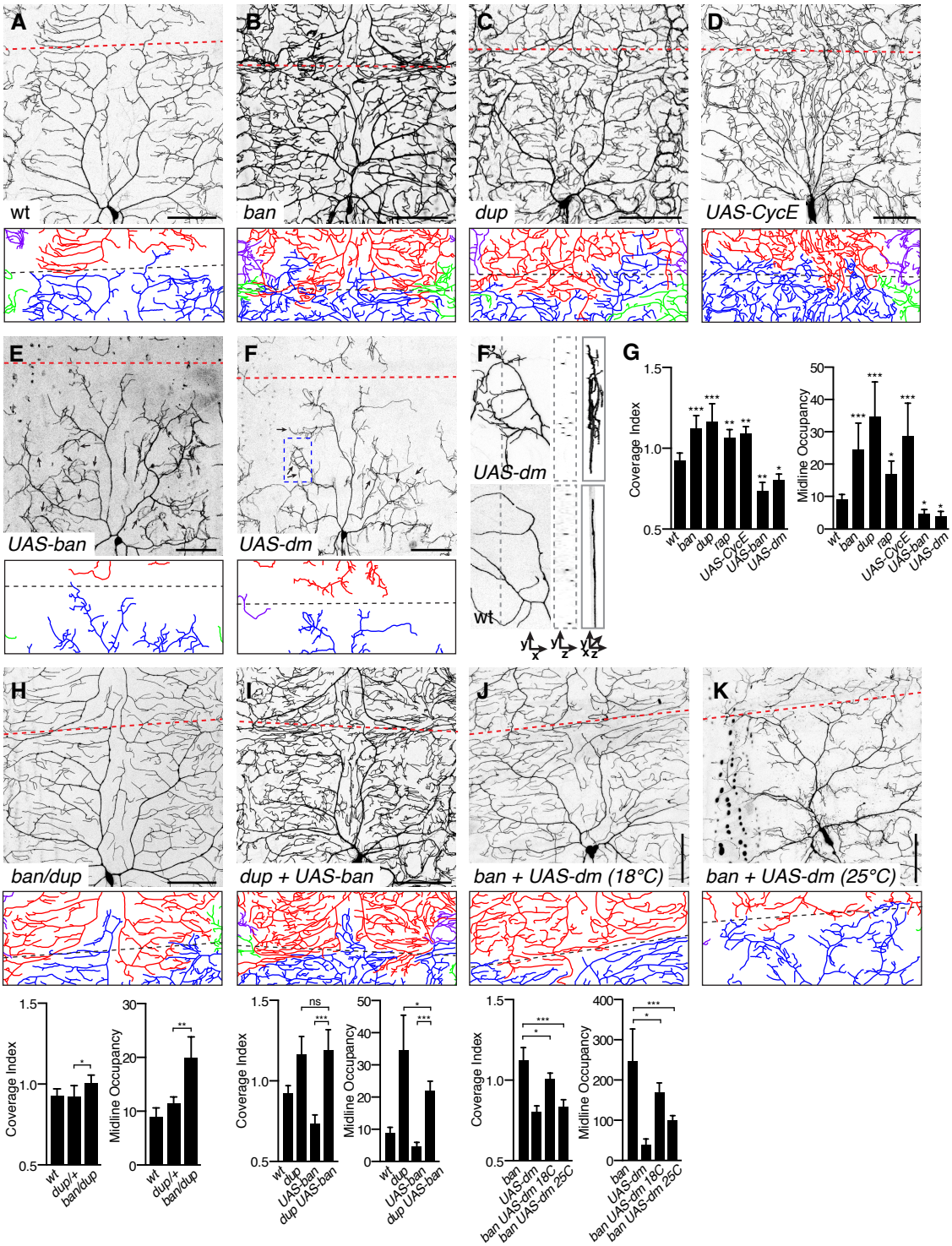

Figure 1.3. Epithelial endoreplication influences dendrite growth.
(A-D) Effects of reduced epithelial endoreplication on C4da dendrite coverage. Compared to wild type (wt) controls (A), blocking endoreplication with mutations in ban (B), dup (C), or epithelial Cyclin E overexpression (D) led to unrestrained dendrite growth, including growth beyond normal boundaries (e.g. dorsal midline; red hatched line in images, black hatched line in traces). (E-F) Effects of excess epithelial endoreplication on C4da dendrite growth. Epithelial overexpression of ban (E), or dm (F) led to reduction in dendrite growth, exaggerated wrapping of individual epithelial cells by dendrites (arrows) and increased 3D dendrite occupancy. (F') 3D orientation of dendrites. YZ cross-section and 3D rendering of region of interest is shown. The region of interest for UAS-dm corresponds to the boxed region in (F) and the corresponding region is shown for a wild type C4da dendrite. (G) Quantification of dendrite coverage index and midline occupancy (µm dendrite length/1000µm2). (H-K) Epistasis analysis of ban and endoreplication machinery. Representative dendrite images of ban/dup trans-heterozygotes (H), dup mutant larvae with epithelial ban overexpression (I), and ban mutants overexpressing dm in epithelial cells reared at 18°C for moderate dm expression (J) or 25°C for high dm expression (K). Traces depict midline dendrites. n≥8 neurons for each measurement in (G, H-J). Error bars represent standard deviation. *p<0.05, **p<0.01, **p<0.001; ns, not significant; one way ANOVA with a post-hoc Dunnett's test.

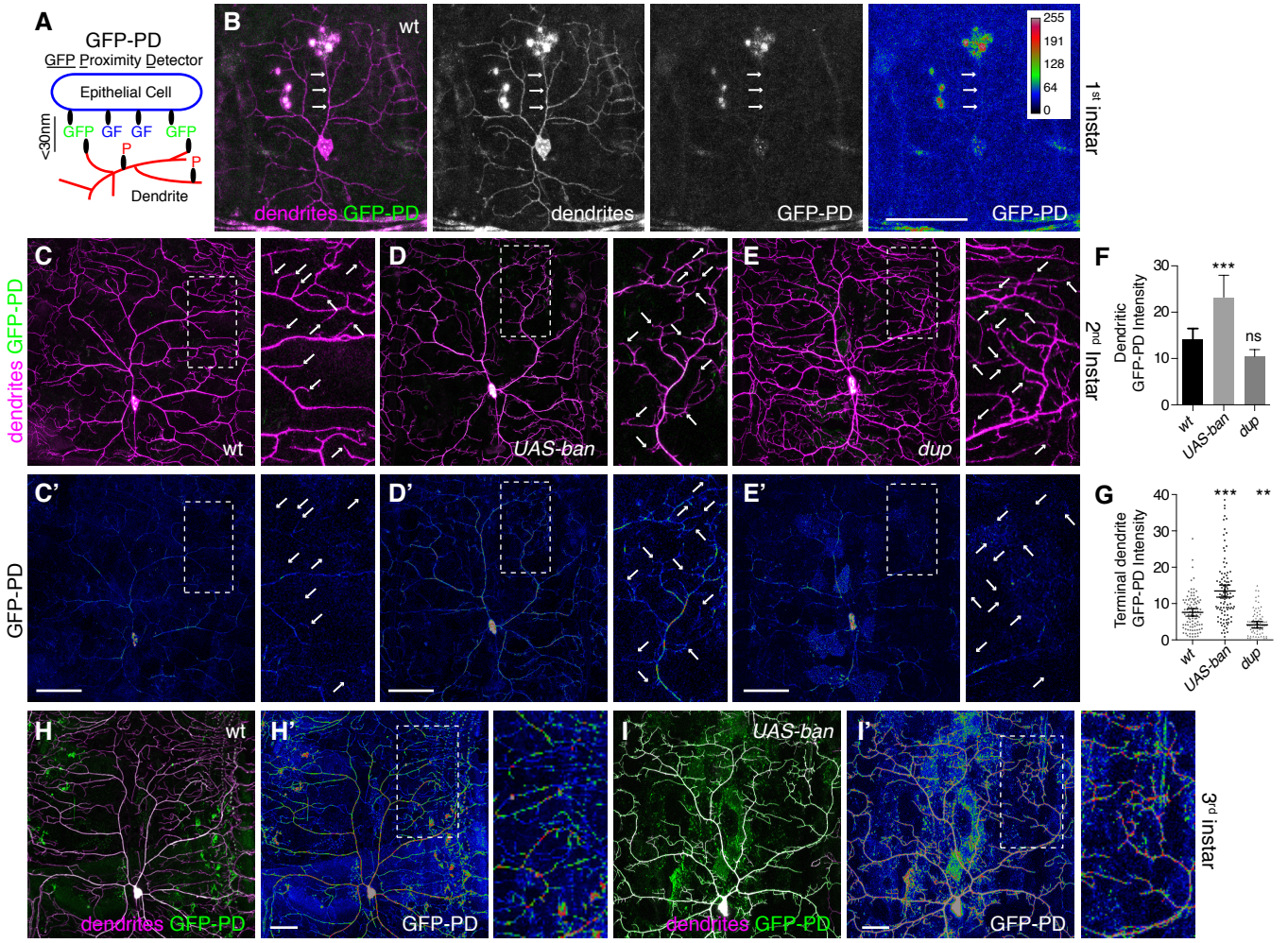

Figure 1.4. Dendrite-epithelia proximity is developmentally regulated.
(A) GFP-PD schematic. Expressing one membrane tethered portion of GFP (GF; strands 1-10 of the GFP beta sheet) in epithelial cells and the other membrane tethered portion in neurons (P; strand 11 of the beta sheet), allows for high resolution in vivo analysis of dendrite-substrate proximity. (B) Dendrite-epithelia GFP-PD signal in 1st instar larvae. ppk-spGFP11-CD4-tdTomato labels dendrites independent of GFP-PD signal. GFP-PD signal is only slightly above background in dendrites (arrows) at this stage; GFP-PD intensity is color-coded according to a lookup table (right). (C-G) Dendrite-epithelia proximity in 2nd instar larvae. Top, merged image showing distribution of GFP-PD in the dendrite arbor of wt (C), epithelial ban overexpressing (D) or dup mutant (E) larvae. Bottom, GFP-PD signal intensity. Arrows mark the tips of a subset of terminal dendrites. (F) Quantification of dendrite-epithelia GFP-PD signal from 2nd instar larvae. Intensity values were measured along the entire dendrite arbor and mean values (following background subtraction) for 10 neurons of each genotype are plotted. Error bars represent standard deviation. (G) Scatter plot showing the mean and 95% confidence interval for terminal dendrite GFP-PD intensity (n≥200 terminal dendrites for each genotype). *p<0.05, **p<0.01, ***p<0.001, ns, not significant, compared to wt; one way ANOVA with a post-hoc Dunnett's test. (H-I) Dendrite-epithelia GFP-PD signal in 3rd instar larvae. Epithelial ban overexpression leads to increased GFP-PD signal intensity, especially in terminal dendrites, suggesting that ban promotes dendrite-substrate proximity. Scale bars: 50μm

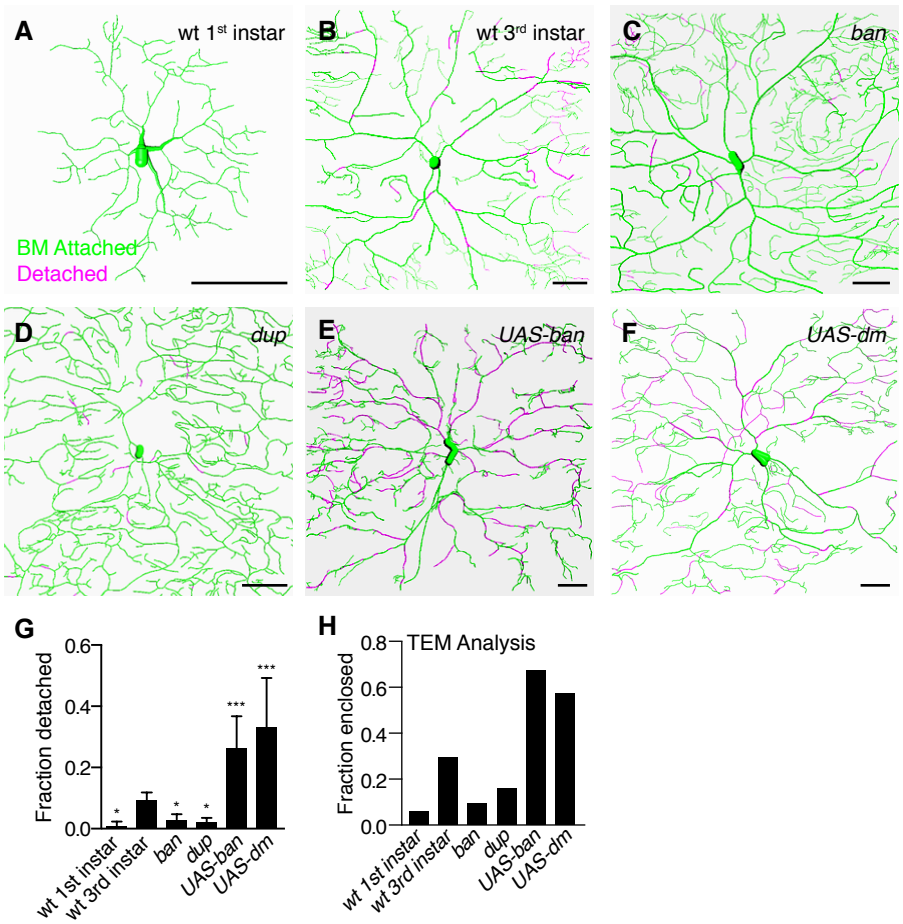

Figure 1.5. Epithelial growth program influences dendrite-ECM attachment.
Live imaging of dendrites and ECM using a neuronally-expressed membrane marker (ppk-CD4-tdTomato) and a GFP exon trap in Drosophila collagen IV (vkg-GFP) to monitor dendrite-ECM colocalization in 1st instar wt (A), 3rd instar wt (B), ban mutant (C), epithelial ban overexpressing (D), dup mutant (E) and epithelial dm overexpressing larvae (F). Representative maximum projections of 3D stacks captured by taking 200nm optical sections are shown in (A) and (B). Following deconvolution, colocalization was measured between dendrites and Vkg-GFP (see Fig. S4); in traces, dendrites that colocalize with Vkg-GFP are colored green whereas detached (apically shifted) dendrites are colored magenta. Similar results were obtained using an additional ECM marker (Fig. S3). (G) Quantification of dendrite detachment from the ECM (n≥10 dendrite arbors for each genotype). (H) TEM analysis of epithelia-dendrite interactions demonstrates that epithelial internalization of dendrites is developmentally regulated by endoreplication. TEM analysis of the fraction of dendrites (n≥50 dendrites for all genotypes) enclosed inside epithelial cells is shown for the indicated genotypes. Other than wt 1st instar samples, all samples were from 3rd instar larvae. *p<0.05, **p<0.01, ***p<0.001 compared to wt 3rd instar; one way ANOVA with a post-hoc Dunnett's test.

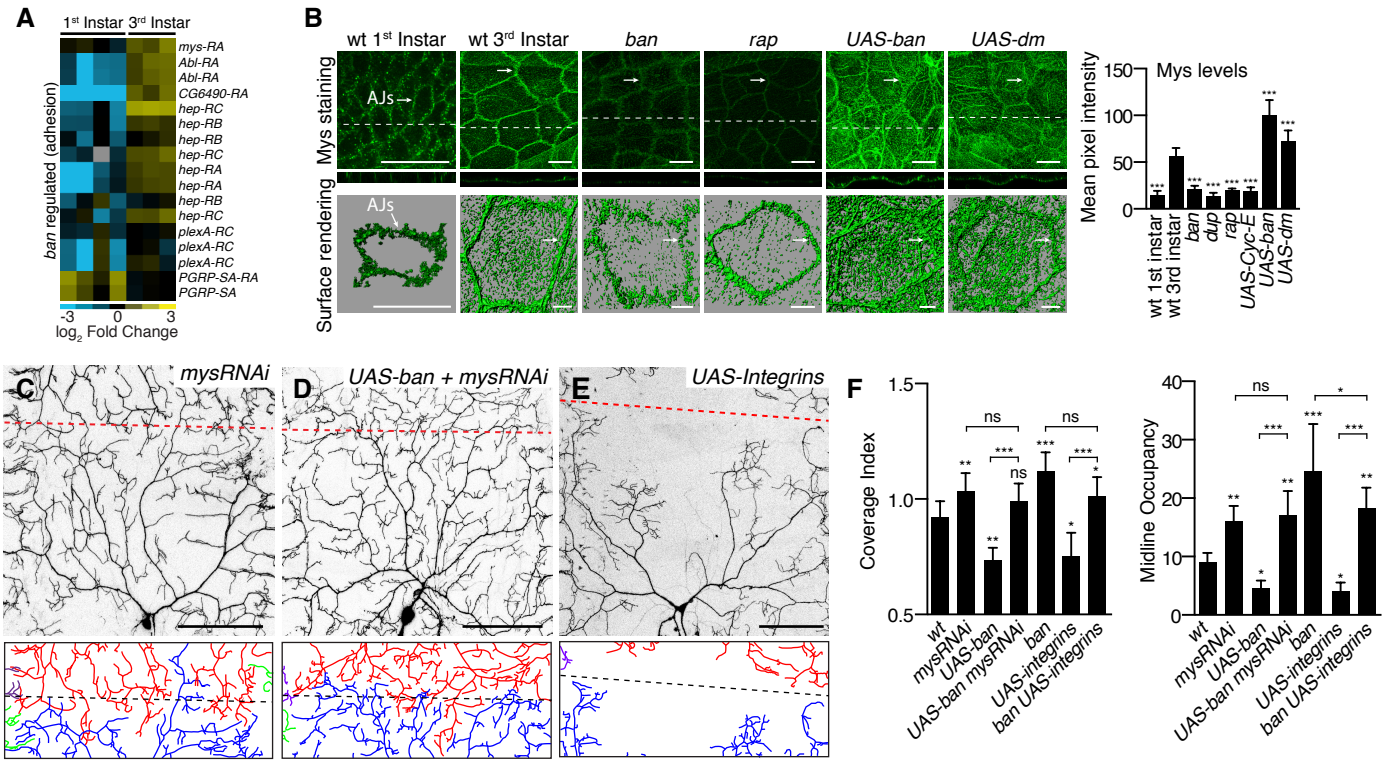

Figure 1.6. Epithelial growth program influences dendrite-ECM attachment.
Live imaging of dendrites and ECM using a neuronally-expressed membrane marker (ppk-CD4-tdTomato) and a GFP exon trap in Drosophila collagen IV (vkg-GFP) to monitor dendrite-ECM colocalization in 1st instar wt (A), 3rd instar wt (B), ban mutant (C), epithelial ban overexpressing (D), dup mutant (E) and epithelial dm overexpressing larvae (F). Representative maximum projections of 3D stacks captured by taking 200nm optical sections are shown in (A) and (B). Following deconvolution, colocalization was measured between dendrites and Vkg-GFP (see Fig. S4); in traces, dendrites that colocalize with Vkg-GFP are colored green whereas detached (apically shifted) dendrites are colored magenta. Similar results were obtained using an additional ECM marker (Fig. S3). (G) Quantification of dendrite detachment from the ECM (n≥10 dendrite arbors for each genotype). (H) TEM analysis of epithelia-dendrite interactions demonstrates that epithelial internalization of dendrites is developmentally regulated by endoreplication. TEM analysis of the fraction of dendrites (n≥50 dendrites for all genotypes) enclosed inside epithelial cells is shown for the indicated genotypes. Other than wt 1st instar samples, all samples were from 3rd instar larvae. *p<0.05, **p<0.01, ***p<0.001 compared to wt 3rd instar; one way ANOVA with a post-hoc Dunnett's test

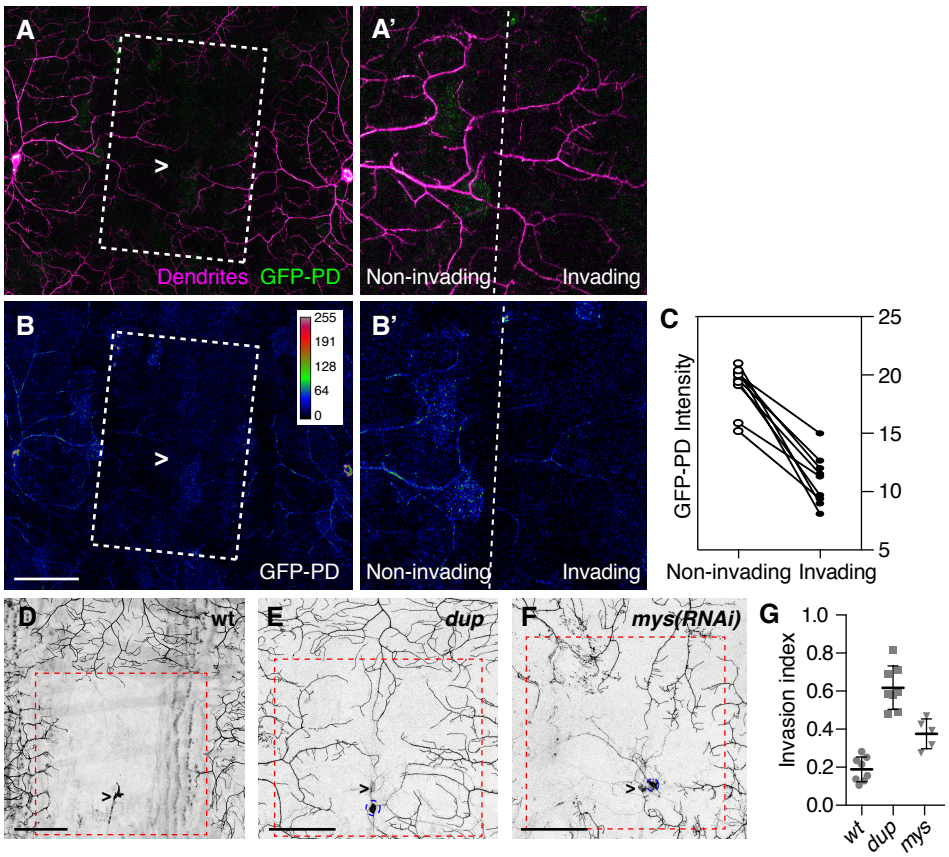

Figure 1.7. Epithelia-BM attachment influences structural plasticity of dendrites.

(A-C) Dendrite-epithelia interactions differ in invading and non-invading dendrites. Merged image (A) and GFP-PD signal (B) 48hrs after ablation of a single C4da neuron (the carat marks the soma and the white box marks the dendritic territory of the ablated neuron). (B' and C') Dendrite growth and GFP-PD signal at the receptive field boundary (dashed line) of the ablated neuron. Invading dendrites grow beyond this boundary and non-invading dendrites remain on the left of side of the boundary. Neurons express ppk-spGFP11-CD4-tdTomato and epithelia express UAS-spGFP1-10-CD4-mCer. (C) Mean GFP-PD intensity values for invading dendrites and neighboring non-invading dendrites from the same neuron (n=9 neurons). (D-G) C4da neurons in newly eclosed 2nd instar larvae were ablated with a focused laser beam and dendrite invasion into unoccupied territory was monitored 48hr post-ablation. Hatched red boxes demarcate the territory covered by the ablated neuron and carats mark the position of the ablated cell body. Dendrite invasion is shown for (D) Control, (E) dup mutant, and (F) epithelia-specific mys(RNAi) larvae. The marker stochastically labels class III neurons (blue dashed circles). (G) Scatter plot depicting mean and standard deviation for dendrite invasion of the indicated mutants (n≥8 neurons for each genotype)

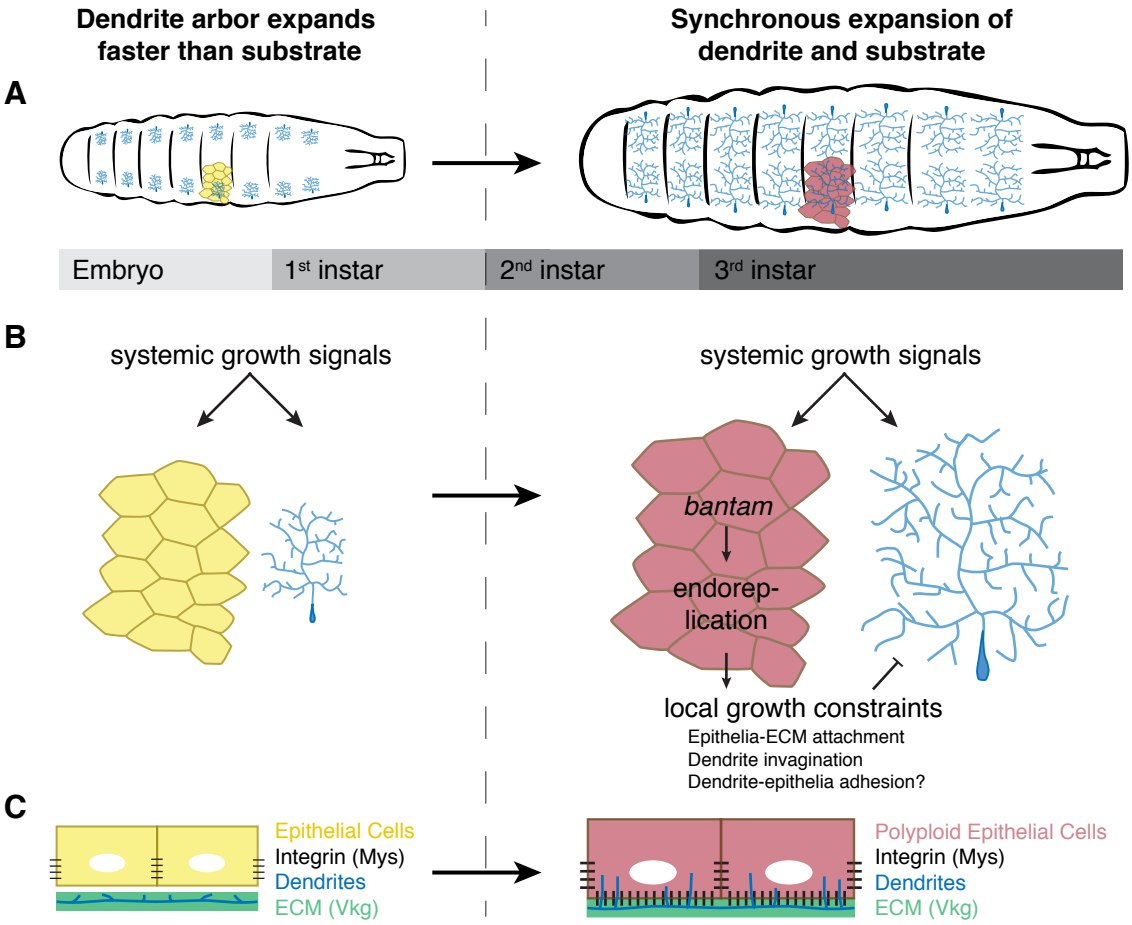

Figure 1.8. Model depicting control of dendrite expansion at different stages in larval development. (A) Biphasic growth of C4da dendrites. Early in develop-ment, dendrites expand faster than their substrate to establish complete cover-age of their substrate. After the 1st/2nd instar transition, dendrites expand in proportion to their substrate. (B) For the duration of larval development both dendrites and epithelial cells constantly grow in response to systemic growth cues. During proportional growth of dendrite and substrate, epithelial endorepli-cation causes changes in adhesive properties of epithelial cells, locally constrain-ing dendrite growth. (C) Epithelial expression of Integrin (black dashed lines) and epithelial invagination of dendrites (blue) are developmentally regulated.

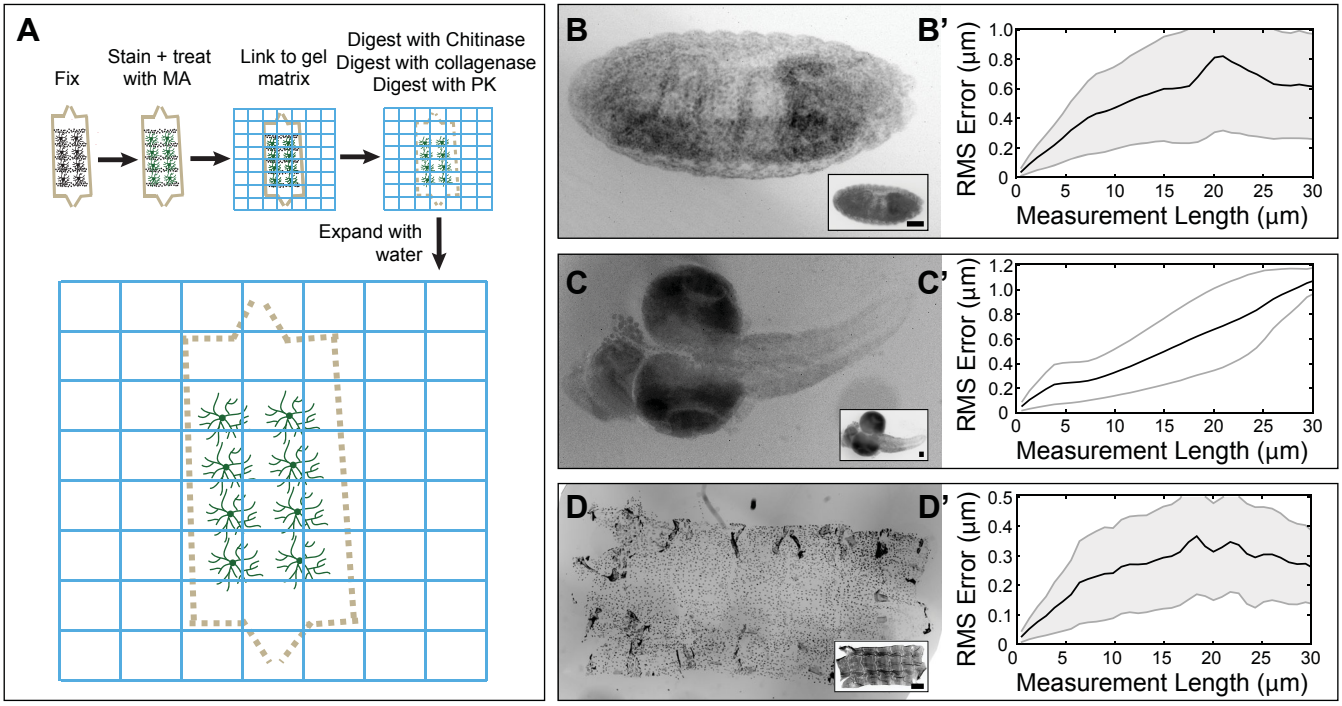

Figure 2.1. ExM can be applied to different fly tissues. (A) Schematic illustration of expansion microscopy in *Drosophila* larva. (B-D) Compare the expanded tissue size with the original tissue size (pictures at right bottom corner).The final expansion of the tissue showed about 4X linear increase in size. Tissues are stained with DAPI for visualization. (B'-D') Root-mean-squared measurement error(RMSE) of different tissue images before and after ExM. (C') shows the RMSE of the 3D correlative analysis with *Drosophila* brain images.The others are all analyzed in 2D. Scale bar (B,C) 50µm,(D) 500µm.

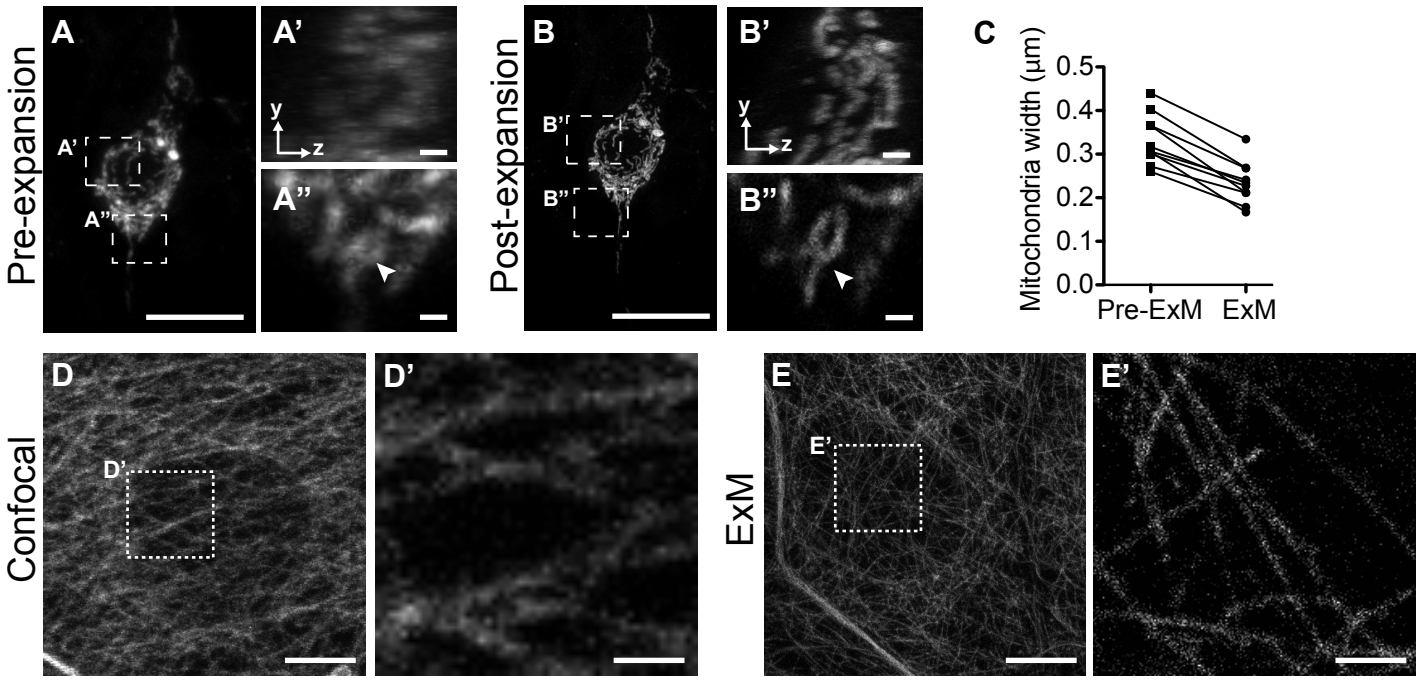

Figure 2.2. ExM applied to organelle imaging.(A) Maximum intensity projection of the pre-expanded mitochondria in a Class IV da neuron. (A') Zoomed-in YZ maximum intensity of the boxed region A' in A. (A") Zoomed-in maximum intensity projection of 3 slices in the stack of region A" in A. (B) Maximum intensity projection post-expanded mitochondria in the same Class IV da neuron. (B') Zoomed-in YZ maximum intensity of the boxed region B' in B. (B") Zoomed-in maximum intensity projection of 5 slices in the stack of region B" in B. (C) Measured width of mitochondria branches in single image slices taken before and after expansion. (D) Maximum intensity projection of conventional confocal image of the microtubules in a *Drosophila* larval body wall epithelial cell. (D') Zoomed-in maximum intensity projection of 5 slices in the stack of region D' in D. (E) Maximum intensity projection of ExM image of micro-tubules in a *Drosophila* larval body wall epithelial cell.(E') Zoomed-in maximum intensity projection of 5 slices in the stack of region E' in E. All distances and scale bars correspond to pre-expansion dimensions. Scale bars,10µm (A,B),1µm (A',A",B',B",D',E'), 5µm (D,E)

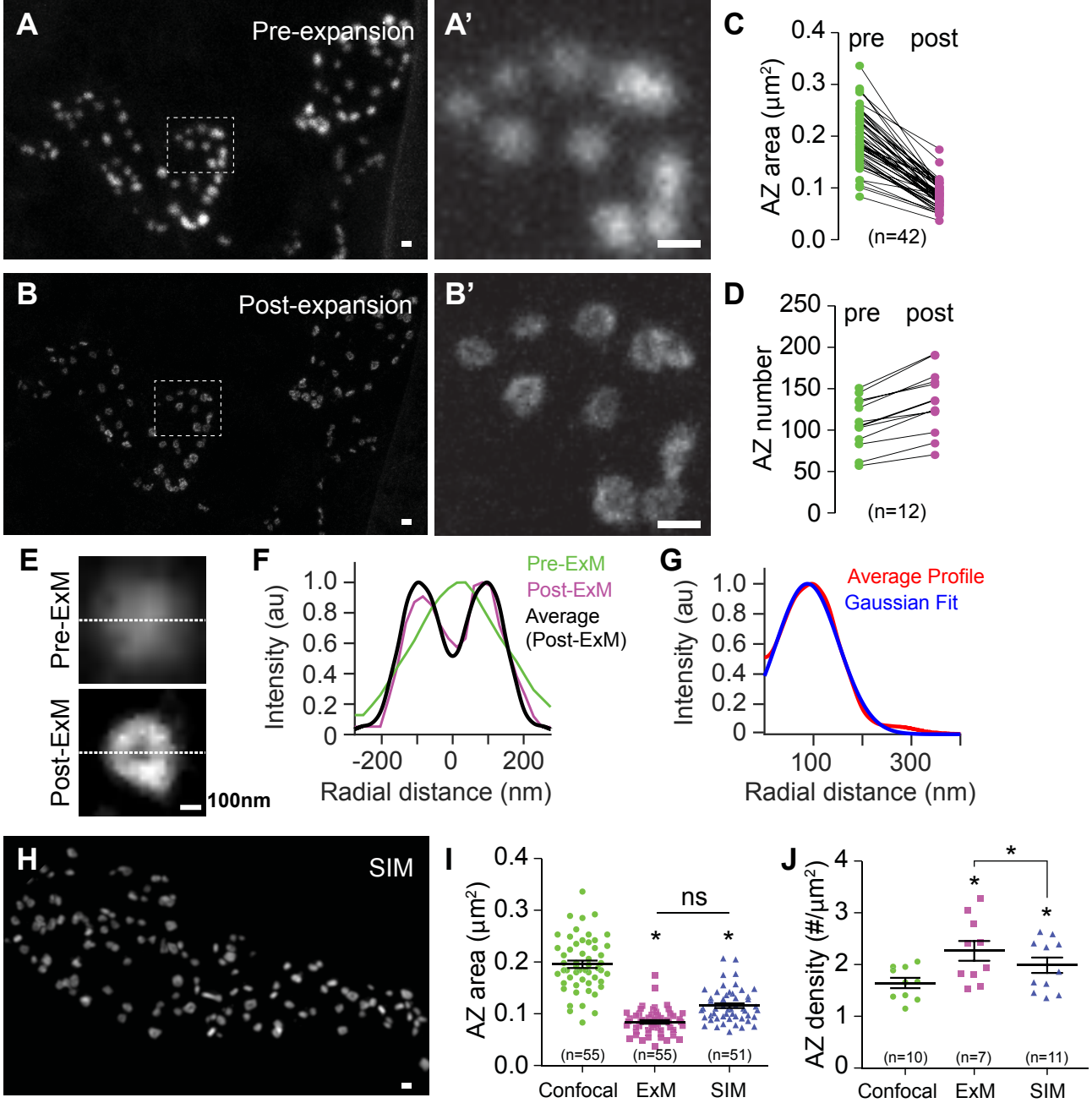

Figure 2.3. ExM resolves substructural information on the AZ. (A) Maximum intensity projection of the pre-expansion *Drosophila* larval body wall NMJ AZ stained with Brp. (A') Zoomed in view of the boxed region in A. (B) Maximum intensity projection of the post-expansion of the same *Drosophila* larval body wall NMJ AZ stained with Brp. (B') Zoomed in view of the boxed region in B. (C) AZ size measured on confocal images taken before and after expansion. (D) AZ numbers counted on confocal images taken before and after expansion. (E) Pre and post expansion images of one AZ. The donut structure of the AZ can be resolved after expansion. (F) Cross section profile of lines in E. (G) En face views of individual AZ were aligned according to their centers of mass and the radial density distributions of Brp localizations were plotted. (H) Maximum intensity projection SIM image of the *Drosophila* larval body wall NMJ AZ stained with Brp. (I) AZ size measured on images taken with different imaging techniques. (J) AZ density measured on images taken with different imaging techniques. All distances and scale bars correspond to pre-expansion dimensions. Scale bars, (A,A',B,B',H) 500nm, (E) 100nm. Scatter plots show mean + SEM. p values are indicated as: *p < 0.05, n.s. = not significant as assessed by Tukey's multiple comparison test.

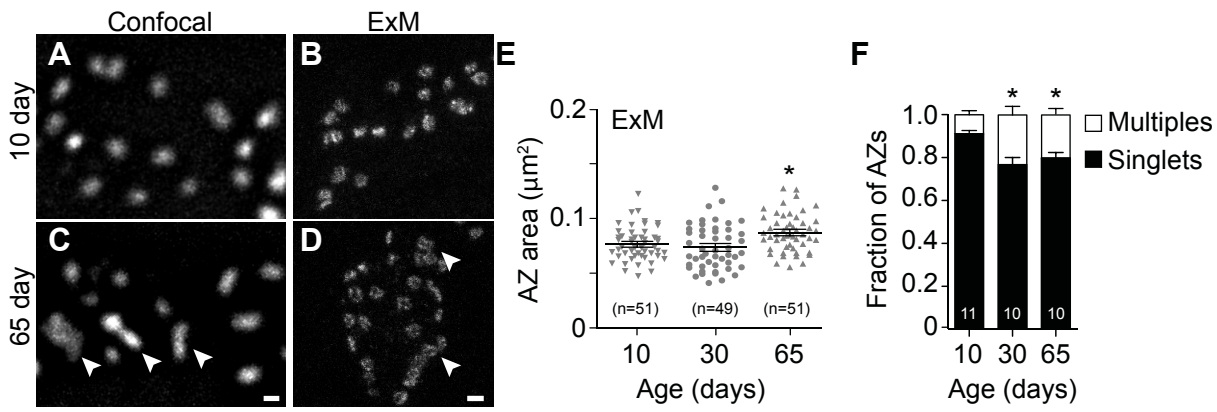

Figure 2.4. ExM resolves substructural information on the AZ of the adult Dro-sophila CM9 muscle. (A) Confocal image of 10-days-old adult fly CM9 muscle NMJ AZ stained with Brp.(B) ExM image of 10-days-old adult fly CM9 muscle NMJ AZ stained with Brp.(C) Confocal image of 65-days-old adult fly CM9 muscle NMJ AZ stained with Brp.(D) ExM image of 65-days-old adult fly CM9 muscle NMJ AZ stained with Brp.(E) Quantification of the CM9 muscle AZ size of adult flies of differ-ent ages. 65-days-old flies have significantly larger AZ size than younger flies.(F) Quantification of the number of single AZ and number of AZ multiples. Older adult flies have significantly more AZ multiples than the 10-days-old adult fly. All distances and scale bars correspond to pre-expansion dimensions. Scale bars,1µm (A,B,C,D). p values are indicated as: *$p < 0.05$ as assessed by Dunnett's multiple comparisons test.

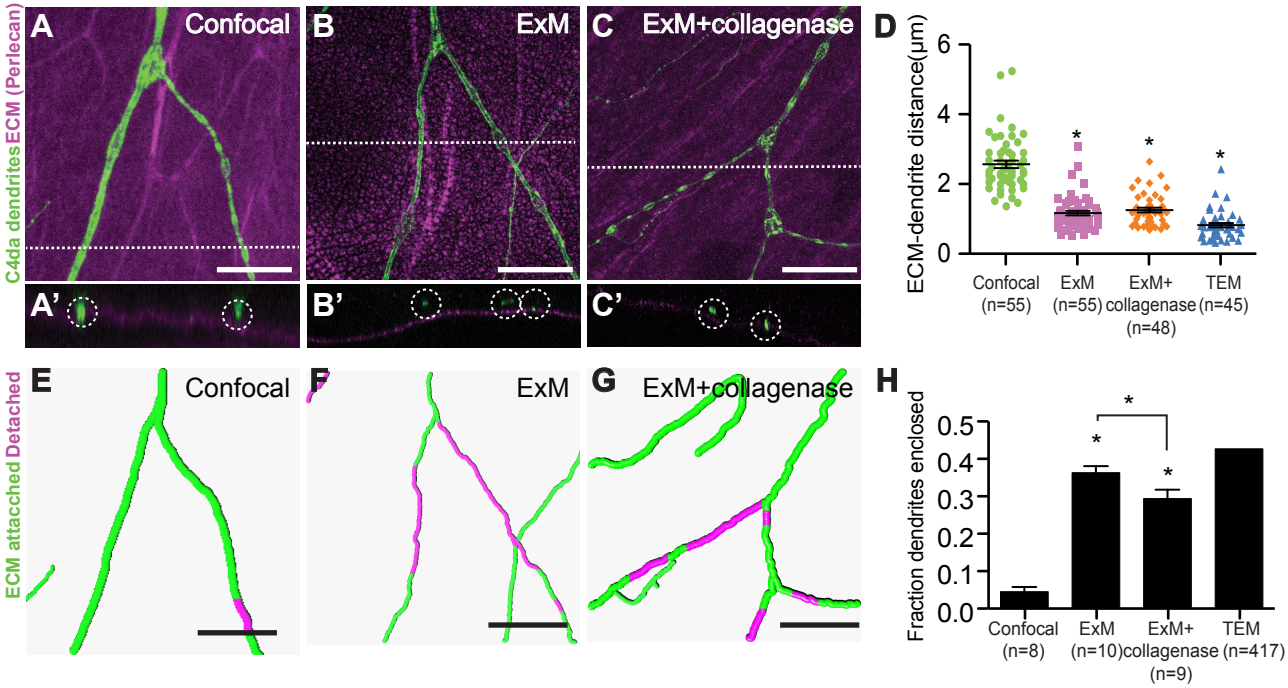

Figure 2.5. ExM resolves neuron- epithelial interaction. (A) Confocal image of Class IV da neuron dendrites (green) and ECM (magenta). (A') XZ view of the dotted line in A. (B) ExM image of the Class IV da neuron dendrites and ECM.(B') XZ view of the dotted line in B'. (C) ExM with collagenase treatment of the Class IV da neuron dendrites and ECM. (C') XZ view of the dotted line in C. (D) Measurements of enclosed dendrites to ECM on images taken with different imaging techniques. (E,F,G) Rendered dendrites from A,B and C respectively with ECM attached dendrites colored green and ECM detached dendrites colored magenta. (H) percentage of the enclosed dendrites quantified using images taken with different imaging techniques. All distances and scale bars correspond to pre-expansion dimensions. Scale bars,10μm. p values are indicated as: *$p < 0.05$ as assessed by Dunnett's multiple comparisons test.

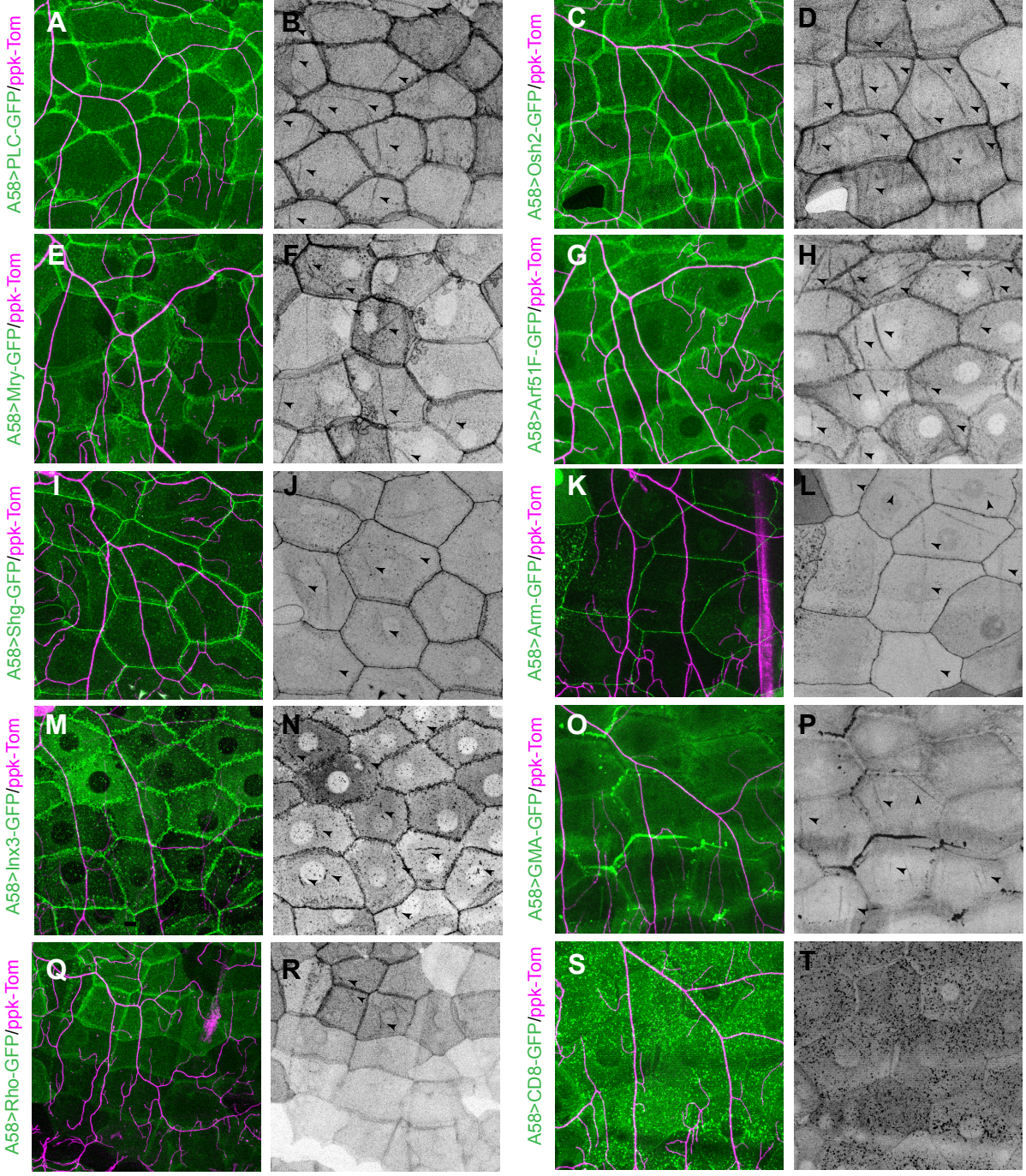

Figure 3.1. Image gallery of dendritic ensheathment markers. (A, B) Live imaging of a quadrant of the Class IV da neuron arbor of *ppk-CD4-tdTom, A58gal4 > PLC-GFP* larva. (B) PIP2 channel indicates PIP2 enrichment associates with the dendritic arbor as pointed by arrows. (C, D) Live imaging of a quadrant of the Class IV da neuron arbor of *ppk-CD4-tdTom, A58gal4 > Osh2-GFP* larva. (D) Osh2 labeled PIP2 channel indicates PIP2 enrichment associates with the dendritic arbor as pointed by arrows. (E, F) Live imaging of a quadrant of the Class IV da neuron arbor of *ppk-CD4-tdTom, A58gal4 > Myr-GFP* larva. (F) Myr-GFP channel indicates membrane lipids components enrichment associate with the dendritic arbor as pointed by arrows. (G, H) Live imaging of a quadrant of the Class IV da neuron arbor of *ppk-CD4-tdTom, A58gal4 > Arf51F-GFP* larva. (H) Arf51F channel indicates Arf51F enrichment associates with the dendritic arbor as pointed by arrows. (I, J) Live imaging of a quadrant of the Class IV da neuron arbor of *ppk-CD4-tdTom, A58gal4 > Shg-GFP* larva. (J) Shg channel indicates E-cadherin enrichment associates with the dendritic arbor as pointed by arrows. (K, L) Live imaging of a quadrant of the Class IV da neuron arbor of ppk-*CD4-tdTom, A58gal4 > Arm-GFP*P larva. (L) Arm channel indicates β-catenin enrichment associates with the dendritic arbor as pointed by arrows. (M, N) Live imaging of a quadrant of the Class IV da neuron arbor of ppk-CD4-tdTom, A58gal4 > Inx3-GFP larva. (N) Inx3 channel indicates inx3 enrichment associates with the dendritic arbor as pointed by arrows. (O, P) Live imaging of a quadrant of the Class IV da neuron arbor of *ppk-CD4-tdTom, A58gal4 > GMA* larva. (P) GMA channel indicates F-actin enrichment associates with the dendritic arbor as pointed by arrows. (Q, R) Live imaging of a quadrant of the Class IV da neuron arbor of *ppk-CD4-tdTom, A58gal4 > Rho-GFP* larva. (R) Rho channel indicates Rho enrichment associates with the dendritic arbor as pointed by arrows. (S,T) Live imaging of a quadrant of the Class IV da neuron arbor of *ppk-CD4-tdTom, A58gal4 > CD8-GFP* larva. (T) CD8-GFP channe l indicates membrane marker CD8-GFP doesn't associate with the Class IV da neuron dendritic arbor. Scale bar 10μm

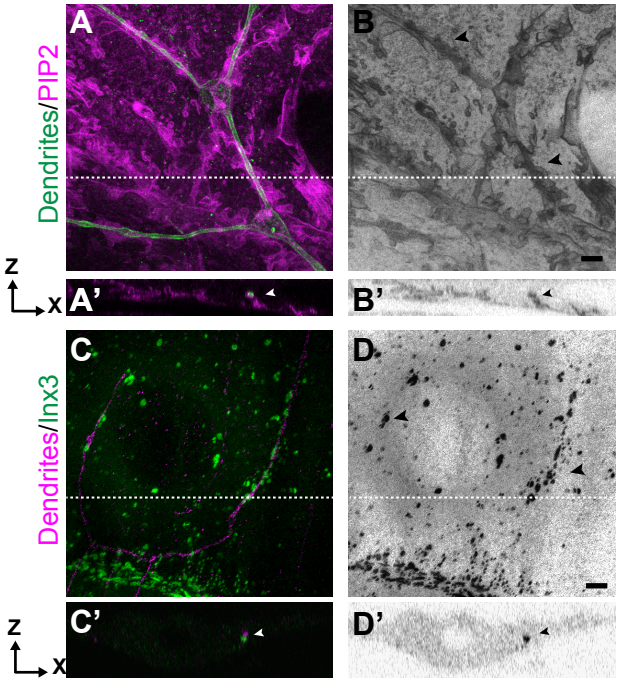

Figure 3.2. ExM resolves the localization of the epithelial ensheathment molecules. (A, B) ExM *of ppk-CD4-tdTom, A58gal4>PLC-GFP* larva stained with dsred antibody and GFP antibody to label Class IV da neuron dendrites and epithelial PIP2. (B) PIP2 channel indicates PIP2 enrich-ments as pointed by the arrows. (A', B') XZ views of the dotted lines in A and B. Arrows pointed to the dendritic ensheathment structure. (C, D) ExM of *ppk-CD4-tdTom, A58gal4>Inx3-GFP* larva stained with dsred antibody and GFP antibody to label Class IV da neuron dendrites and epithelial Inx3. (D) Inx3 channel indicates Inx3 enrichments as pointed by the arrows. (C', D') XZ views of the dotted lines in C and D. Arrows pointed to the dendritic ensheathment structure. Inx3 molecules localize at the basal side of the ensheathment structure. All distances and scale bars correspond to pre-expansion dimensions. Scale bar, 2.5μm.

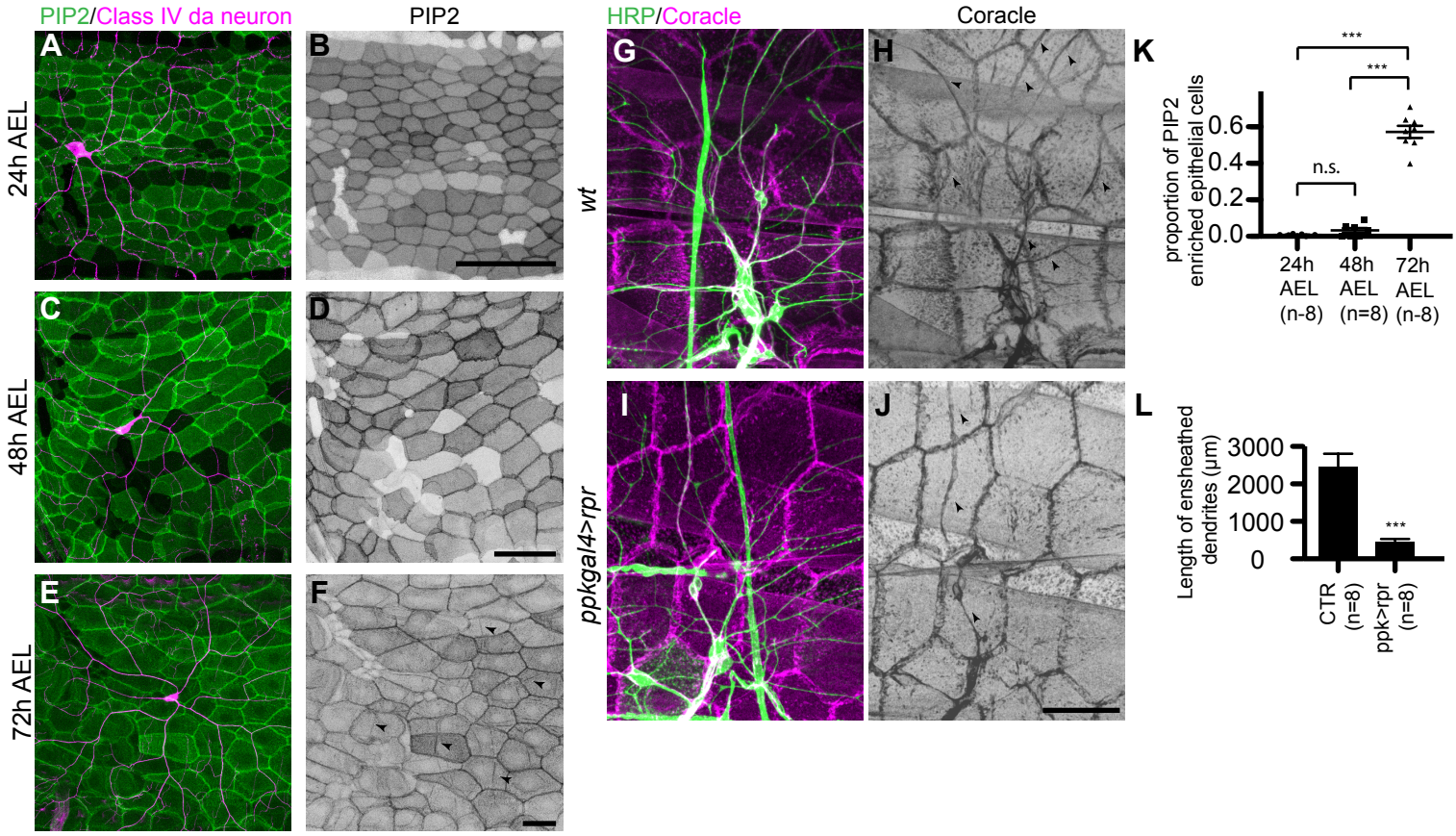

Figure 3.3. Dendrites are required for the formation of epithelial membrane specialized domains. (A, B, C, D, E, F) Live imaging of a Class IV da neuron (magenta) with epithelial PIP2 (green) of the *ppk-CD8-tdTomato, A58>PLC-GFP*P larva at different developmental time points. (B, D, F) PIP2 channel at different time points shows PIP2 enrichment occurs at late larval developmental stage. (G, H) Wild type larva stained with HRP (labels all sensory neurons) and coracle (ensheathment marker). (H) Arrows point to coracle channel dendritic ensheathment. (I, J) Class IV da neuron ablated larva stained with HRP and coracle. The HRP positive dendrites in (I) are from the Class I, Class II and Class III da neurons. (J) Arrows point to Coracle channel dendritic ensheathment. Coracle enrichment is largely decreased without Class IV da neurons. (K) Quantification of the proportion of ensheathment at different developmental time points. (L) Dendrite ensheathment was largely decreased when Class IV neurons were removed by rpr. Scale bar 50µm. Bar plots show mean + SD. p values are indicated as: ***p < 0.001 as assessed by unpaired t-test. Scatter plots show mean + SEM. p values are indicated as: ***p < 0.001, n.s. = not significant as assessed by Tukey's multiple comparison test.

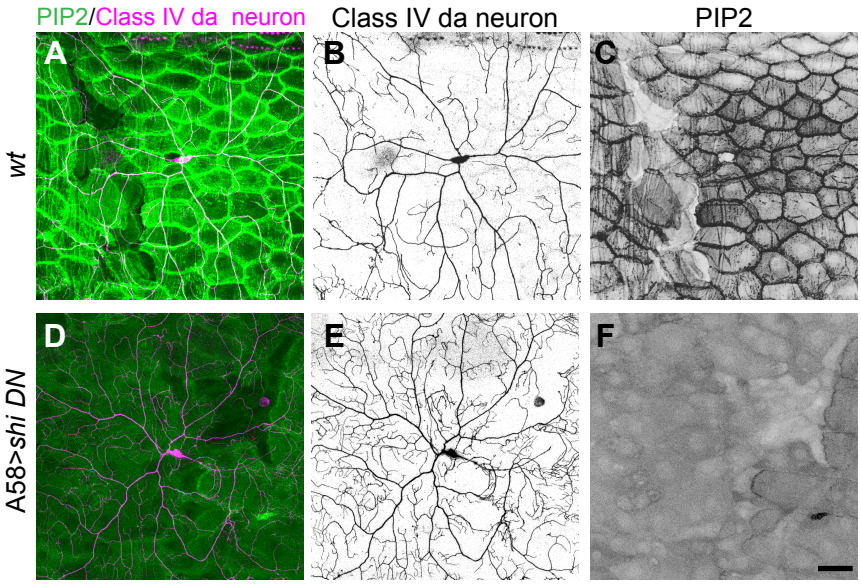

Figure 3.4. Epithelial endocytic pathway regulates epithelial membrane special-ized ensheathment structure and dendrite morphology. (A-C) Live imaging of third instar *ppk-CD4-tdTom, A58gal4 > PLC-GFP* larva. (B) Class IV da neuron channel shows the wild type neuron phenotype. (C) PIP2 channel shows PIP2 enrichments along the dendritic arbor in the wild type larva. (D-F) Live imaging of third instar larva with epithelial endocytosis being blocked by *SHi DN*. (E) Class IV da neuron channel shows the over growth dendrite phenotype after blocking epithe-lial endocytosis. (F) PIP2 channel shows no PIP2 accumulation in epithelial cells after blocking epithelial endocytosis. Scale bar 50μm.

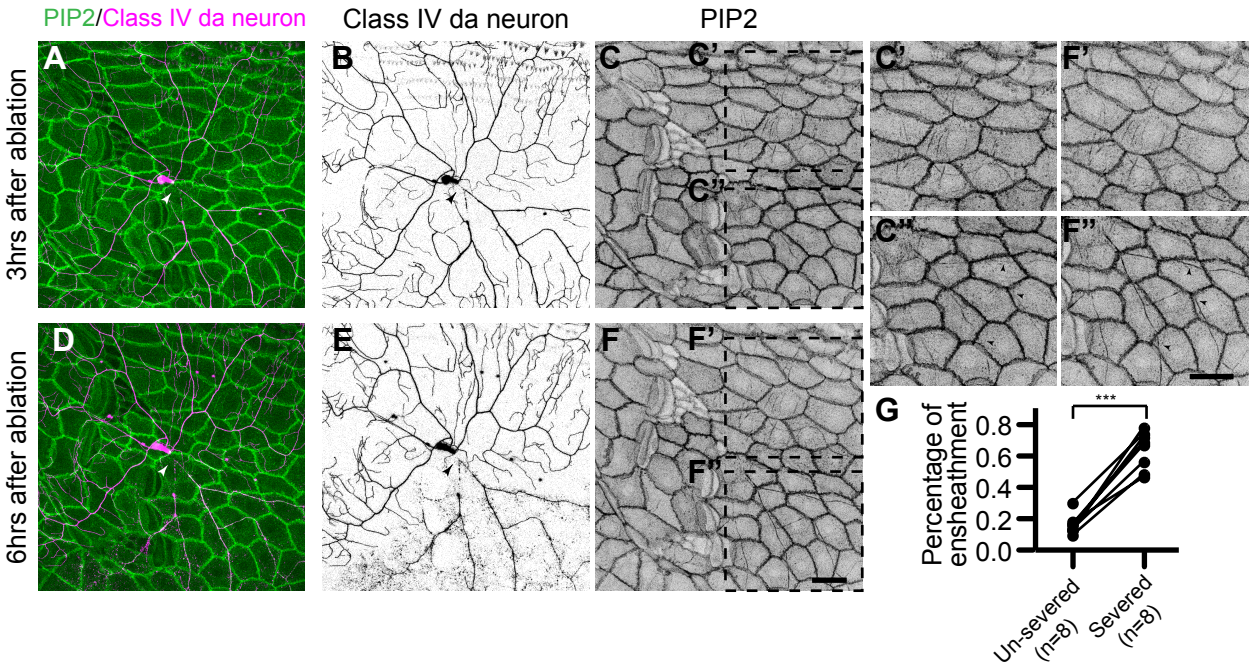

Figure 3.5. Dendritic ensheathment during dendrite degeneration. (A-C) Class IV da neuron dendrite was severed (arrow) at 72 hrs AEL and imaged 3hrs after abla-tion. Class IV da neuron was labeled with *ppk-CD8-tdTomato* (magenta). Epithelial PIP2 was labeled with *A58gal4 > PLC-GFP* (green). (B) Class IV da neuron channel indicates dendrite degeneration has not started at 3hrs after ablation. (C) PIP2 chan-nel indicates PIP2 enriched at ensheathed dendrites. (D-F) The same Class IV da neuron was imaged at 6hrs after ablation. (E) Class IV da neuron channel indicates dendrite degeneration has started at 6hrs after ablation. (F) PIP2 channel indicates PIP2 enrichment at the severed dendrite has increased. (C',F') Zoomed in view of the boxed region in C and F. PIP2 enrichment of unsevered dendrite at 3hrs and 6hrs after ablation. (C", F") Zoomed in view of the boxed region in C and F. PIP2 enrich-ment of the severed dendrite at 3hrs and 6hrs after ablation. Arrows point to the newly formed PIP2 enrichment during degeneration. (G) Quantification of the ensheathment percentage on severed and un-severed dendrites at 6hrs after abla-tion. More dendrites are ensheathed during degeneration. Scale bar, 50μm. Plots show the percentage of ensheathment of un-severed dendrites versus severed dendrites. p values are indicated as: ***p < 0.001 as assessed by paired t test.

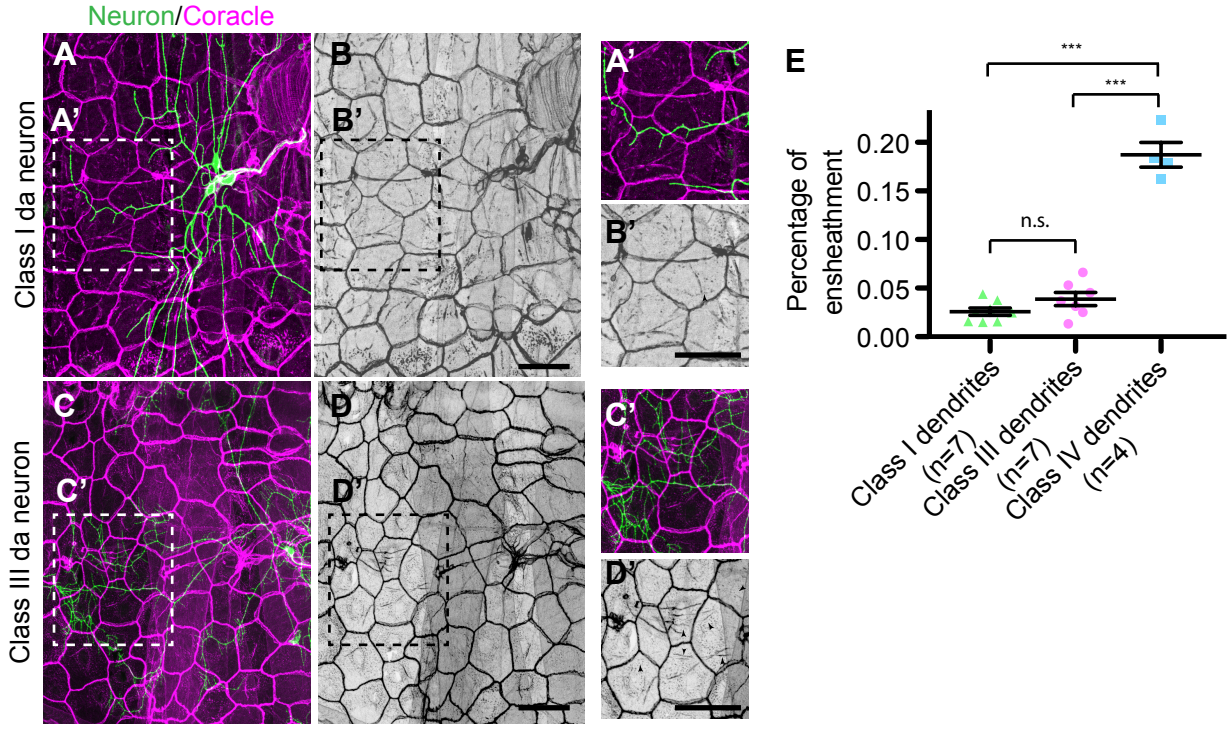

Figure 3.6. Dendritic ensheathment of other classes of somatosensory neu-rons. (A, B) Staining of the third instar *Gal4*^{221}*, UAS-mCD8-GFP* larva with anti GFP and coracle antibodies. The majority of coracle enrichments are not colocalized with the Class I neuron dendrites. (B) Coracle channel shows enrichment of coracle on epithelial cells. (C, D) Staining of the third instar *nompC-gal4 ,UAS-mCD8-GFP* larva with anti GFP and coracle antibodies. The majority of coracle enrichments are not colocalized with the Class III neuron dendrites. (D) Coracle channel shows enrichment of coracle on epithelial cells. (A',B',C',D') Zoomed in views of the boxed regions in A,B,C and D. Coracle enrichments colocalized with dendrites are noted by arrows. (E) Quantification of dendritic ensheathment levels in different classes of somatosensory neurons. Scale bar 50μm. Scatter plots show mean + SEM. p values are indicated as: ***p < 0.001, n.s. = not significant as assessed by Tukey's multiple comparison test.

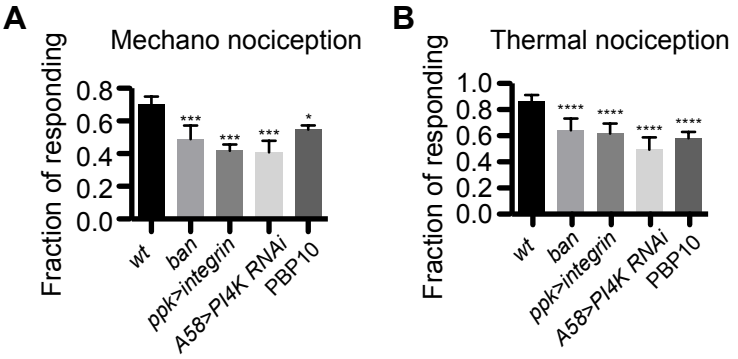

Figure 3.7. Dendritic ensheathment is import-ant for Class IV da neuron nociception. (A) Responding rate of larvae with different dendritic ensheathment levels to 80mN von frey filaments. n = 5 trials per each genotype group. 30 larvae were tested per each trial. (B) Responding rate of larvae with different dendritc ensheathment levels to heat probe stimu-lation. n = 5 trials per each genotype group. 30 larvae were tested per each trial. Bar plots show mean + SD. p values are indicated as: *p < 0.05, ***p < 0.001, ****p < 0.0001 as assessed by Dunnett's multiple comparisons test.

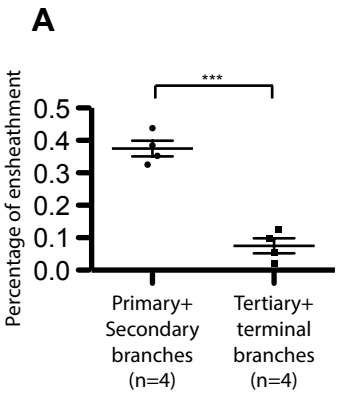

Supplemental Figure 3.1. Distribution of the ensheathed dendrites on the Class IV da neuron dendritic arbor. (A) Plots show the percentage of ensheathment on different subsets of dendrite branch-es. Dendrite ensheathment primarily occurs on primary and secondary branches, oppossed to tertiary and terminal branches. p values are indicated as: ***$p < 0.001$ as assessed by paired t test.

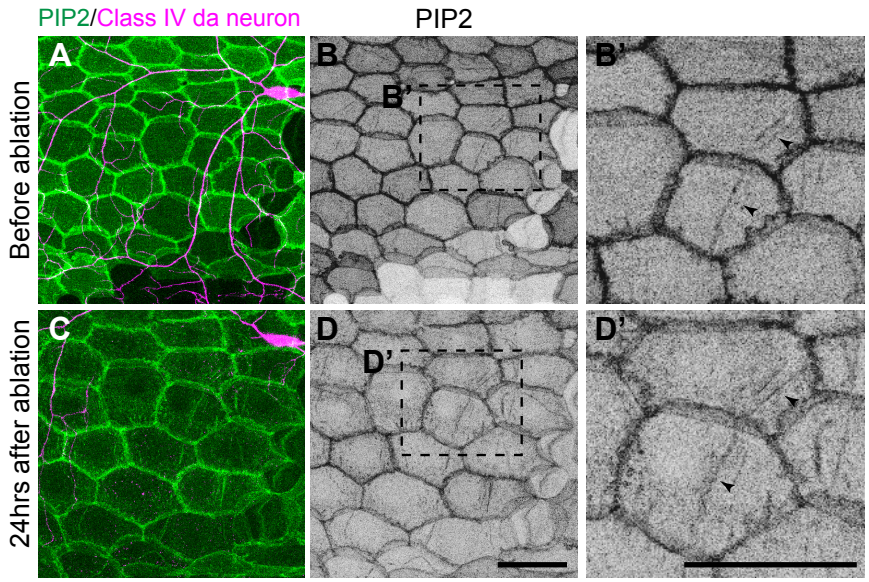

Supplemental Figure 3.2. Epithelial ensheathment structure is maintained after dendrite degradation. (A, B) Live imaging of a quadrant of the Class IV da neuron arbor of *ppk-CD4-tdTom, A58gal4 > PLC-GFP* larva before severing. (B) PIP2 channel shows PIP2 enrichment before dendrite severing. (C-D) Live imaging of the same quadrant of the Class IV da neuron arbor of *ppk-CD4-tdTom, A58gal4 > PLC-GFP* larva 24hrs after severing. The severed dendrite branch is degraded. (D) PIP2 channel shows PIP2 enrichment after dendrite degradation. (B',D') Zoomed in view of the boxed regions in B and D, showing epithe-lial membrane PIP2 enrichment is maintianed after dendrite degradation. Scale bar, 50μm.

VITA

My name is Nan Jiang. I was born and grew up in north China. I came to the United States at 2011 for graduate School at the University of Washington. Before that I went to college at Sichuan University in China with a major in Biology. At the University of Washington, I joined Dr. Jay Parrish's lab in the department of Biology to work on neuron epidermis interactions.